PARAMETRIC REDUCED-ORDER MODELS OF STRUCTURAL DYNAMICS FOR DESIGN, DAMAGE DETECTION AND STRUCTURAL OPTIMIZATION

by

Sung-Kwon Hong

A dissertation submitted in partial fulfillment
of the requirements for the degree of
Doctor of Philosophy
(Mechanical Engineering)
in The University of Michigan
2012

Doctoral Committee:

Associate Professor Bogdan I. Epureanu, Chair
Professor Michael M. Bernitsas
Professor Gregory M. Hulbert
Assistant Professor Kenn R. Oldham
Visiting Scholar Matthew P. Castanier, U.S. Army TARDEC

To my family and wife

ACKNOWLEDGEMENTS

First, I wish to express my utmost gratitude to my advisors and chair of my doctoral committee, Professor Bogdan I. Epureanu, for his inspiring and encouraging guidance during the past years. I would like to thank to Dr. Matthew P. Castanier for providing a chance to study on this work and numerous great research ideas. I also want to thank Professor Michael M. Bernitsas, Professor Gregory M. Hulbert, and Professor Kenn R. Oldham for their valuable comments and suggestions, and serving on my doctoral committee. I sincerely admit that it my not be possible to attain without their supervision and supports.

I am also grateful to my colleagues of Vibration and Acoustics Laboratory, including Keychun Park, Akira Saito, Andrew Madden, Darren Holland, Joosup Lim, Chulwoo Jung, Woochul Nam, Kiran D'Souza, Andrew Sloboda, Anish Joshi, Jason Rodgers, and Olguta Marinescu, for their insights and suggestions. It has been a very nice time and a good memory for me.

Additionally, I would like to express my appreciation for my entire family, in particular my parents and in-laws for their love and supports. I would like to thank my daughter Jisoo, and my sun Jaehee for being so adorable. Finally, I would like to thank my lovely wife, Hyunjung, for everything. I would like to give my thanks and apologies to all those who helped me but not mentioned here.

This research was supported by the Automotive Research Center, a U.S. Army RDECOM center of excellence for modeling and simulation at the University of Michigan.

TABLE OF CONTENTS

LIST OF FIGURES

Figure

LIST OF TABLES

Table

CHAPTER I

Introduction

1.1 Dissertation Objective

Finite element models (FEMs) are often used to predict vibration responses and stresses to support design processes. Also, evaluating variations in structural responses caused by design changes and damages (such as cracks and dents) is an important challenge in a wide variety of applications. As computing capabilities increase, simulation techniques replace experiments for testing designs, especially when the experiments are considerably expensive or difficult to execute. However, the conventional design complexity can make the analysis very slow when many substructure changes are needed during the iterative process such as design, statistical analyses, and optimization problems. This issue is particularly important because usual industrial FEMs (such as automobile bodies and complex airplane structural components) have millions of degrees of freedom (DOFs). These models, with very large numbers of DOFs, have to be used to ensure high accuracy. However, the large computational cost of direct analyses based on these large models detrimentally affects the design cycle. Thus, model reduction techniques such as those presented in this work are necessary to reduce the computational cost.

An alternative to direct structural analysis of computationally expensive models is based on component mode synthesis (CMS) because CMS can be combined with a wide

variety of FEM-based methods. In the context of vibration analysis, CMS is used by first dividing the global structure into components. Next, each component is projected onto a very small truncated set of (component-level) basis vectors that approximately span the space of the (component-level) response. As a result, the number of DOFs required to model each component is considerably reduced compared to standard FEMs. Finally, the models of each component are assembled, and a global reduced-order model (ROM) is synthesized. As a result, the order of the global model is reduced significantly.

Although many CMS techniques have been developed for basic structural analyses, they have not been constructed for design or damage detection in complex structures. The key element that separates ROMs for design from those used for basic structural analysis, is that usual ROMs cannot easily be re-constructed when changes are applied (by design or through damage) in a few components of the overall system. Recently, design-oriented ROMs have been developed to avoid prohibitively expensive reanalyses of complex structures. These recent models are referred to as parametric reduced-order models (PROMs). These PROMs are global in nature, in that they require access to the full system model as part of the process. To address this issue, design-oriented PROMs built in a component-oriented framework are needed for design and damage modeling.

Design-oriented PROMs are important for vibration-based structural health monitoring (SHM) and structural optimization. For example, vibration-based SHM techniques are of current interest in identifying damage and assessing the integrity of structures such as vehicles and airplanes. Predicting the dynamic characteristics of damaged (cracked) structures is an important challenge for vibration-based SHM. For this challenge, PROMs can be used to predict the mode shapes of a cracked structure at a dramatically reduced computational cost. The characteristics of the dynamic response predicted by PROMs provide useful signals for vibration-based SHM. However, not all of the signals obtained

from PROMs can be used in practice due to limited accessibility constraints and cost of the needed sensors. Thus, a methodology to select optimal sensor locations for SHM is developed for the purpose of accurately capturing changes in mode shapes and identifying the size of a crack.

Another use of PROMs is for structural optimization. Typically, mechanical structures such as those found in automobiles and airplanes consist of multiple components which are assembled using joints such as bolts, welds, rivets, etc. The locations (assembly points) of these joints affect structural performance characteristics such as the static compliance, the frequency response, and the durability. To achieve high performance, the joining locations should be selected by a systematic approach rather than an experience-based approach. However, this issue can be quite challenging because there are many joints (as many as several thousand) and even more possible joining locations for large scale complex structures. Thus, a systematic approach to select optimal joining locations of components of complex structures is necessary.

The primary objectives of this research are as follows:

- To develop efficient and accurate PROMs which can be used to predict the vibration characteristics of complex structures for the purpose of design and damage modeling.
- To develop a robust signal processing technology for SHM based on PROMs.
- To develop an algorithm to identify the size of a crack in complex structures based on a robust signal processing technology.
- To develop a structural optimization technique to select optimal joining locations for the assembly of complex structures.

1.2 Dissertation Background

1.2.1 Component mode synthesis and parametric reduced-order models

Structural dynamic analyses often have high computational costs because repetitive calculations are needed in the processes of optimization, stochastic analysis , and statistical analysis. These repetitive calculations are very time consuming especially when conventional complex and large models are used. One method to reduce the computational cost is to use reduced-order models (ROMs). Such ROMs have been used in a variety of applications. Yun and Masri [1, 2] developed a methodology for stochastic detection of changes in uncertain nonlinear systems using ROMs. Chung and Fung [3] proposed a nonlinear finite element model of piezoelectric tube actuators with hysteresis and creep for control and design purposes. In their work, the operation of the actuators is simulated using ROMs. Ashwin *et al.* [4] developed a finite element substructuring procedure for design analysis of large structural systems. Hartl *et al.* [5] also developed advanced methods for analysis, design, and optimization which use ROMs for computational efficiency.

In the field of structural dynamic analysis, component mode synthesis (CMS) [6–12] is well established as an alternative to conventional finite element models (FEMs) with large numbers of degrees of freedom (DOFs). CMS belongs to a wide class of domain decomposition techniques. CMS divides the global structure into several substructures, and the DOFs of each individual substructure are reduced separately. Then, the substructure are reconnected, and the dynamic response of the system is predicted very efficiently and accurately. Applications of CMS include the work of Wang and Kirkhope [13] who applied CMS for multi-shaft rotors with flexible inter-shaft bearings. They also used CMS for damped systems [14]. In addition, Liu and Zheng [15] proposed an improved CMS method for nonclassically damped systems. Takewaki [16] proposed an inverse CMS method for redesign of large structural systems. Matichard and Gaudiller [17] used CMS to develop

a hybrid modal nodal method for model reduction and feedback control (of multi-body, smart structures). Kim [18] also developed a recursive CMS method to solve large-scale eigenvalue problems efficiently. Tran [19] developed and applied a CMS approach which uses partial interface modes of cyclically symmetric structures. To enhance computational efficiency for redesign of large damped structural systems, Takewaki and Uetani [20] used a new formulation for an incremental inverse problem based on CMS. Elhami *et al.* [21] proposed methods for repetitive symmetric structures by CMS. Farhat and Geradin [22] developed a methodology which uses CMS for structures with incompatible substructures. Also, many other methodologies based on CMS have been developed for structural analyses [23–27].

The most common CMS approach is the fixed-interface Craig-Bampton CMS (CB-CMS) method [7]. CB-CMS is well understood and frequently used because of its simplicity and numerical stability. Herein, CB-CMS is used for substructuring analysis. However, existing CMS-based techniques were not originally constructed for design or damage detection in complex structures. Thus, there are several studies focused on improving CMS-based ROMs for these purposes. For example, Balmès *et al.* [28, 29] calculated sets of modes for a few sample parameter values in the parameter space, and grouped them into a fixed augmented basis for the modes of the nominal system. This augmented basis was found to be suitable for a (parametric) family of models. However, the need for repeatedly solving many sample eigenproblems makes the approach impractical for global parametric reduced-order models (PROMs) of realistic industrial FEMs. To accelerate solving the sampled eigenproblems, this technique was combined with a component-based approach by Zhang and Park [30, 31] for large FEMs. As a by-product, the eigenproblems of the sampled space are confined to one specific component, and the resulting global model is reduced substantially. However, in the projection phase, the component basis

has to be expanded back into the global coordinates. Hence, the approach does not lead to true component-based PROMs. To address that issue, substructural analysis techniques based on PROMs have been developed [32]. However, those PROMs can account for one parametric variability in one substructure only. In contrast, the new component PROMs developed herein allow several substructures to have parametric variability in characteristics such as geometric parameters (e.g., thickness), or material properties (e.g., Young's modulus). These new multiple-component PROMs (MC-PROMs) are obtained by simply managing the geometric compatibility conditions between substructures.

Geometric variations (e.g., dents or thickness variability due to manufacturing) can be treated as parametric variability in the structure. Such an approach has been used for a few years to investigate the vibration of turbo machinery bladed disks. For example, static mode compensation has been used for global models [33, 34] to compute the vibration response of a structure which has dents or missing material. By accounting for the effects of geometric variability as though they are produced by external forces, a set of basis vectors can be established using a combination of normal modes of the pristine structure compensated by static modes. However, the static mode compensation method for geometric variations has not been applied for substructuring. Herein, CMS with static mode compensation is developed based on CB-CMS. When substructures have dents, component mode synthesis with static mode compensation (SMC-CMS) is applied to obtain the vibration response. Finally, the effects of parameter variations (e.g., thickness and geometric variations) are analyzed by MC-PROMs and SMC-CMS [35].

For modeling cracks, Poudou and Pierre [36, 37] have developed a hybrid frequency-time domain method. In that method, the resonant frequencies of the cracked structure are found by a forced response analysis. That is a nonlinear problem whose solution is complex and computationally intensive. To alleviate this issue, a bi-linear frequency

approximation (which was first used to predict resonant frequencies of single-DOF piece-wise linear systems [38]) is generalized to large dimensional models. The approach herein builds on the early methods for studying the vibration of cracked beams and plates using a multi-DOFs model. Chati *et al.* [39] have studied the bi-linear frequency approximation for a two dimensional cracked beam, and Saito *et al.* [40] have used a bi-linear frequency approximation for a three dimensional cracked plate. Note that the actual motion of the crack surfaces can be quite complex, and there may be more than two crack states (open and closed) when, for example, the crack closing proceeds gradually so that different regions of the crack surfaces close at different times. Although the generalized bi-linear frequency approximation cannot capture the effects of gradual opening and closing, it can provide approximate values for the resonant frequencies of complex cracked structures by employing linear analyses only. Also, the linear analyses required in a bi-linear frequency approximation can be performed using MC-PROMs, and that further reduces the computational cost.

1.2.2 Robust signal processing for damaged structure

Robust techniques for sensor placement and damage detection are of current interest because of the increased need to reduce the time and the cost of examining the structural integrity of ground vehicles and aircraft. To assess integrity, structural information must be obtained using a variety of sensors. Both the number and the locations of sensors are limited due to cost and accessibility constraints. There are many previous studies of sensor placement for structural health monitoring. For example, Ansari [41] has implemented SHM strategies which require selection and placement of sensors suitable for measuring key parameters that influence the performance and health of civil structures. Flynn and Todd [42] have proposed a novel approach for optimal actuator and sensor placement for

SHM. Krommer *et al.* [43] have investigated a sensor network composed of strain-type patch sensors with constant intensity designed to replace distributed strain-type sensors for monitoring beam-type structures.

Herein, a novel robust signal processing technique is employed to find the optimal number of sensor locations for gathering mode shape information of cracked structures. The novel approach is developed starting from an algorithm based on the effective independence distribution vector (EIDV) [44, 45]. The key idea of EIDV is to choose sensor locations for measuring physical mode shapes as linearly independent as possible in the frequency range of interest. Herein, the EIDV method is modified to select optimal sensor locations for cracked complex structures. The number of selected locations based on the modified EIDV method is not only limited to the frequency range of interest, but also limited in the way which it can handle the effects of measurement noise. To address this noise, over-sampling is often performed. EIDV cannot provide optimal locations for over-sampling. Herein, a new signal processing technique is developed to select over-sampled measurement locations.

In addition, novel robust signal processing techniques are applied to identify the size of a crack. In particular, an approach to place sensors to optimally capture the variation of mode shapes is developed and combined with the new algorithm for crack size detection.

1.2.3 Selection of optimal joining locations

The number of joining locations for assembled complex structure can be as many as several thousand. The choice for joining locations in the assembly can be improved by topology optimization approaches such as homogenization techniques [46] and density methods [47–49]. Homogenization techniques compute an optimal distribution of microstructures in a given design domain. Density methods compute an optimal distribution

of isotropic materials, where the material densities are design variables. Although single-component topology design has been extensively studied during the past two decades [50], the amount of research done for multiple-component topology optimization is relatively small. In that area of research, Chirehdast and Jiang [51] extended the concept of topology optimization to the design of spot-weld and adhesive bond patterns. Following that, Jiang and Chirehdast [52] proposed a theoretical framework to determine which optimal connection points minimize the static compliance of the given substructures. To solve the coupled problem of component topology and joining location optimization, Chickermane and Gea [53] proposed a methodology for a multiple-component structure as a whole, in which the optimal topology and the joint locations were computed simultaneously. More recently, Zhu and Zhang [54] did layout optimization of structural supports using a topology optimization method for free vibration analyses. All these previous efforts employed spring elements for modeling joints. In contrast, Li *et al.* [55] proposed a fastener layout/topology that achieves an almost uniform stress level in each joint, and adopted evolutionary structural optimization [56–61] to provide an alternative optimization strategy to traditional gradient-based topology optimization approaches. In the context of these past efforts, the focus of this work is on the development of an efficient framework for determining improved/optimal joining locations so as to minimize the total energy input into the structure and the strain energy in the joints of a complex structure with variability using a density-based method.

1.3 Dissertation Overview

The main contributions of this dissertation are summarized briefly as follows:

(1) Novel multiple-component parametric reduced-order models are developed that more directly and efficiently capture the influence of component-level design changes and

damages (variabilities in geometrical and material properties) on the system-level dynamic response.

(2) Next-generation parametric reduced-order models having a numerically stable formulation are developed and used to analyze complex structures modeled with brick-type finite elements.

(3) New robust signal processing and crack detection algorithms are extended and developed to identify the size of a crack

(4) Structural optimization techniques are developed in a unique workframe for joining of components of complex structures for improved dynamic response

The remaining chapters of this dissertation are compiled from a collection of five manuscripts submitted to archival journals (where they are either in review or in print). Because of this, some of the background material is repeated in various chapters. The remaining chapters in this thesis are summarized as follows.

Chapter II describes the development of multiple-component parametric reduced-order models for design and damage detection (structural variability, dents and crack).

Chapter III describes the development of the next-generation parametric reduced-order models which have a numerically stable formulation (a new transformation matrix and a novel parameterization technique) and a local interface reduction technique.

Chapter IV describes robust signal processing for damaged vehicles with variability to select the optimal sensor locations to capture the mode shapes of a cracked structure, and to reduce the effects of measurement noise.

Chapter V describes a novel sensor placement for damage identification in a cracked complex structure with structural variability. It is shown that the crack size is estimated

very accurately by using a robust signal processing technology and Monte-Carlo simulation techniques.

Chapter VI presents a modeling and joining location optimization methodology for designing connections between components of assembled structures. New cost functions developed include the external energy input into the structure with damping and the strain energy of joints. The optimization techniques are applied to attach armor plate to a V-shaped structure.

Chapter VII reviews the findings and contributions of this dissertation and proposes future research topics.

CHAPTER II

Parametric Reduced-Order Models for Predicting the Vibration Response of Complex Structures with Component Damage and Uncertainties

2.1 Introduction

Structural analyses based on finite element models (FEMs) are often used to predict vibration responses, stresses, and other structural characteristics to support design processes. Also, evaluating the effects of possible damages (such as cracks and dents) on the structural response is crucial in a wide variety of applications. As computing power increases, simulation techniques replace experiments for testing designs, especially when the experiments are considerably expensive or difficult to execute. However, the complexity of the designs can make the analysis very slow when many component changes are needed during the design process. This issue is particularly important because usual industrial FEMs (such as automobile bodies and complex airplane structural components) have millions of degrees of freedom (DOFs). These detailed models, with very large numbers of DOFs, have to be used to ensure high accuracy. However, the large computational cost of direct analyses based on these large models detrimentally affects the design cycle, especially when it is necessary to evaluate the effects of parametric variability and damages on the structural response. Thus, model reduction techniques such as presented herein are

necessary to reduce the computational cost.

An alternative to direct structural analysis of huge models is based on component mode synthesis. Many component mode synthesis-based reduced-order modeling techniques have been published [6–12] because component mode synthesis can be combined with a wide variety of FEM-based methods. In the context of vibration analysis, component mode synthesis is used by first dividing the global structure into components. Next, each component is projected onto a very small truncated set of (component-level) basis vectors that approximately span the space of the (component-level) response. As a result, the number of DOFs required to model each component is considerably reduced compared to standard FEMs. Finally, the models of each component are assembled, and a global reduced-order model is synthesized. This last step can be performed in several ways. The most common approach is the fixed-interface Craig-Bampton component mode synthesis method [7]. Craig-Bampton component mode synthesis is well understood and frequently used because of its simplicity and numerical stability. Herein, Craig-Bampton component mode synthesis is used for the substructuring analysis.

Although many reduced-order models have been developed for structural analyses [18, 23–27], they are not constructed for design or damage detection in complex structures. The key element that separates reduced-order models for design from the rest is that usual reduced-order models cannot easily be re-constructed when changes are applied (by design or through damage) in a few components of the overall system. Recently, design-oriented reduced-order models have been developed to avoid prohibitively expensive reanalyses of complex structures. These recent models are referred to as parametric reduced-order models. For example, Balmes and co-workers [28, 29] calculated sets of modes for a few sample parameter values in the parameter space, and grouped them into a fixed augmented basis for the modes of the nominal system. This augmented basis was found to

be suitable for a (parametric) family of models. However, the need for repeatedly solving many sample eigenproblems makes the approach impractical for global parametric reduced-order models of realistic industrial FEMs. To accelerate solving the sampled eigenproblems, this technique was combined with a component-based approach by Zhang and Park [30, 31] for large FEMs. As a by-product, the eigenproblems of the sampled space are confined to one specific component, and the resulting global system is reduced substantially. However, in the projection phase, the component basis has to be expanded back into the global coordinates. Hence, the approach does not lead to true component-based parametric reduced-order models. To address that issue, substructural analysis techniques based on parametric reduced-order models have been developed [32]. However, those parametric reduced-order models can account for one parametric variability in one substructure only. In contrast, the new component parametric reduced-order models proposed herein allow several substructures to have parametric variability in characteristics such as geometric parameters (e.g. thickness), or material properties (e.g. Young's modulus). These new multiple-component parametric reduced-order models are obtained by managing the geometric compatibility conditions between substructures.

Geometric variations (e.g. dents in the structure, or thickness variability due to manufacturing) can be treated as parametric variability in the structure. Such an approach has been used for a few years for investigating the vibration of turbo-machinery bladed disks. For example, static mode compensation has been used for global models [33, 34] to compute the vibration response of a structure which has dents or missing material. By accounting for the effects of geometric variability as though they are produced by external forces, a set of basis vectors can be established using a combination of normal modes of the pristine structure compensated by static modes. However, the static mode compensation method for geometric variations has not been applied for substructuring. Herein,

component mode synthesis with static mode compensation is developed based on Craig-Bampton component mode synthesis. When substructures have dents, component mode synthesis with static mode compensation is applied to obtain the vibration response. Finally, the effects of parameter variations (e.g. thickness and geometric variations) are analyzed by multiple-component parametric reduced-order models and component mode synthesis with static mode compensation.

Typical FEM-based techniques for modeling cracks in complex structures lead to remarkably large models. Also, it is well known that system-level response characteristics (such as resonant frequencies) of cracked structures differ from their healthy counterparts. Hence, models which are accurate yet reduced-order are highly desirable for complex cracked structures. In general, a nonlinear analysis is needed to predict the vibration response of a cracked structure because the periodic opening and closing of the crack surfaces leads to a (piece-wise linear) nonlinear response. For that, Poudou and Pierre [36,37] have developed a hybrid frequency-time domain method. In that method, the resonant frequencies of the cracked structure are found by a forced response analysis which is a nonlinear problem whose solution is complex and computationally intensive. To alleviate this issue, the bi-linear frequency approximation (which was first used to predict resonant frequencies of single-DOF piece-wise linear systems [38]) is generalized to large dimensional models. The approach herein builds on the early methods for studying the vibration of cracked beams and plates using a multi-DOFs model. Chati *et al*. [39] have studied bi-linear frequency approximation for a two dimensional cracked beam, and Saito *et al*. [40] have used bi-linear frequency approximation for a three dimensional cracked plate. Note that the actual motion of the crack surfaces can be quite complex, and there may be more than two crack states (open and closed) when, for example, the crack closing proceeds gradually so that different regions of the crack surfaces close at different times. Although

the generalized bi-linear frequency approximation cannot capture the effects of gradual opening and closing, it can provide approximate values for the resonant frequencies of complex cracked structures by employing linear analyses only. Also, the linear analyses required in bi-linear frequency approximation can be performed using Craig-Bampton component mode synthesis, and that further reduces the computational cost.

The key novel contributions of this paper are as follows. First, the proposed multiple-component parametric reduced-order models are developed for cases where parameter variations occur simultaneously in multiple components by developing a novel transformation matrix. Second, the static mode compensation approach is adapted for use with Craig-Bampton component mode synthesis to create a novel component-level analysis. Third, the geometric compatibility conditions normally used in Craig-Bampton component mode synthesis are generalized and adapted so that bi-linear frequency approximation can be implemented efficiently for crack analysis in conjunction with Craig-Bampton component mode synthesis, component mode synthesis with static mode compensation and multiple-component parametric reduced-order models.

This paper is organized as follows. In Sec. 2.2, bi-linear frequency approximation and Craig-Bampton component mode synthesis for the cracked structure are discussed. Also, multiple-component parametric reduced-order models for structures which have multiple components with parametric variability, and component mode synthesis with static mode compensation for components with geometric variations (such as dents) are formulated. Next, the models for all substructures are assembled by using an effective computational approach to implement geometric compatibility conditions. In Sec. 2.3, numerical simulations are used to demonstrate the proposed methods for an L-shape structure which has several substructures with thickness variation and also substructures with damage (dents). Also, bi-linear frequency approximation is implemented for a cracked L-shape structure.

Next, the novel reduced-order modeling techniques are applied to a real vehicle model in Sec. 2.4. Finally, conclusions are summarized in Sec. 2.5.

2.2 Reduced-Order Modeling

2.2.1 Bi-linear frequency approximation and CB-CMS for cracked structures

Bi-linear systems are essentially nonlinear and the notions of natural frequencies and normal modes are, strictly speaking, not applicable. In this study we focus on the many cases where the forcing applied to the system is periodic and leads to a periodic response. Herein, the frequency corresponding to the response with the largest amplitude is referred to as a resonant response and its frequency is referred to as a resonant frequency. Note that the systems where penetration is allowed or the crack is considered closed are linear. In this work, we discuss a methodology to approximate the nonlinear resonant frequencies based on resonant frequencies of systems where penetration is allowed, or the crack is considered closed at all times. Herein, we consider bi-linear systems under harmonic excitation which are assumed to produce a periodic response. While periodic responses are certainly observed in many applications, they are not guaranteed to occur in all occasions. Even when periodic solutions are possible, there can be complicating features such as multiplicity of steady state responses and dependency on initial conditions. Such cases are exciting but are beyond the scope of this work.

Bi-linear frequency approximation

In this section, the bi-linear frequency approximation (BFA) is generalized and used to analyze three-dimensional cracked structures. Initially, BFA was used to provide approximate resonant frequencies for single-DOF piecewise linear (bi-linear) systems. In essence,

BFA can be expressed as [38]

$$\omega_b = \frac{2\omega_1\omega_2}{\omega_1 + \omega_2}, \tag{2.1}$$

where ω_b is the approximate resonant frequency, ω_1 is the resonant frequency of one of the linear systems associated with the piecewise linear system, and ω_2 is that of the other linear system of the piecewise linear system. This expression is the exact solution for the undamped oscillation of a piecewise linear (bi-linear) single-DOF oscillator. The application of Eq. (2.1) is more complex for more general cases such as cracked plates because in those cases multiple DOFs are located on the crack surfaces. Hence, the model involves multiple piecewise linear systems. Nevertheless, for many cases one can assume that the cracked system behaves as if it were defined by only two linear systems, corresponding to two states: one when the crack is fully open, and for when the crack fully is closed. In the following, these states are referred to as state 1 and state 2.

The definition of the states 1 and 2 can be extended to those proposed by Chati *et al.* [39], who analyzed the in-plane bending vibrations of a cracked beam. Specifically, state 1 (open crack) is defined by removing the constraint of no penetration of the crack surfaces. That is, for state 1 there is no constraint applied on the relative motion between the corresponding nodes (one on each crack surface) that are in contact when the crack is closed. Hence, for state 1, inter-penetration is allowed. Similarly, state 2 (closed crack) is defined by enforcing no penetration, but allowing sliding between the crack surfaces. That is, for state 2 the relative motion between the nodes (which are located on each of the two separate faces of the crack) is not allowed in the direction perpendicular to the crack surface. Their motion in the plane tangent to the crack surfaces is allowed. Hence, for state 2, sliding is allowed while inter-penetration is not allowed. The mathematical representation of these two states is detailed in below section.

CB-CMS for cracked structures

In this section, the fixed-interface Craig-Bampton CMS (CB-CMS) [7] method is used to construct reduced-order models (ROMs). This modeling approach is used because of its simplicity and computational stability. To apply CMS, the complex structure of interest is partitioned into substructures. The DOFs of each substructure are further partitioned into active DOFs on the interface (indicated by the superscript A), and omitted DOFs in the interior (indicated by the superscript O). The mass and stiffness matrices for a component i can then be partitioned to obtain

$$\mathbf{M}_i = \begin{bmatrix} \mathbf{m}_i^{AA} & \mathbf{m}_i^{AO} \\ \mathbf{m}_i^{OA} & \mathbf{m}_i^{OO} \end{bmatrix}, \quad \text{and} \quad \mathbf{K}_i = \begin{bmatrix} \mathbf{k}_i^{AA} & \mathbf{k}_i^{AO} \\ \mathbf{k}_i^{OA} & \mathbf{k}_i^{OO} \end{bmatrix}.$$

Next, the physical coordinates are changed to a set of coordinates representing the amplitudes of a selected set of fixed-interface component-level normal modes $\mathbf{\Phi}_i^N$ (indicated by the superscript N), and the amplitudes of the full set of static constraint modes $\mathbf{\Phi}_i^C = -\mathbf{k}_i^{OO^{-1}}\mathbf{k}_i^{OA}$ (indicated by the superscript C). The transformed mass and stiffness matrices for component i can be expressed as

$$\hat{\mathbf{M}}_i = \begin{bmatrix} \hat{\mathbf{m}}_i^{C} & \hat{\mathbf{m}}_i^{CN} \\ \hat{\mathbf{m}}_i^{NC} & \hat{\mathbf{m}}_i^{NN} \end{bmatrix}, \quad \text{and} \quad \hat{\mathbf{K}}_i = \begin{bmatrix} \hat{\mathbf{k}}_i^{C} & \hat{\mathbf{k}}_i^{CN} \\ \hat{\mathbf{k}}_i^{NC} & \hat{\mathbf{k}}_i^{NN} \end{bmatrix}. \tag{2.2}$$

To model the dynamics of cracked structures and to apply BFA, the substructuring is done such that all cracks are along boundaries between adjacent substructures. Hence, all crack surfaces are boundaries between substructures. Thus, in Eq. (2.2), the DOFs marked as C are obtained from interface DOFs (which are the interface DOFs for the i^{th} substructure). The interface DOFs are further divided into constraint DOFs (shown by superscript CC) and free DOFs (indicated by superscript FF) for BFA. For example, for state 1 (open crack), the DOFs on the crack surfaces are completely free (and the inter-penetration of

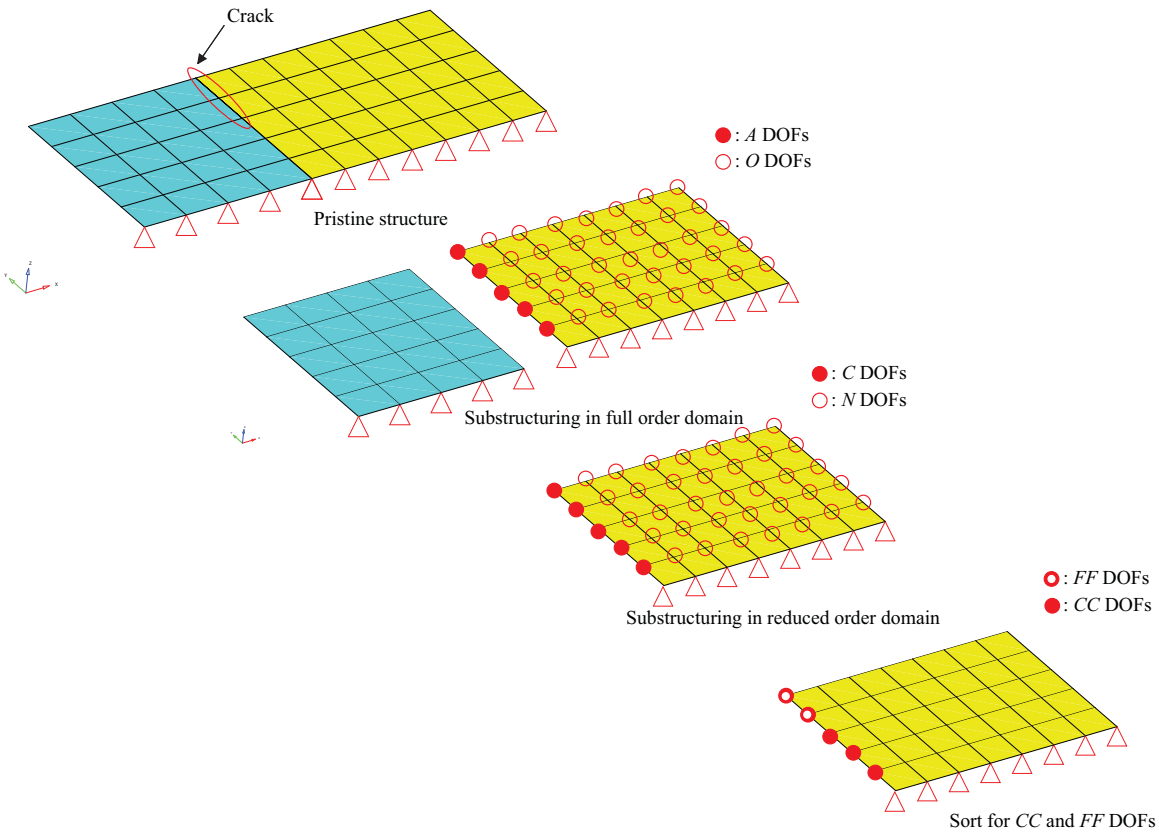

Figure 2.1: Conceptual view of the groups of DOFs corresponding to superscripts A, O, C, N, CC, and FF

crack surfaces is allowed). These DOFs on the crack surfaces (are free DOFs for state 1 and) are indicated by superscript FF in Eq. (2.3). For state 2 (closed crack), sliding boundary conditions are applied at the crack surfaces. Thus, the constrained DOFs (for sliding boundary conditions) are denoted by superscript CC in Eq. (2.3). Using these two kinds of geometric compatibility conditions, the frequencies ω_1 and ω_2 in Eq. (2.1) are obtained through two separate linear analyses. Thus, if component i has a crack surface,

the component-level mass and stiffness matrices are partitioned as

$$\begin{aligned} \hat{\mathbf{M}}_i &= \begin{bmatrix} \hat{\mathbf{m}}_i^{CC} & \hat{\mathbf{m}}_i^{CF} & \hat{\mathbf{m}}_i^{CCN} \\ \hat{\mathbf{m}}_i^{FC} & \hat{\mathbf{m}}_i^{FF} & \hat{\mathbf{m}}_i^{FFN} \\ \hat{\mathbf{m}}_i^{NCC} & \hat{\mathbf{m}}_i^{NFF} & \hat{\mathbf{m}}_i^{NN} \end{bmatrix} \quad \text{and} \\ \hat{\mathbf{K}}_i &= \begin{bmatrix} \hat{\mathbf{k}}_i^{CC} & \hat{\mathbf{k}}_i^{CF} & \hat{\mathbf{k}}_i^{CCN} \\ \hat{\mathbf{k}}_i^{FC} & \hat{\mathbf{k}}_i^{FF} & \hat{\mathbf{k}}_i^{FFN} \\ \hat{\mathbf{k}}_i^{NCC} & \hat{\mathbf{k}}_i^{NFF} & \hat{\mathbf{k}}_i^{NN} \end{bmatrix}. \end{aligned} \tag{2.3}$$

The notation contains many superscripts such as A, O, C, N, CC, and FF. To clarify the meaning of these superscripts, Fig. 2.1 provides a conceptual view of the groups of DOFs corresponding to these superscripts. Since all crack surfaces are at interfaces between components, the geometric compatibility conditions at the interfaces between substructures are applied only for the DOFs marked as CC in Eq. (2.3). For example, if a substructure does not have a crack surface, then there are no DOFs marked as FF, and all DOFs are marked as CC. Hence, the geometric compatibility conditions are applied to all DOFs marked as C in Eq. (2.2). In general, all DOFs on the boundaries are constrained *except* the DOFs corresponding to the crack surfaces. The DOFs along crack surfaces (denoted by FF) are not constrained. Also, note that all boundary DOFs are active DOFs, and the geometric compatibility conditions used to assemble every substructure are applied only to the DOFs marked as CC in Eq. (2.3).

2.2.2 Multiple-component parametric reduced-order models

Global Parametric reduced-order models (PROMs) [29] have been developed for fast reanalyses of structures with parametric variability in their properties. An important drawback of existing global PROMs is that they require computationally expensive calculations to determine multiple sets of system-level eigenvectors. These eigenvectors are needed

when multiple parameters are considered. Thus, component-mode-based PROMs [30] have been developed to adopt component normal modes and characteristic constraint modes as projection basis instead of global modes. However, constructing component-mode-based PROMs is also time consuming because the approach still requires the calculation of system-level (global) interface modes. These interface modes are needed for the secondary modal analysis performed on the system-level matrix partitions (corresponding to the interface DOFs) for all of the components in the global model. Thus, Park [32] introduced truly component-level analysis for constructing PROMs, referred to as component-PROMs. However, component-PROMs can be applied only to one component (and a single parametric variability). This issue is addressed herein by developing novel component-PROMs for multiple components. These new models can be used for cases where parametric variability (or damages) are present in several substructures simultaneously. For each substructure, a single variation is considered in parameters such as Young's modulus, or in geometric characteristics such as thickness. These models are referred to as multi-component PROMs (MC-PROMs).

A family of models can be defined as all models which differ only through a single parameter. Herein, we focus on families of component-level models first. Consider a family of models for parameter p for the i^{th} component of a (global) structure. The mass and stiffness matrices of the i^{th} component for this family of models can be approximated by using Taylor series. For example, for a linear thin plate element, the modification of the stiffness matrix due to variations in the thickness of the plate can be accurately represented by a Taylor series up to the third order, while the mass matrix can be approximated by a Taylor series up to first order, neglecting the rotary inertia [32]. The first and the third order Taylor series approximations about the nominal parameter value p_0 can be expressed

as follows

$$\begin{aligned}
\mathbf{M}_i(p) &\approx \mathbf{M}_i(p_0) + \frac{\partial \mathbf{M}_i}{\partial p}(p-p_0), \\
\mathbf{K}_i(p) &\approx \mathbf{K}_i(p_0) + \frac{\partial \mathbf{K}_i}{\partial p}(p-p_0) \\
&\quad + \frac{1}{2}\frac{\partial^2 \mathbf{K}_i}{\partial p^2}(p-p_0)^2 + \frac{1}{6}\frac{\partial^3 \mathbf{K}_i}{\partial p^3}(p-p_0)^3.
\end{aligned} \tag{2.4}$$

Computationally, the partial derivatives in Eq. (2.4) can be approximated using standard finite differences for a small parameter variation Δp as follows

$$\begin{aligned}
\mathbf{M}^1_{FD} &= \frac{\partial \mathbf{M}_i}{\partial p} \approx \frac{\mathbf{M}_i(p_0+\Delta p) - \mathbf{M}_i(p_0)}{\Delta p} \\
\mathbf{K}^1_{FD} &= \frac{\partial \mathbf{K}_i}{\partial p} \approx \frac{\mathbf{K}_i(p_0+\Delta p) - \mathbf{K}_i(p_0)}{\Delta p} \\
\mathbf{K}^2_{FD} &= \frac{\partial^2 \mathbf{K}_i}{\partial p^2} \approx \frac{\mathbf{K}_i(p_0+\Delta p) - 2\mathbf{K}_i(p_0) + \mathbf{K}_i(p_0-\Delta p)}{\Delta p^2} \\
\mathbf{K}^3_{FD} &= \frac{\partial^3 \mathbf{K}_i}{\partial p^3} \approx \frac{\mathbf{K}_i(p_0+2\Delta p) - 3\mathbf{K}_i(p_0+\Delta p) + 3\mathbf{K}_i(p_0) - \mathbf{K}_i(p_0-\Delta p)}{\Delta p^3}
\end{aligned} \tag{2.5}$$

Then, the parameterized component matrices can be obtained by substituting Eq. (2.5) into Eq. (2.4) to obtain

$$\begin{aligned}
\mathbf{M}_i(p) &\approx \mathbf{M}_i(p_0) + \mathbf{M}^1_{FD}(p-p_0), \\
\mathbf{K}_i(p) &\approx \mathbf{K}_i(p_0) + \mathbf{K}^1_{FD}(p-p_0) \\
&\quad + \frac{1}{2}\mathbf{K}^2_{FD}(p-p_0)^2 + \frac{1}{6}\mathbf{K}^3_{FD}(p-p_0)^3.
\end{aligned} \tag{2.6}$$

To obtain a ROM for a i^{th} component, each parametric family of component models is projected onto a (constant) component-level modal basis $\hat{\mathbf{\Phi}}_i$. This basis is calculated (for each component) at a few given (perturbed) sets of parameter values. This basis is used for all configurations in the parameter space of the corresponding component. The component-level modal basis $\hat{\mathbf{\Phi}}_i$ for i^{th} component can be expressed as

$$\hat{\mathbf{\Phi}}_i = \begin{bmatrix} \mathbf{I} & \mathbf{I} & \mathbf{0} \\ \mathbf{\Psi}_i^0 & \mathbf{\Psi}_i^U & \mathbf{\Phi}_i^{aug} \end{bmatrix}, \tag{2.7}$$

where $\mathbf{\Phi}_i^{aug}$ is referred to as the matrix of augmented fixed-interface normal modes

$$\mathbf{\Phi}_i^{aug} = \left[\begin{array}{cccc} \mathbf{\Phi}_i^0 & \mathbf{\Phi}_i^1 & \mathbf{\Phi}_i^2 & \mathbf{\Phi}_i^3 \end{array} \right], \tag{2.8}$$

and the superscript 0 indicates quantities computed for the nominal parameter values, while the superscript U, 1, 2 and 3 indicate quantities computed for perturbed parameter values (which can be, for example, $p + \Delta p$, $p + 2\Delta p$, and $p + 3\Delta p$). Vectors $\mathbf{\Phi}_i$ and $\mathbf{\Psi}_i$ in Eq. (2.7) represent fixed-interface normal modes and static constraint modes.

When the stiffness matrix is represented by a third order Taylor series, then the fixed-interface normal modes for three perturbed structures are computed to form a transformation matrix. In general, taken all together, the modes in $\mathbf{\Phi}_i^{aug}$ are not orthogonal. For numerical stability, an orthogonal basis for the space spanned by these modes is used. To that aim, the left singular vectors of Eq. (2.8) are computed, and the left singular vector $\mathbf{U}$ corresponding to singular values larger than 0.01% of the maximum singular values are selected. Next, $\mathbf{U}$ is used to construct a transformation matrix (instead of the augmented fixed-interface normal modes $\mathbf{\Phi}_i^{aug}$). The final transformation matrix can be expressed as

$$\hat{\mathbf{\Phi}}_i = \left[\begin{array}{ccc} \mathbf{I} & \mathbf{I} & \mathbf{0} \\ \\ \mathbf{\Psi}_i^0 & \mathbf{\Psi}_i^U & \mathbf{U}_i \end{array} \right], \tag{2.9}$$

Using Eq. (2.9) into Eq. (2.6), the physical coordinates are transformed to coordinates along the collected set of modes $\hat{\mathbf{\Phi}}_i$ for the i^{th} component. The transformed mass and stiffness matrices can be expressed as

$$\begin{aligned} \hat{\mathbf{M}}_i(p) &\approx \hat{\mathbf{\Phi}}_i^T \mathbf{M}_i(p_0) \hat{\mathbf{\Phi}}_i + \hat{\mathbf{\Phi}}_i^T \mathbf{M}_{FD}^1 \hat{\mathbf{\Phi}}_i (p - p_0), \\ \hat{\mathbf{K}}_i(p) &\approx \hat{\mathbf{\Phi}}_i^T \mathbf{K}_i(p_0) \hat{\mathbf{\Phi}}_i + \hat{\mathbf{\Phi}}_i^T \mathbf{K}_{FD}^1 \hat{\mathbf{\Phi}}_i (p - p_0) \\ &\quad + \frac{1}{2} \hat{\mathbf{\Phi}}_i^T \mathbf{K}_{FD}^2 \hat{\mathbf{\Phi}}_i (p - p_0)^2 + \frac{1}{6} \hat{\mathbf{\Phi}}_i^T \mathbf{K}_{FD}^3 \hat{\mathbf{\Phi}}_i (p - p_0)^3. \end{aligned}$$

The modal basis consists of internal and interface DOFs for each substructure. Thus,

the mass and stiffness matrices for the i^{th} component used for MC-PROM can be partitioned as follows

$$\mathbf{M}_i^{PROM} = \begin{bmatrix} \mathbf{m}_i^{C_{00}} & \mathbf{m}_i^{C_{0U}} & \mathbf{m}_i^{CN_{00}} \\ \mathbf{m}_i^{C_{U0}} & \mathbf{m}_i^{C_{UU}} & \mathbf{m}_i^{CN_{UU}} \\ \mathbf{m}_i^{NC_{00}} & \mathbf{m}_i^{NC_{UU}} & \mathbf{m}_i^{N_d} \end{bmatrix}, \tag{2.10}$$

$$\mathbf{K}_i^{PROM} = \begin{bmatrix} \mathbf{k}_i^{C_{00}} & \mathbf{k}_i^{C_{0U}} & \mathbf{k}_i^{CN_{00}} \\ \mathbf{k}_i^{C_{U0}} & \mathbf{k}_i^{C_{UU}} & \mathbf{k}_i^{CN_{UU}} \\ \mathbf{k}_i^{NC_{00}} & \mathbf{k}_i^{NC_{UU}} & \mathbf{k}_i^{N_d} \end{bmatrix}. \tag{2.11}$$

In addition, the interface DOFs are also divided into constrained DOFs (denoted by superscript CC) and free DOFs (denoted by superscript FF) to apply open and sliding boundary conditions for BFA as in Eq. (2.3). Thus, the interface DOFs marked as C can also be divided into CC and FF DOFs. Then, the MC-PROM mass and stiffness matrices can be partitioned as

$$\mathbf{M}_i^{PROM} = \begin{bmatrix} \mathbf{m}_i^{CC_{00}} & \mathbf{m}_i^{CF_{00}} & \mathbf{m}_i^{CC_{0U}} & \mathbf{m}_i^{CF_{0U}} & \mathbf{m}_i^{CCN_{00}} \\ \mathbf{m}_i^{FC_{00}} & \mathbf{m}_i^{FF_{00}} & \mathbf{m}_i^{FC_{0U}} & \mathbf{m}_i^{FF_{0U}} & \mathbf{m}_i^{FFN_{00}} \\ \mathbf{m}_i^{CC_{U0}} & \mathbf{m}_i^{CF_{U0}} & \mathbf{m}_i^{CC_{UU}} & \mathbf{m}_i^{CF_{UU}} & \mathbf{m}_i^{CCN_{UU}} \\ \mathbf{m}_i^{FC_{U0}} & \mathbf{m}_i^{FF_{U0}} & \mathbf{m}_i^{FC_{UU}} & \mathbf{m}_i^{FF_{UU}} & \mathbf{m}_i^{FFN_{UU}} \\ \mathbf{m}_i^{NCC_{00}} & \mathbf{m}_i^{NFF_{00}} & \mathbf{m}_i^{NCC_{UU}} & \mathbf{m}_i^{NFF_{UU}} & \mathbf{m}_i^{N_d} \end{bmatrix}, \tag{2.12}$$

$$\mathbf{K}_i^{PROM} = \begin{bmatrix} \mathbf{k}_i^{CC_{00}} & \mathbf{k}_i^{CF_{00}} & \mathbf{k}_i^{CC_{0U}} & \mathbf{k}_i^{CF_{0U}} & \mathbf{k}_i^{CCN_{00}} \\ \mathbf{k}_i^{FC_{00}} & \mathbf{k}_i^{FF_{00}} & \mathbf{k}_i^{FC_{0U}} & \mathbf{k}_i^{FF_{0U}} & \mathbf{k}_i^{FFN_{00}} \\ \mathbf{k}_i^{CC_{U0}} & \mathbf{k}_i^{CF_{U0}} & \mathbf{k}_i^{CC_{UU}} & \mathbf{k}_i^{CF_{UU}} & \mathbf{k}_i^{CCN_{UU}} \\ \mathbf{k}_i^{FC_{U0}} & \mathbf{k}_i^{FF_{U0}} & \mathbf{k}_i^{FC_{UU}} & \mathbf{k}_i^{FF_{UU}} & \mathbf{k}_i^{FFN_{UU}} \\ \mathbf{k}_i^{NCC_{00}} & \mathbf{k}_i^{NFF_{00}} & \mathbf{k}_i^{NCC_{UU}} & \mathbf{k}_i^{NFF_{UU}} & \mathbf{k}_i^{N_d} \end{bmatrix}. \tag{2.13}$$

2.2.3 Component mode synthesis with static mode compensation

In this section, a novel, component-based modeling technique for systems containing dents is formulated using a mode-acceleration method based on static mode compensation (SMC). Lim *et al.* [34] used this modeling technique for structures with geometric variation. However, that SMC technique was applied to global structural analysis and not to substructural analysis. Herein, an SMC technique is developed for substructural analysis. The resulting reduced-order modeling method is referred to as component mode synthesis with static mode compensation (SMC-CMS). Note that, although this procedure is formally similar to CB-CMS, the bases used are distinct.

The mass and stiffness matrices of the i^{th} dented substructure can be expressed as

$$\mathbf{M}_i^D = \begin{bmatrix} \mathbf{m}_i^{AA^D} & \mathbf{m}_i^{AO^D} \\ \mathbf{m}_i^{OA^D} & \mathbf{m}_i^{OO^D} \end{bmatrix}, \quad \text{and} \quad \mathbf{K}_i^D = \begin{bmatrix} \mathbf{k}_i^{AA^D} & \mathbf{k}_i^{AO^D} \\ \mathbf{k}_i^{OA^D} & \mathbf{k}_i^{OO^D} \end{bmatrix},$$

where the DOFs of each substructure have been partitioned into active DOFs on the interface (indicated by the superscript A), and omitted DOFs in the interior (indicated by the superscript O).

In the CB-CMS method, a selected set of fixed-interface component-level normal modes $\mathbf{\Phi}_i^N$ are obtained using the component-level mass and stiffness matrices $\mathbf{M}_i$ and $\mathbf{K}_i$. In contrast, in the SMC-CMS method, a truncated/selected set of fixed-interface normal modes calculated using SMC are used. Hence, the normal modes of the pristine / healthy substructure are compensated by using static modes. To that aim, the changes in the mass and stiffness matrices due to the presence of the dent are expressed as $\mathbf{M}_i^\delta = \mathbf{M}_i^D - \mathbf{M}_i^H$, and $\mathbf{K}_i^\delta = \mathbf{K}_i^D - \mathbf{K}_i^H$, where the superscripts D and H indicate dented and healthy substructures.

The active DOFs (which are interface DOFs between substructures) are needed for applying the geometric compatibility conditions. In addition to those DOFs, there are

other active DOFs which have to be considered. These other active DOFs (indicated by the subscript Γ) are DOFs affected the dent. These DOFs are needed to model the attachment modes used in the SMC-CMS method. The attachment modes $\mathbf{\Psi}^H$ are obtained using the DOFs marked as Γ together with the omitted DOFs.

One physical interpretation of SMC is that an equivalent force is applied to the structure to account for the changes in dynamics due to the dent. This equivalent force [33, 34] can be expressed as

$$\mathbf{f}_{ij} = \left(-\omega_{ij}^{H\,2}\mathbf{M}_i^{OO^D} + \mathbf{K}_i^{OO^D}\right)\mathbf{\Phi}_{ij}^H = \begin{bmatrix} \mathbf{0} \\ \left(-\omega_{ij}^{H\,2}\mathbf{M}_i^{OO^\delta} + \mathbf{K}_i^{OO^\delta}\right)\mathbf{\Phi}_{\Gamma,ij}^H \end{bmatrix},$$

where ω_{ij}^H and $\mathbf{\Phi}_{ij}^H$ are the j^{th} natural frequency and mode shape of the i^{th} healthy substructure, and $\mathbf{\Phi}_{\Gamma,ij}^H$ are the portions of $\mathbf{\Phi}_{ij}^H$ which correspond to the DOFs where a dent is present (i.e. the DOFs marked as Γ). The static modes used in SMC are defined by $\mathbf{K}_i^{D^{-1}}\mathbf{f}_{ij}$, and can be obtained using the following relation [33, 34]

$$\mathbf{K}_i^{D^{-1}}\mathbf{f}_{ij} = \mathbf{K}_i^{H^{-1}}\left(\mathbf{I} + \mathbf{K}_i^\delta\mathbf{K}_i^{H^{-1}}\right)^{-1}\mathbf{f}_{ij} = \mathbf{K}_i^{H^{-1}}\mathbf{g}_{ij}, \tag{2.14}$$

where

$$\mathbf{g}_{ij} = \left(\mathbf{I} + \mathbf{K}_i^\delta\mathbf{K}_i^{H^{-1}}\right)^{-1}\mathbf{f}_{ij}.$$

Eq. (2.14) shows that the static modes can be obtained by a static analysis where the (static) forces $\mathbf{f}_{ij}$ are applied to the dented substructure, or the (static) forces $\mathbf{g}_{ij}$ are applied to the healthy substructure. Also, these static modes can be computed as a linear combination of healthy-structure attachment modes with the coefficients being the corresponding forces, that is

$$\mathbf{K}^{D^{-1}}\mathbf{f}_{ij} = \mathbf{K}^{H^{-1}}\mathbf{g}_{ij} = \mathbf{\Psi}^H\mathbf{g}_{\Gamma,ij}.$$

Finally, the truncated set of component-level normal modes for the healthy substructure (compensated by static modes) can be obtained as

$$\mathbf{\Phi}_i^{SMC} = \mathbf{\Phi}_i^H - \mathbf{\Psi}_i^H \mathbf{G}_{\Gamma,i}.$$

This set of modes is used in SMC-CMS to construct ROMs. The resulting ROMs are similar to the ones obtained using fixed-interface normal modes in CB-CMS.

Using the truncated set of normal modes $\mathbf{\Phi}_i^{SMC}$, the reduced mass and stiffness matrices can be expressed as follows

$$\mathbf{M}_i^{SMC} = \begin{bmatrix} \mathbf{m}_i^C & \mathbf{m}_i^{C,SMC} \\ \mathbf{m}_i^{SMC,C} & \mathbf{m}_i^{SMC} \end{bmatrix}, \tag{2.15}$$

$$\mathbf{K}_i^{SMC} = \begin{bmatrix} \mathbf{k}_i^C & \mathbf{k}_i^{C,SMC} \\ \mathbf{k}_i^{SMC,C} & \mathbf{k}_i^{SMC} \end{bmatrix}, \tag{2.16}$$

where the superscript C refers to constraint modes, and

$$\begin{aligned} \mathbf{m}_i^C &= \mathbf{m}_i^{AA^D} + \mathbf{\Psi}_i^C \mathbf{m}_i^{OA^D} + \mathbf{\Psi}_i^{C^T} \mathbf{m}_i^{OO^D} \mathbf{\Psi}_i^{C^T}, \\ \mathbf{m}_i^{C,SMC} &= \mathbf{m}_i^{AO^D} \mathbf{\Phi}_i^{SMC} + \mathbf{\Psi}_i^{C^T} \mathbf{m}_i^{OO^D} \mathbf{\Phi}_i^{SMC}, \\ \mathbf{m}_i^{SMC,C} &= \mathbf{M}_i^{C,SMC^T}, \\ \mathbf{m}_i^{SMC} &= \mathbf{\Phi}_i^{SMC^T} \mathbf{m}_i^{OO^D} \mathbf{\Phi}_i^{SMC}, \end{aligned} \tag{2.17}$$

The formulas for the stiffness matrices are similar to those for the mass matrices (and are omitted here for the sake of brevity).

Similar to the CB-CMS and MC-PROM matrices used for BFA, the DOFs marked as C can be partitioned into CC and FF DOFs. One obtains

$$\mathbf{M}_j^{SMC} = \begin{bmatrix} \mathbf{m}_j^{CC} & \mathbf{m}_j^{CF} & \mathbf{m}_j^{CC,SMC} \\ \mathbf{m}_j^{FC} & \mathbf{m}_j^{FF} & \mathbf{m}_j^{FF,SMC} \\ \mathbf{m}_j^{SMC,CC} & \mathbf{m}_j^{SMC,FF} & \mathbf{m}_j^{SMC} \end{bmatrix}, \tag{2.18}$$

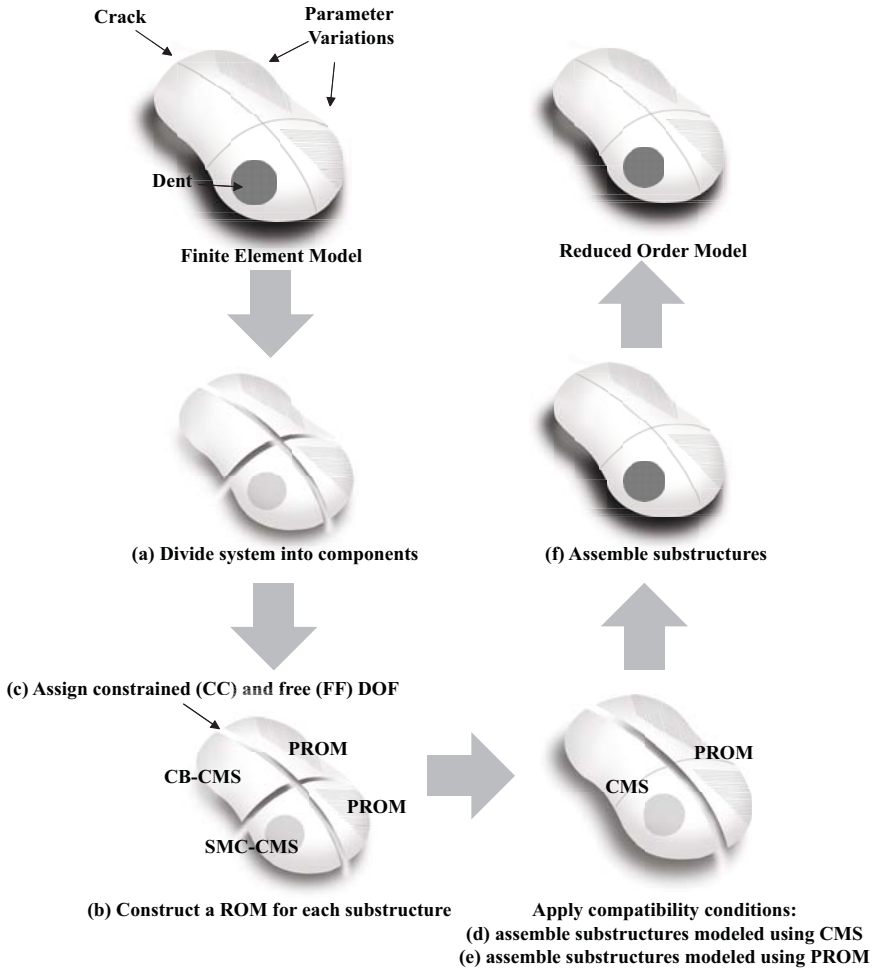

Figure 2.2: Conceptual diagram depicting the process of building a PROM

$$\mathbf{K}_j^{SMC} = \begin{bmatrix} \mathbf{k}_j^{CC} & \mathbf{k}_j^{CF} & \mathbf{k}_j^{CC,SMC} \\ \mathbf{k}_j^{FC} & \mathbf{k}_j^{FF} & \mathbf{k}_j^{FF,SMC} \\ \mathbf{k}_j^{SMC,CC} & \mathbf{k}_j^{SMC,FF} & \mathbf{k}_j^{SMC} \end{bmatrix}. \tag{2.19}$$

2.2.4 Geometric compatibility conditions for MC-PROM, CB-CMS and SMC-CMS

In MC-PROM, the component-level mass and stiffness matrices are spanned by matrices corresponding to the nominal and the perturbed parameters. Hence, the interface DOFs (indicated by the superscript C) of the substructure are not the same in MC-PROM

as in CB-CMS and SMC-CMS.

The component-level matrices used in CB-CMS and SMC-CMS (given in Eqs. (2.2), (2.15) and (2.16)) have single interface parts, so in this Section, CMS indicates both CB-CMS and SMC-CMS. However, in Eqs. (2.10) and (2.11), one may note that the interface parts of the PROM matrices are twice as many as those of the mass and stiffness matrices used in CB-CMS and SMC-CMS. Thus, geometric compatibility conditions are enforced to assemble these matrices (CB-CMS, SMC-CMS and MC-PROM), as described next.

Fig. 2.2 shows the procedure used to construct a PROM. In particular, reduced-order modeling techniques are applied to each substructure, and then geometric compatibility conditions are enforced. The process may be summarized as follows: (a) the system matrix is divided into components according to the type of parameter variation and/or damage, (b) a ROM is constructed for each substructure, (c) the constrained (CC) and free (FF) DOFs are assigned for the substructures which have crack surfaces at their interface with other components, (d) substructures modeled using the CB-CMS or the SMC-CMS approach are assembled, (e) substructures modeled using the PROM approach are assembled, and (f) the partially assembled structure modeled using CB-CMS or SMC-CMS, and the partially assembled structure modeled using PROM are assembled together. Note that when each substructure is assembled, the geometric compatibility conditions are applied to the DOFs marked as CC. A more detailed description of this procedure is as follows.

MC-PROM is applied for the design of the parts of the structure which have parametric variability, and CB-CMS is applied for the remainder of the structure. This remainder is the full structure minus the parameterized components (which are the components of interest in the design process, referred to as design components). In addition, SMC-CMS is applied for dented components.

Recall that the SMC-CMS method is similar to CB-CMS except that it uses a different

truncated set of (component-level) normal modes. Hence, the interface parts for SMC-CMS and CB-CMS have the same meaning. Thus, dented components can be grouped together with the remainder of the structure for the purpose of applying geometric compatibility conditions.

In general, a complex structure has remainder substructures and substructures which have parameter variability. First, CB-CMS is applied for the nominal components, and SMC-CMS is applied for the dented components. Next, consider that a crack exists between substructure i (a reminder substructure where CMS is applied) and substructure j (a substructure which has parameter variability and where MC-PROM is applied). Then, the DOFs marked as FF are assigned only for matrices of substructures i and j for the purpose of applying BFA. The complete, reduced-order, component-level equations of motion for each component based on CB-CMS, SMC-CMS and MC-PROM can be expressed as follows

$$\begin{aligned} \mathbf{M}_i^{CMS}\ddot{\mathbf{q}}_i^{CMS} + \mathbf{K}_i^{CMS}\mathbf{q}_i^{CMS} &= \mathbf{F}_i^{CMS}, (i = 1, 2, \cdots), \\ &\vdots \\ \mathbf{M}_j^{PROM}\ddot{\mathbf{q}}_j^{PROM} + \mathbf{K}_j^{PROM}\mathbf{q}_j^{PROM} &= \mathbf{F}_j^{PROM}, (j = 1, 2, \cdots). \end{aligned}$$

To apply the interface compatibility conditions, the equations above are grouped into one global equation of motion. The resulting mass and stiffness matrices, and the forcing vector can be expressed as

$$\hat{\mathbf{M}} = \mathbf{Bdiag}\left[\begin{array}{ccccccc} \mathbf{M}_1^{CMS} & \mathbf{M}_2^{CMS} & \cdots & \mathbf{M}_1^{PROM} & \mathbf{M}_2^{PROM} & \cdots \end{array}\right], \tag{2.20}$$

$$\hat{\mathbf{K}} = \mathbf{Bdiag}\left[\begin{array}{ccccccc} \mathbf{K}_1^{CMS} & \mathbf{K}_2^{CMS} & \cdots & \mathbf{K}_1^{PROM} & \mathbf{K}_2^{PROM} & \cdots \end{array}\right], \tag{2.21}$$

$$\hat{\mathbf{F}} = \left[\begin{array}{ccccccc} \mathbf{F}_1^{CMS^{\mathrm{T}}} & \mathbf{F}_2^{CMS^{\mathrm{T}}} & \cdots & \mathbf{F}_1^{PROM^{\mathrm{T}}} & \mathbf{F}_2^{PROM^{\mathrm{T}}} & \cdots \end{array}\right]^{\mathrm{T}}, \tag{2.22}$$

where $\mathbf{Bdiag}[.]$ denotes a block-diagonal matrix.

The first set of geometric compatibility conditions for CMS and MC-PROM are expressed (separately) as

$$\begin{aligned} \mathbf{q}^{CC_r} &= \mathbf{q}_1^{CC_r} + \mathbf{q}_2^{CC_r} + \cdots, \\ \mathbf{q}^{CC_d{}^{00}} &= \mathbf{q}_1^{CC_d{}^{00}} + \mathbf{q}_2^{CC_d{}^{00}} + \cdots, \\ \mathbf{q}^{CC_d{}^{UU}} &= \mathbf{q}_1^{CC_d{}^{UU}} + \mathbf{q}_2^{CC_d{}^{UU}} + \cdots, \end{aligned} \tag{2.23}$$

where the subscript r indicates components of the remainder of the structure, and the superscript 0 indicates quantities computed for the nominal parameter values, while the superscript U indicates quantities computed for perturbed parameter values (which can be, for example, the upper limits for the parameters of interest). Note that the geometric compatibility conditions are applied only for the constrained DOF.

Eq. (2.23) are applied into Eqs. (2.20) - (2.22) to assemble the matrices for CMS and MC-PROM, one part at a time. Then, these mass and stiffness matrices are assembled to obtain the full system-level matrices and forcing vector as

$$\bar{\hat{\mathbf{M}}} = \mathbf{Bdiag}\left[\begin{array}{cc} \mathbf{M}_{CMS} & \mathbf{M}_{PROM} \end{array}\right], \tag{2.24}$$

$$\bar{\hat{\mathbf{K}}} = \mathbf{Bdiag}\left[\begin{array}{cc} \mathbf{K}_{CMS} & \mathbf{K}_{PROM} \end{array}\right], \tag{2.25}$$

$$\bar{\hat{\mathbf{F}}} = \left[\begin{array}{cc} \mathbf{F}_{CMS}{}^{\mathrm{T}} & \mathbf{F}_{PROM}{}^{\mathrm{T}} \end{array}\right]^{\mathrm{T}}, \tag{2.26}$$

where

$$\mathbf{M}_{CMS} = \left[\begin{array}{ccc} \mathbf{M}_{CMS}^{CC_r} & \mathbf{M}_i^{CF_r} & \mathbf{M}_{CMS}^{CCN_r} \\ \mathbf{M}_i^{FC_r} & \mathbf{M}_i^{FF_r} & \mathbf{M}_{CMS}^{FFN_r} \\ \mathbf{M}_{CMS}^{NCC_r} & \mathbf{M}_{CMS}^{NFF_r} & \mathbf{M}_{CMS}^{NN_r} \end{array}\right],$$

$$\mathbf{K}_{CMS} = \begin{bmatrix} \mathbf{K}_{CMS}^{CC_r} & \mathbf{K}_{j}^{CF_r} & \mathbf{K}_{CMS}^{CCN_r} \\ \mathbf{K}_{j}^{FC_r} & \mathbf{K}_{j}^{FF_r} & \mathbf{K}_{CMS}^{FFN_r} \\ \mathbf{K}_{CMS}^{NCC_r} & \mathbf{K}_{CMS}^{NFF_r} & \mathbf{K}_{CMS}^{NN_r} \end{bmatrix}, \; \mathbf{F}_{CMS} = \begin{bmatrix} \mathbf{f}_1^{CC_r} + \mathbf{f}_2^{CC_r} + \cdots \\ \mathbf{f}_i^{FF_r} \\ \mathbf{f}_1^{NN_r} \\ \mathbf{f}_2^{NN_r} \\ \vdots \end{bmatrix},$$

$$\mathbf{M}_{PROM} = \begin{bmatrix} \mathbf{M}_{PROM}^{CC_{00}} & \mathbf{M}_{PROM}^{CC_{0U}} & \mathbf{M}_{j}^{CF_{00}} & \mathbf{M}_{j}^{CF_{0U}} & \mathbf{M}_{PROM}^{CCN_{00}} \\ \mathbf{M}_{PROM}^{CC_{U0}} & \mathbf{M}_{PROM}^{CC_{UU}} & \mathbf{M}_{j}^{CF_{UO}} & \mathbf{M}_{j}^{CF_{UU}} & \mathbf{M}_{PROM}^{CCN_{UU}} \\ \mathbf{M}_{PROM}^{FC_{00}} & \mathbf{M}_{PROM}^{FC_{0U}} & \mathbf{M}_{j}^{FF_{00}} & \mathbf{M}_{j}^{FF_{0U}} & \mathbf{M}_{PROM}^{FFN_{00}} \\ \mathbf{M}_{PROM}^{FC_{U0}} & \mathbf{M}_{PROM}^{FC_{UU}} & \mathbf{M}_{j}^{FF_{U0}} & \mathbf{M}_{j}^{FF_{UU}} & \mathbf{M}_{PROM}^{FFN_{UU}} \\ \mathbf{M}_{PROM}^{NCC_{00}} & \mathbf{M}_{PROM}^{NCC_{UU}} & \mathbf{M}_{j}^{NFF_{00}} & \mathbf{M}_{j}^{NF_{UU}} & \mathbf{M}_{PROM}^{NN_d} \end{bmatrix},$$

$$\mathbf{K}_{PROM} = \begin{bmatrix} \mathbf{K}_{PROM}^{CC_{00}} & \mathbf{K}_{PROM}^{CC_{0U}} & \mathbf{K}_{j}^{CF_{00}} & \mathbf{K}_{j}^{CF_{0U}} & \mathbf{K}_{PROM}^{CCN_{00}} \\ \mathbf{K}_{PROM}^{CC_{U0}} & \mathbf{K}_{PROM}^{CC_{UU}} & \mathbf{K}_{j}^{CF_{UO}} & \mathbf{K}_{j}^{CF_{UU}} & \mathbf{K}_{PROM}^{CCN_{UU}} \\ \mathbf{K}_{PROM}^{FC_{00}} & \mathbf{K}_{PROM}^{FC_{0U}} & \mathbf{K}_{j}^{FF_{00}} & \mathbf{K}_{j}^{FF_{0U}} & \mathbf{K}_{PROM}^{FFN_{00}} \\ \mathbf{K}_{PROM}^{FC_{U0}} & \mathbf{K}_{PROM}^{FC_{UU}} & \mathbf{K}_{j}^{FF_{U0}} & \mathbf{K}_{j}^{FF_{UU}} & \mathbf{K}_{PROM}^{FFN_{UU}} \\ \mathbf{K}_{PROM}^{NCC_{00}} & \mathbf{K}_{PROM}^{NCC_{UU}} & \mathbf{K}_{j}^{NFF_{00}} & \mathbf{K}_{j}^{NF_{UU}} & \mathbf{K}_{PROM}^{NN_d} \end{bmatrix},$$

$$\mathbf{F}_{PROM} = \begin{bmatrix} \mathbf{f}_1^{CC_{00}} + \cdots + \mathbf{f}_N^{CC_{00}} \\ \mathbf{f}_1^{CC_{UU}} + \cdots + \mathbf{f}_N^{CC_{UU}} \\ \mathbf{f}_j^{FF_{00}} \\ \mathbf{f}_j^{FF_{UU}} \\ \mathbf{f}_1^{NN_d} \\ \mathbf{f}_2^{NN_d} \\ \vdots \end{bmatrix}.$$

Although the boundary DOFs in the MC-PROM matrices are duplicated for the nominal and perturbed parameter parts, each relative displacement between DOFs of adjacent substructures is still the same for CMS and MC-PROM. Therefore, a second set of geometric compatibility conditions is given by

$$\mathbf{q}_1^{CC_r} + \mathbf{q}_3^{CC_r} + \cdots + \mathbf{q}_L^{CC_r} = \mathbf{q}_2^{CC_{00}} + \mathbf{q}_2^{CC_{UU}} + \cdots + \mathbf{q}_N^{CC_{00}} + \mathbf{q}_N^{CC_{UU}}, \quad \text{or}$$

$$\mathbf{q}^{CC_r} = \mathbf{q}^{CC_{00}} + \mathbf{q}^{CC_{UU}} = \mathbf{q}^{CC_d}.$$

By applying this second set of geometric compatibility conditions into Eqs. (2.24) - (2.26), the CMS and MC-PROM matrices and forcing vector can be rearranged to obtain the full system-level matrices as

$$\mathbf{M}_{sys} = \begin{bmatrix} \mathbf{M}^{CC} & \mathbf{M}^{CF} & \mathbf{M}^{CCN} \\ \mathbf{M}^{FC} & \mathbf{M}^{FF} & \mathbf{M}^{FFN} \\ \mathbf{M}^{NCC} & \mathbf{M}^{NFF} & \mathbf{M}^{NN} \end{bmatrix}, \tag{2.27}$$

$$\mathbf{K}_{sys} = \begin{bmatrix} \mathbf{K}^{CC} & \mathbf{K}^{CF} & \mathbf{K}^{CCN} \\ \mathbf{K}^{FC} & \mathbf{K}^{FF} & \mathbf{K}^{FFN} \\ \mathbf{K}^{NCC} & \mathbf{K}^{NFF} & \mathbf{K}^{NN} \end{bmatrix}, \tag{2.28}$$

$$\mathbf{F}_{sys} = \begin{bmatrix} \mathbf{f}^{CC^{\mathrm{T}}} & \mathbf{f}^{FF^{\mathrm{T}}} & \mathbf{f}^{NN^{\mathrm{T}}} \end{bmatrix}^{\mathrm{T}}, \tag{2.29}$$

where

$$\mathbf{M}^{CC} = \begin{bmatrix} \mathbf{M}_{00}^{CC} & \mathbf{M}_{0U}^{CC} \\ \mathbf{M}_{U0}^{CC} & \mathbf{M}_{UU}^{CC} \end{bmatrix},$$

$$\mathbf{M}^{CF} = \begin{bmatrix} \mathbf{M}_i^{CF} & \mathbf{M}_j^{CF_{00}} & \mathbf{M}_j^{CF_{0U}} \\ \mathbf{M}_i^{CF} & \mathbf{M}_j^{CF_{U0}} & \mathbf{M}_j^{CF_{UU}} \end{bmatrix},$$

$$\mathbf{M}^{CCN} = \begin{bmatrix} \mathbf{m}_1^{C_r N_r} & \mathbf{m}_2^{C_r N_r} & \cdots & \mathbf{m}_1^{C_0 N_d} & \mathbf{m}_2^{C_0 N_d} & \cdots \\ \mathbf{m}_1^{C_r N_r} & \mathbf{m}_2^{C_r N_r} & \cdots & \mathbf{m}_1^{C_U N_d} & \mathbf{m}_2^{C_U N_d} & \cdots \end{bmatrix},$$

$$\mathbf{M}^{FC} = \mathbf{M}^{CF^T},$$

$$\mathbf{M}^{FF} = \begin{bmatrix} \mathbf{M}_i^{FF} & \mathbf{0} & \mathbf{0} \\ \mathbf{0} & \mathbf{M}_j^{FF_{00}} & \mathbf{M}_j^{FF_{0U}} \\ \mathbf{0} & \mathbf{M}_j^{FF_{0U}} & \mathbf{M}_j^{FF_{UU}} \end{bmatrix},$$

$$\mathbf{M}^{FFN} = \begin{bmatrix} \mathbf{m}_i^{FFN_r} & \mathbf{0} & \cdots & \mathbf{0} & \mathbf{0} & \cdots & \mathbf{0} \\ \mathbf{0} & \mathbf{0} & \cdots & \mathbf{0} & \mathbf{M}_j^{FFN_{00}} & \cdots & \mathbf{0} \\ \mathbf{0} & \mathbf{0} & \cdots & \mathbf{0} & \mathbf{M}_j^{FFN_{UU}} & \cdots & \mathbf{0} \end{bmatrix},$$

$$\mathbf{M}^{NCC} = \mathbf{M}^{CCN^T}, \ \mathbf{M}^{NFF} = \mathbf{M}^{FFN^T},$$

$$\mathbf{M}^{N} = \begin{bmatrix} \mathbf{m}_1^{NN_r} & \mathbf{0} & \mathbf{0} & \mathbf{0} & \mathbf{0} & \mathbf{0} \\ \mathbf{0} & \mathbf{m}_2^{NN_r} & \mathbf{0} & \mathbf{0} & \mathbf{0} & \mathbf{0} \\ \mathbf{0} & \mathbf{0} & \ddots & \mathbf{0} & \mathbf{0} & \mathbf{0} \\ \mathbf{0} & \mathbf{0} & \mathbf{0} & \mathbf{m}_1^{NN_d} & \mathbf{0} & \mathbf{0} \\ \mathbf{0} & \mathbf{0} & \mathbf{0} & \mathbf{0} & \mathbf{m}_2^{NN_d} & \mathbf{0} \\ \mathbf{0} & \mathbf{0} & \mathbf{0} & \mathbf{0} & \mathbf{0} & \ddots \end{bmatrix},$$

$$\mathbf{K}^{CC} = \begin{bmatrix} \mathbf{K}_{00}^{CC} & \mathbf{K}_{0U}^{CC} \\ \mathbf{K}_{U0}^{CC} & \mathbf{K}_{UU}^{CC} \end{bmatrix},$$

$$\mathbf{K}^{CF} = \begin{bmatrix} \mathbf{K}_i^{CF} & \mathbf{K}_j^{CF_{00}} & \mathbf{K}_j^{CF_{0U}} \\ \mathbf{K}_i^{CF} & \mathbf{K}_j^{CF_{U0}} & \mathbf{K}_j^{CF_{UU}} \end{bmatrix},$$

$$\mathbf{K}^{CCN} = \begin{bmatrix} \mathbf{k}_1^{C_r N_r} & \mathbf{k}_2^{C_r N_r} & \cdots & \mathbf{k}_1^{C_0 N_d} & \mathbf{k}_2^{C_0 N_d} & \cdots \\ \mathbf{k}_1^{C_r N_r} & \mathbf{k}_2^{C_r N_r} & \cdots & \mathbf{k}_1^{C_U N_d} & \mathbf{k}_2^{C_U N_d} & \cdots \end{bmatrix},$$

$$\mathbf{K}^{FC} = \mathbf{K}^{CF^T},$$

$$\mathbf{K}^{FF} = \begin{bmatrix} \mathbf{K}_i^{FF} & \mathbf{0} & \mathbf{0} \\ \mathbf{0} & \mathbf{K}_j^{FF_{00}} & \mathbf{K}_j^{FF_{0U}} \\ \mathbf{0} & \mathbf{K}_j^{FF_{0U}} & \mathbf{K}_j^{FF_{UU}} \end{bmatrix},$$

$$\mathbf{K}^{FFN} = \begin{bmatrix} \mathbf{k}_i^{FFN_r} & \mathbf{0} & \cdots & \mathbf{0} & \mathbf{0} & \cdots & \mathbf{0} \\ \mathbf{0} & \mathbf{0} & \cdots & \mathbf{0} & \mathbf{K}_j^{FFN_{00}} & \cdots & \mathbf{0} \\ \mathbf{0} & \mathbf{0} & \cdots & \mathbf{0} & \mathbf{K}_j^{FFN_{UU}} & \cdots & \mathbf{0} \end{bmatrix},$$

$$\mathbf{K}^{NCC} = \mathbf{K}^{CCN^T},\ \mathbf{K}^{NFF} = \mathbf{K}^{FFN^T},$$

$$\mathbf{K}^{N} = \begin{bmatrix} \mathbf{k}_1^{NN_r} & \mathbf{0} & \mathbf{0} & \mathbf{0} & \mathbf{0} & \mathbf{0} \\ \mathbf{0} & \mathbf{k}_2^{NN_r} & \mathbf{0} & \mathbf{0} & \mathbf{0} & \mathbf{0} \\ \mathbf{0} & \mathbf{0} & \ddots & \mathbf{0} & \mathbf{0} & \mathbf{0} \\ \mathbf{0} & \mathbf{0} & \mathbf{0} & \mathbf{k}_1^{NN_d} & \mathbf{0} & \mathbf{0} \\ \mathbf{0} & \mathbf{0} & \mathbf{0} & \mathbf{0} & \mathbf{k}_2^{NN_d} & \mathbf{0} \\ \mathbf{0} & \mathbf{0} & \mathbf{0} & \mathbf{0} & \mathbf{0} & \ddots \end{bmatrix},$$

$$\mathbf{F}^{CC} = \begin{bmatrix} \mathbf{f}_1^{CC_r} + \mathbf{f}_2^{CC_r} + \cdots + \mathbf{f}_1^{CC_0} + \mathbf{f}_2^{CC_0} + \cdots \\ \mathbf{f}_1^{CC_r} + \mathbf{f}_2^{CC_r} + \cdots + \mathbf{f}_1^{CC_U} + \mathbf{f}_2^{CC_U} + \cdots \end{bmatrix},$$

$$\mathbf{F}^{FF} = \begin{bmatrix} \mathbf{f}_i^{FF} \\ \mathbf{f}_j^{FF_{00}} \\ \mathbf{f}_j^{FF_{UU}} \end{bmatrix}, \quad \text{and} \quad \mathbf{F}^{NN} = \begin{bmatrix} \mathbf{f}_1^{NN_r} \\ \mathbf{f}_2^{NN_r} \\ \vdots \\ \mathbf{f}_1^{NN_d} \\ \mathbf{f}_2^{NN_d} \\ \vdots \end{bmatrix}.$$

Eqns. (2.27) - (2.29) represent the assembled system matrices and forcing vector for the global ROM. However, the system matrices are (in general) singular due to the transformation matrix used for PROM in Eq. (2.9). There, the constraint modes $\mathbf{\Psi}_i^0$ for the nominal parameter values (indicated by superscript 0) and the constraint modes $\mathbf{\Psi}_i^U$ for a perturbed parameter value can be linearly dependent. Thus, to numerically stabilize the system, the modal assurance criterion (MAC) for $\mathbf{\Psi}_i^0$ and $\mathbf{\Psi}_i^U$ is used when the i^{th} component PROM matrices are obtained. The MAC is given by

$$\mathbf{MAC}_i = \frac{\mathbf{\Psi}_i^{0T}\mathbf{\Psi}_i^U}{\sqrt{\mathbf{\Psi}_i^{0T}\mathbf{\Psi}_i^0}\sqrt{\mathbf{\Psi}_i^{UT}\mathbf{\Psi}_i^U}}, \quad \mathbf{e}_{jj}^i(\mathbf{MAC}_i) = \begin{cases} 0 & \text{MAC} \geq \epsilon \\ 1 & \text{MAC} < \epsilon \end{cases},$$

where subscript j in e_{jj} indicates the j^{th} static constraint mode, and ϵ is a constant close to 1 which is used to distinguish linearly dependent modes among all the static constraint modes. Note that only the counterpart modes for the perturbed parameter case need to be checked against those of the nominal parameter case. Here, $\mathbf{e}_{jj}^i$ is a vector used to decide whether to keep or to eliminate the static constraint mode j of the PROM substructure i. The entries of the eliminating vector consist only of 0 or 1. Using the eliminating vector $\mathbf{e}_{jj}^i$, the system matrices are reduced by eliminating DOFs which correspond to the perturbed parameter case.

Table 2.1: Thickness variations in substructures 1, 6 and 7

Substructure	Thickness, Case 1	Thickness, Case 2
1	0.4 mm $\rightarrow$ 0.473 mm	0.4 mm $\rightarrow$ 0.435 mm
6	0.4 mm $\rightarrow$ 0.422 mm	0.4 mm $\rightarrow$ 0.491 mm
7	0.4 mm $\rightarrow$ 0.493 mm	0.4 mm $\rightarrow$ 0.481 mm

2.3 Results for a Moderately Complex Structure: L-Shape Structure

To demonstrate the proposed MC-PROM, SMC-CMS and BFA methodologies, an L-shaped structure (shown in Fig. 2.3) with various parameter variations and dents has been investigated numerically. The left side of Fig. 2.3 is the pristine structure, and the right side of Fig. 2.3 shows the damaged structure. The forced response of the L-shape structure is computed, and resonant frequencies are identified. The structure consists of eight substructures. Substructures 1, 6 and 7 have thickness variations as shown by Case 1 and Case 2 in Tab. 2.1. Moreover, substructures 3 and 5 have geometric variations (dents). The CB-CMS method is applied for the remainder of the structure (the part of the structure which does not have any thickness or other geometric variations). Those are substructures 2, 4,

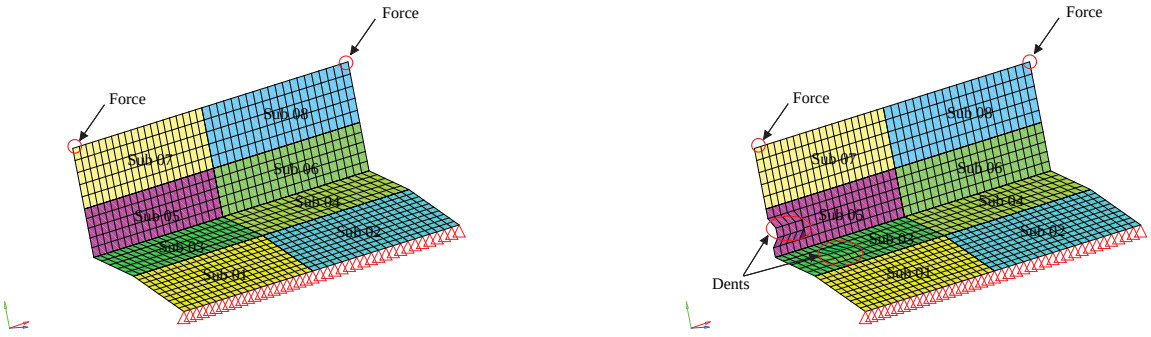

Figure 2.3: Healthy structure and damaged structure with thickness variations

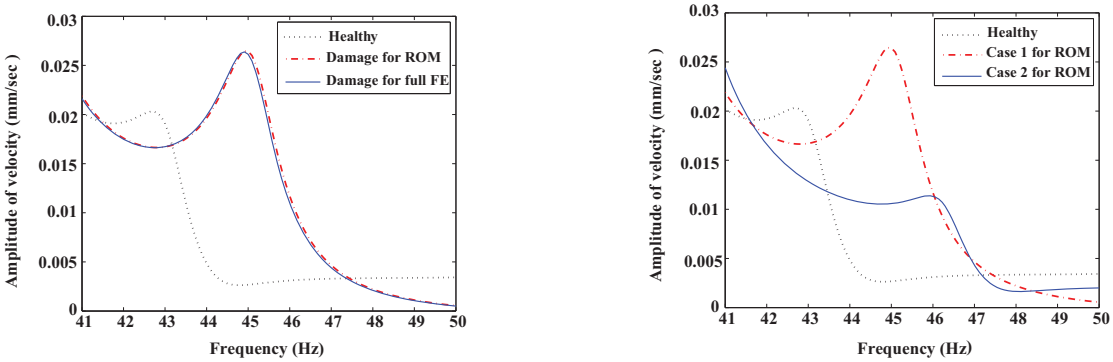

Figure 2.4: Forced response predictions provided by a full finite element model and a PROM for the healthy and damaged structures with thickness variations for Case 1 and Case 2

and 8. The remainder substructures are healthy and have nominal thickness of 0.4 mm. The MC-PROM and SMC-CMS methods are implemented for thickness and geometric variations respectively. Fig. 2.4 shows the system-level forced response for the healthy structure and the two cases of thickness variation. The response predicted by the PROM agrees well with the response proved by the full order model. On the left in Fig. 2.4, the dotted line represents the vibration response for the healthy structure, and the solid line is the response of the damaged structure with thickness variation (Case 1) and dents. Both these results are obtained using a full finite element model and response calculations performed using NASTRAN. Also, NASTRAN was used to obtain the finite element mass and stiffness matrices and force vectors. Using that information from NASTRAN, an in-house code was used to compute the structural vibration response.

The dashed line shows results obtained using a PROM based on CB-CMS, SMC-CMS, and MC-PROM. The results provided by the full model agree very well with those obtained using the novel PROM. In addition, on the right in Fig. 2.4, the dotted line is the response of the healthy structure, and the dashed line and the solid line are those for Case

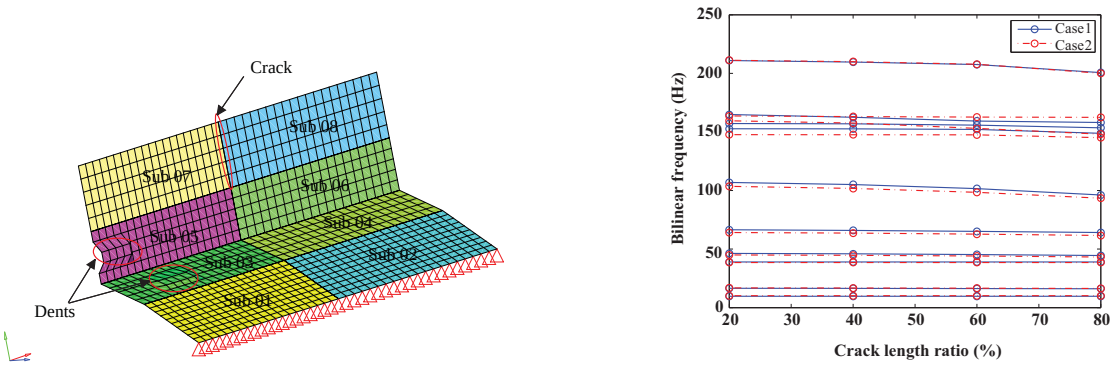

Figure 2.5: Cracked structure with geometric and thickness variations, and resonant frequencies predicted using BFA for the first 10 modes

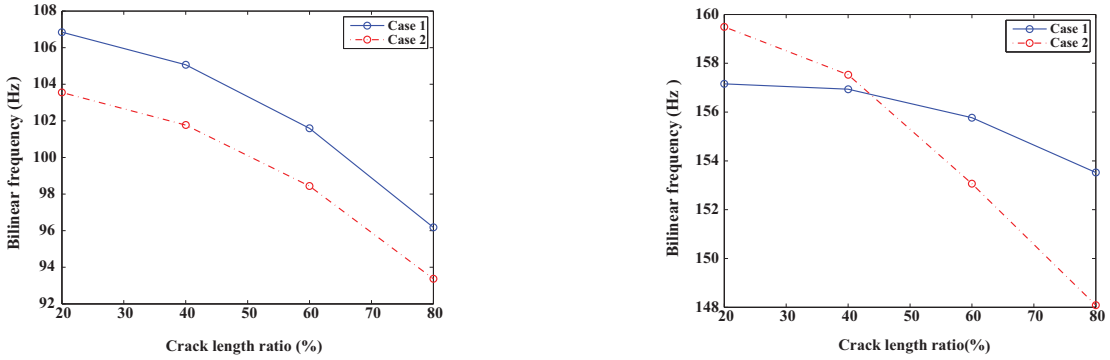

Figure 2.6: Shifts of resonant frequencies for cases 1 and 2 for the 6^{th} and 8^{th} modes

1 and Case 2, respectively. These results show that the example considered is a challenging one because even small structural variations in one component affect the system-level vibration response.

The left side of Fig. 2.5 shows the structure which has not only a dent and thickness variations as in Case 1 and Case 2, but also a crack between substructures 7 and 8. This structure has the same dents and thickness variations as in cases 1 and 2. The resonant frequencies of the first 10 modes are shown on the right in Fig. 2.5. The solid line and

the dashed line are the resonant frequencies for cases 1 and 2, respectively. The right side of Fig. 2.5 shows that the frequencies of the higher modes are shifted (compared to the healthy structure) more than frequencies of the lower modes. Fig. 2.6 shows the shift of the resonant frequency for the 6^{th} and 8^{th} modes respectively. The crack length varies from 20% to 80% (of structure's width). Note that the resonant frequencies are also shifted due to the thickness variations.

2.4 Results for a Complex Structure: HMMWV frame

In Sec. 2.3, the PROM method is applied to a moderately large model which consists of eight substructures. The total number of DOFs of the L-shape structure is not huge, so the analysis time using the full order and reduced-order models are not dramatically different. In this section, the PROM method is used to predict the dynamic response of a realistic vehicle model which is the base frame of a high mobility multipurpose wheeled vehicle (HMMWV). The finite element model for the HMMWV is a conventional model used to examine its dynamic response. Fig. 2.7 shows the finite element model of the HMMWV frame, and Fig. 2.8 shows each substructure of the HMMWV frame for constructing a PROM. The substructure which represents the reinforcement frame of the back and front left-rails have thickness variations, and the engine cradle has a dent. Tab. 2.3 shows two

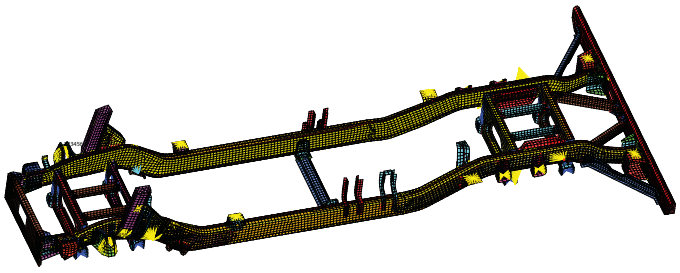

Figure 2.7: HMMWV frame FE model

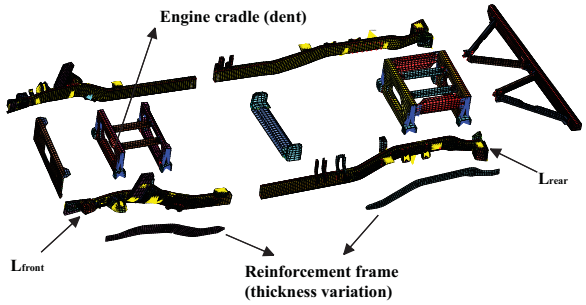

Figure 2.8: Substructuring for HMMWV frame

Table 2.2: Comparison of the full order model and the PROM

Types	Full Order Model	PROM
System DOFs	119,808	2,420
Initial Analysis Time	60,125 (sec.)	21,955 (sec.)
Reanalyses Time	60,125 (sec.)	595 (sec.)

cases of thickness variation of the reinforcement frames. The total number of DOFs of the HMMWV model is 119,808, and the calculation time for one full order analysis takes more than 6 hours. However, the PROM approach reduces the number of DOFs of the system and lowers the calculation time dramatically. Not only the time needed for the initial calculation is shortened, but also the time for subsequent analyses is drastically decreased. In Tab. 2.2, the number of DOFs and the computational time required for the initial analysis and for the reanalyses are shown. The number of DOFs of the PROM is much lower than that for the full order finite element model. Note that natural frequencies are needed for BFA. If natural frequencies are obtained from the full order finite element model which has 119,808 DOFs, the calculation time is much longer than that required by PROM because PROM requires fewer than 2000 DOFs. In addition, the initial analysis

Table 2.3: Thickness variations for the HMMWV frame in substructures L_{front} and L_{rear}

Substructure	Thickness, Case 1	Thickness, Case 2
L_{front}	3.0378 mm $\rightarrow$ 4.6268 mm	3.0378 mm $\rightarrow$ 5.5788 mm
L_{rear}	3.0378 mm $\rightarrow$ 5.3838 mm	3.0378 mm $\rightarrow$ 4.0908 mm

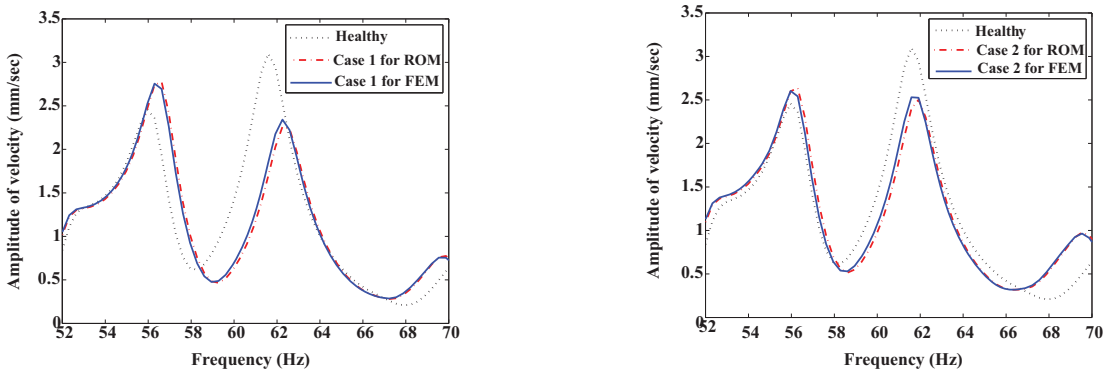

Figure 2.9: Forced response predictions provided by a full finite element model and a PROM for the healthy and damaged structures with thickness variations for cases 1 and 2 of the HMMWV frame

time needed for the PROM approach is 3 times shorter than that required by the full order finite element model. Also, the reanalysis time is 100 times faster than the time required by the full order finite element model. The time savings are not as large for the initial analysis as they are for reanalyses because of the need for an eigenanalysis to form the transformation matrix for each damage type.

Next, forces and moments are applied as excitations in several nodal points of the structure. Force and moments can be applied by the tires, the engine, and several other external factors such as the aerodynamics. Herein, forces and moments from the engine are considered. The Fig. 2.9 shows the response of the the HMMWV frame for cases 1 and 2 of thickness variation respectively. The dotted line shows the forced response of the

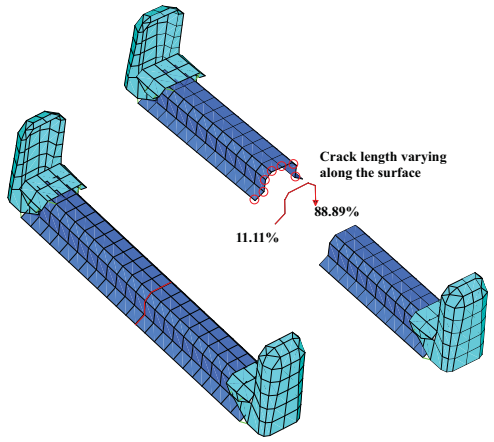

Figure 2.10: Cracked base frame component

healthy HMMWV structure, and the dashed line and the solid line show the response of the damaged HMMWV frame. Results obtained using a PROM and the full order model are shown.

Fig. 2.10 shows the finite element model of the cracked cross frame for the HMMWV frame. The crack length varies across the frame component from 11.11% to 88.89%. BFA is used to compute the resonant frequencies of the cracked HMMWV frame model. Note that the other damages (such as dents and thickness variations) are as in the cases 1 and 2. The resonant frequencies for cases 1 and 2 of thickness variation of the cracked and dented HMMWV frame model are shown in Fig. 2.11. These figures show the modes from the 1^{st} mode to the 5^{th} mode, the 11^{th} mode to the 15^{th} mode, and the 26^{th} mode to the 30^{th} mode, respectively. The lower frequencies shown in Fig. 2.11 do not shift much as the crack length increases. However, the mid-range resonant frequencies shift much more as the crack length increases, as shown in Fig. 2.11. Note that several modes switch when the crack length is around 40%. For the higher modes shown in Fig. 2.11, the frequencies shift more than those in lower modes, but the mode switching does not take place. Fig. 2.12

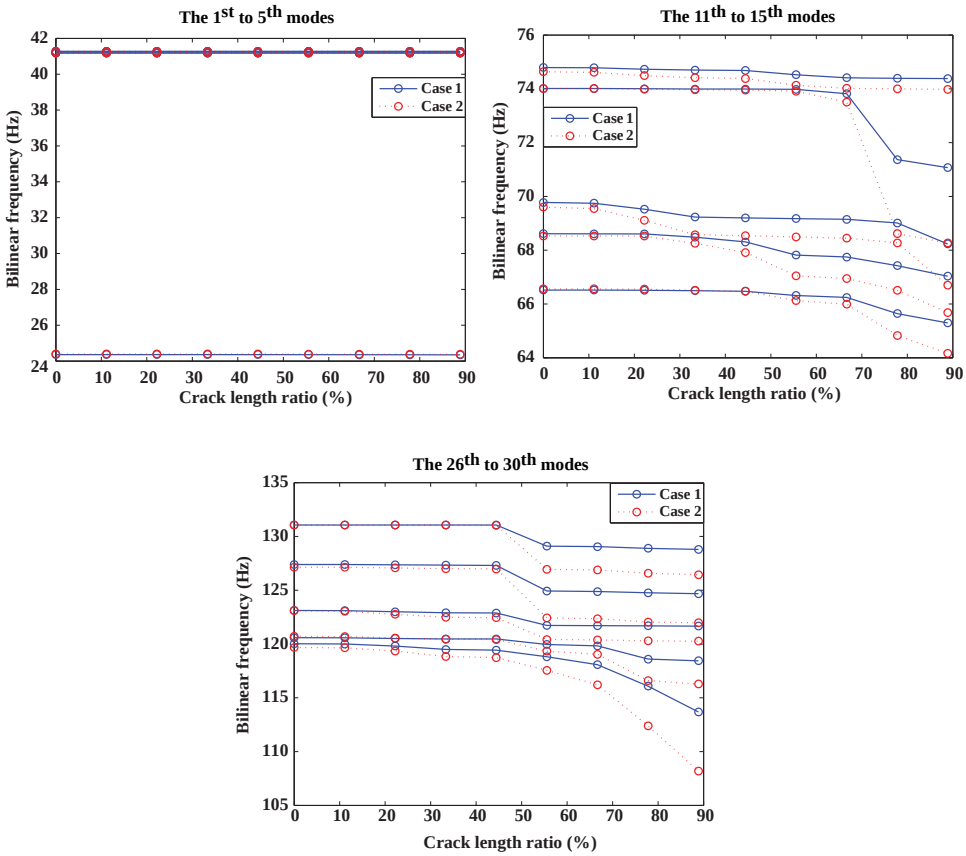

Figure 2.11: Resonant frequencies predicted using BFA for the first 5 modes, for the 11^{th} to 15^{th} mode, and for the 26^{th} to 30^{th} mode

shows the 14^{th} and 25^{th} resonant frequency of the cracked and dented HMMWV frame for cases 1 and 2 of thickness variations. These figures show that the resonant frequencies decrease significantly, once the crack length is larger than about 60%.

2.5 Conclusions and Discussion

Novel multiple-component parametric reduced-order models (MC-PROMs) for predicting the vibration response of complex structures have been developed. These models are able to handle simultaneously with very high efficiency both parametric variability in multiple components as well as damage. Also, the parametric reduced-order mod-

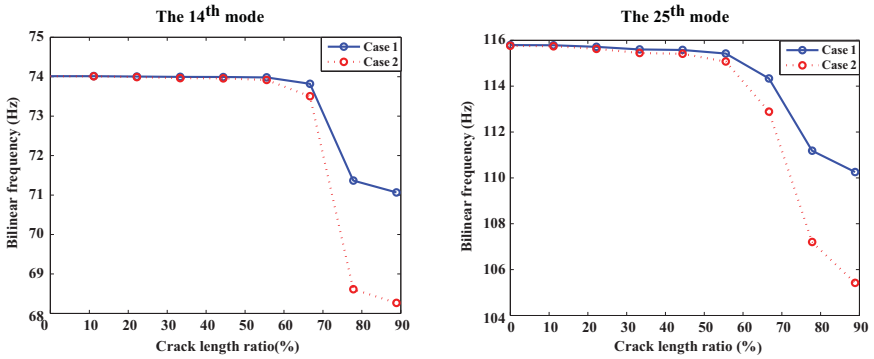

Figure 2.12: Resonant frequencies predicted using BFA for the 14^{th} mode and the 25^{th} mode

els (PROMs) developed are agile and easy to construct, which makes them particularly useful for analyses required in design processes.

In addition, the reanalysis time for parametric reduced-order models (PROM) is significantly shorter than that for the full order model. For example, to perform reanalyses which account for thickness variations (such as the ones in case 2 for the high mobility multipurpose wheeled vehicle (HMMWV) model) or new types of dents, the parametric reduced-order models (PROM) approach needs only a few simple matrix calculations (without the need for eigenanalyses) to construct the transformation matrix for each damage type. The appropriate transformation matrix to reduce the DOFs of the structure has been already constructed in the initial analysis. Hence, the recalculation of the transformation matrix is not needed. That is one of the core advantages of the parametric reduced order models (PROM) approach proposed herein.

The models developed are a viable, more efficient alternative to other component-mode-based parametric reduced-order models (PROMs). Although those models also require a reduced computation time compared to full finite element models, that computational time is still long. In particular, those models are hard to use for the analysis

of huge models. These issues can be overcome by the use multiple-component parametric reduced-order models (MC-PROMs) as described herein. The key characteristic of multiple-component parametric reduced-order models (MC-PROMs) is that parameterization is applied at the component-level rather than at the system-level. As a consequence, low order approximations of the variability in the mass and stiffness matrices is effective and accurate. Note that, in general, that is not the case for system-level matrices.

To manage the geometric variations created by dents, a methodology based on component mode synthesis with static mode compensation has been developed. Furthermore, to avoid the fully nonlinear analyses, a generalized bi-linear frequency approximation has been employed for predicting resonant frequencies of complex cracked structures. The predictions of full finite element models have been shown to agree very well with the predictions obtained using (dramatically lower-dimensional) reduced-order models.

The novel parametric reduced-order models (PROMs) approach provides smaller system matrices and shorter analysis and reanalysis time to predict the vibration response of complex structures. These advantages are particularly useful for optimization problems because parameter variations such as thickness variations, geometric deformations (dents), and interfaces (cracks) can easily be considered as design cases. Thus, the search for the optimal structure can be done effectively by using fast reanalyses based on parametric reduced-order models (PROMs). In contrast, conventional reduced-order modeling techniques cannot provide fast reanalyses because those reduced-order modeling are not constructed for that purpose. Instead, conventional reduced-order models reduce the size of the system matrices for *a single set of values* for the structural parameters and the geometry.

Model order reduction in general may use approximations which interfere with genuine changes in response caused by the damage. A key advantage of this work is that it

is designed to address precisely this issue. Specifically, the proposed approach focuses on accurately capturing the effects of small parameter variations on the overall system response. That contrasts other existing model order reduction techniques which often turn out to be robust to such variability.

CHAPTER III

Next-Generation Parametric Reduced-Order Models

3.1 Introduction

Generally, most research related to structural dynamic analysis are in need of save computational cost saving because of the repetitive nature of optimization, stochastic, and statistical analyses. Even considering computing power increases, these repetitive processes are very time consuming due to the conventional complex and large model. One method to save computational time is the use of reduced-order models (ROMs). There are a significant number of existing research studies about ROMs. Yun and Masri [1, 2] developed a methodology for stochastic detection of changes in uncertain nonlinear systems using ROMs. Chung and Fung [3] proposed a nonlinear finite element model of piezoelectric tube actuators with hysteresis and creep for control and design purposes. In their work, the operation of the actuators is simulated using ROMs. Ashwin *et al.* [4] developed a finite element based substructuring procedure for design analysis of large structural systems. Hartl *et al.* [5] also developed advanced methods for analysis, design, and optimization which use ROMs for computational efficiency.

In the field of structural dynamics, component mode synthesis (CMS) techniques [6–12] are well established as an alternative to conventional finite element models (FEMs) with large numbers of degrees of freedom (DOFs). CMS belongs to a wide class of do-

main decomposition techniques. CMS is a substructural based technique, which divides the global structure into several substructures. The DOFs of those substructures can be reduced significantly. Then, each individual substructure in the CMS domain is reconnected, and the system dynamic responses are predicted very efficiently and accurately. Applications of CMS include the work of Wang and Kirkhope [13] who applied CMS for multi-shaft rotors with flexible inter-shaft bearings. They also developed CMS for damped systems [14]. In addition, Liu and Zheng [15] proposed the improved component mode synthesis for nonclassically damped systems. Takewaki [16] proposed the inverse component mode synthesis method for redesign of large structural systems. Matichard and Gaudiller [17] developed the hybrid modal nodal method for multi-body smart structure model reduction and feedback control development by CMS. Kim [18] also developed a recursive component mode synthesis method to solve large-scale eigenvalue problems efficiently. Tran [19] developed and applied component mode synthesis using partial interface modes to a cyclically symmetric structure. To enhance computational efficiency for redesign of damped large structural systems, Takewaki and Uetani [20] used a new formulation for an incremental inverse problem based on component mode synthesis. Elhami *et al.* [21] proposed methods for repetitive symmetric structures using CMS. Farhat and Geradin [22] developed a methodology for applying CMS to structures with incompatible substructures.

In general, CMS has become a very popular numerical tool in aerospace and automotive engineering because it usually meets high standards of computational efficiency. Computational efficiency is illustrated by significant cost saving when remeshing is needed, since this task can be done locally, i.e. on each substructure separately. However, the remeshing process might also be time consuming computationally and manually for design purposes such as structural optimization, and for damage modeling for structural health

monitoring. Therefore, ROMs for design and damage modeling purposes are needed.

The ROMs for design and damage modeling were introduced almost fifteen years ago by Balmés *et al.* [28,29] to avoid the relatively expensive process of reanalysis of complex structures. In addition, several other ROMs referred to as parametric reduced-order models (PROMs) have been developed [30–32, 35]. In particular, multi-component PROMs (MC-PROMs) have been developed recently by Hong *et al.* [35]. For robust substructure (re)analysis, MC-PROMs are advantageous because they allow several substructures to have parametric variability in characteristics such as geometric parameters (e.g., thickness), or material properties (e.g., Young's modulus). MC-PROMs are perfectly suited for predicting the vibration response of structures modeled with shell-type finite elements which can have thickness variations. However, if the structure is modeled with brick-type finite elements, and if the brick-type elements require local volume changes during reanalysis, then MC-PROMs cannot be effectively used to predict the dynamic response. This is because MC-PROMs use third-order Taylor series for parameterization. These Taylor series do not capture accurately the variation of the mass and stiffness matrices for brick-type finite elements because the volume of local finite elements can change during the reanalysis. Consequently, some entries of the mass and stiffness matrices for brick-type finite elements vary highly nonlinearly with respect to geometric variations in the structure. Herein, a novel parameterization technique is proposed to capture these element-level nonlinearities.

Another challenge for MC-PROMs is that they can be numerically not stable due to the transformation matrix they employ. Specifically, the transformation matrix consists of static constraint modes and fixed interface normal modes computed for a set of nominal parameters, and a few sets of perturbed parameter values (typically up to 3 sets per parameter) [35]. If all static constraint modes are kept and many normal modes are included,

then the size of the system-level mass and stiffness matrices can be nearly singular (and can even be larger than that of the full-order models). This is because the transformation matrix can contain vectors which are nearly linearly dependent. These vectors are usually normal modes for substructures where the parametric variation (e.g., modulus of elasticity) does not affect the component-level normal modes. Moreover, the transformation matrix used in MC-PROMs was designed for small parameter variations which ensures that the space spanned by the basis vectors at a component-level does not depend nonlinearly on parameter variations. That approach can break down because of the volume variations which can occur when brick elements are used.

Another challenge of CMS methods and MC-PROMs is that they often require an excessively large number of interface DOFs because (often) these DOFs are many and are hard (or impossible) to reduce. To address this issue, Castanier *et al.* [11] proposed that the physical interface DOFs be replaced by global interface modes, which were also called characteristic constraint (CC) modes. However, this concept is not optimal for substructural-based techniques because CC modes are $system$-level interface modes, not $substructural$-level interface modes. Thus, a new technique to reduce the interface DOFs locally is proposed herein and referred to as local-interface reduction.

This paper is organized as follows. In Sec. 3.2, the element-level nonlinearity due to the volume variations of finite elements of brick or other type is evaluated, and a novel parameterization technique is proposed to capture this nonlinearity. Next, in Sec. 3.3, CMS is briefly reviewed, and next-generation parametric reduced-order models (NX-PROMs) are proposed. In Sec. 3.4, to locally reduce the interface DOFs, a local-interface reduction technique is presented. Section 3.5 discusses the procedure to assemble substructural mass and stiffness matrices (with and without implementing the local-interface reduction technique). In Sec. 3.6, numerical examples such as a plate structure, an L-shaped structure,

and a realistic vehicle model (a high mobility multipurpose wheeled vehicle, HMMWV) modeled with brick-type finite elements are used to demonstrate the proposed methods. Finally, conclusions are summarized in Sec. 3.7.

3.2 Robust Parameterization Techniques for Element-Level Nonlinearity

For structural design and damage modeling purposes, the parameterization of the mass and stiffness matrices can be the most important step. This is because the parameterization techniques enable capturing mass and stiffness variations due to design changes or damage in the structure. Thus, the reanalysis time can be significantly reduced because the finite element mesh does not need to be modified and remodeled. The parameterization technique has to be adapted for the different characteristics of each type of finite element used. For example, the thickness, Young's modulus, and material density variations of shell-type elements can be captured well by third-order Taylor series [28, 29, 32, 35]. However, we found that the thickness variations for a brick and other types of finite elements such as hexagonal and tetrahedron elements cannot be captured well by Taylor series of low order due to an element-level nonlinear characteristics caused by volume variations. For elements which have volume, local thickness variations induce volume variations in the elements. In contrast, Taylor series works well for parameterizing shell-type elements because these do not have actual volume. In this section, a parameterization technique that captures thickness variations of brick and other types of finite elements is the focus.

Fig. 3.1 shows an 8-node brick-type element which uses first-order (linear) shape functions. Coordinates x, y, and z are global, and coordinates ξ, η, and ζ are local. As a conceptual example, consider that the four nodes on the top surface in Fig. 3.1 move by a distance Δt. The brick-type element has a volume, so when each node moves, the volume

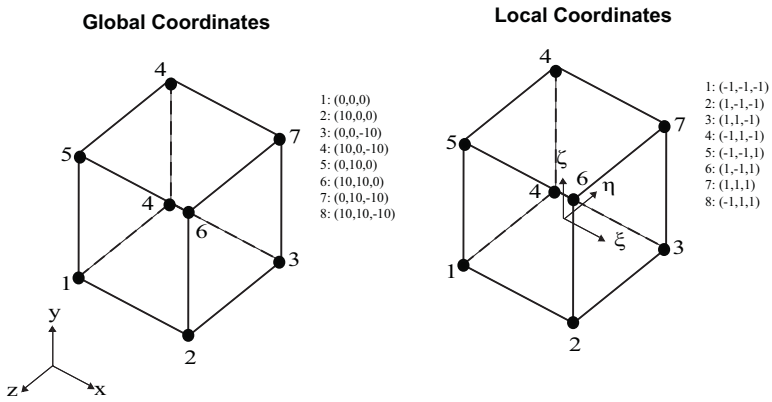

Figure 3.1: Sample 8-node brick element with global and local coordinates

of the brick-type element varies. Thus, the parameterization technique has to account for these volume variations. To that aim, let us first revisit the formulation used to derive stiffness matrices for brick-type elements [62, 63]. The equation used to obtain the stiffness matrix can be expressed as

$$\begin{aligned}\mathbf{K} &= \int_V \mathbf{B}^T\mathbf{D}\mathbf{B}\mathrm{d}V \\ &= \int_{\zeta=-1}^{\zeta=1}\int_{\eta=-1}^{\eta=1}\int_{\xi=-1}^{\xi=1} \mathbf{B}^T\mathbf{D}\mathbf{B}\mathrm{d}\xi\mathrm{d}\eta\mathrm{d}\zeta \\ &= \sum_{i=1}^{8}\sum_{j=1}^{8}\sum_{k=1}^{8} W_iW_jW_k\mathbf{B}^T(\xi_i,\eta_j,\zeta_k)\mathbf{D}\mathbf{B}(\xi_i,\eta_j,\zeta_k)\det(\mathbf{J}(\xi_i,\eta_j,\zeta_k)),\end{aligned} \tag{3.1}$$

where $\mathbf{B}$ is a strain matrix (which contains derivatives of the linear shape functions in global coordinates), and $\mathbf{D}$ is an elasticity matrix (which contains Poisson's ratio ν, and the elastic modulus E). The determinant of the Jacobian in Eq. (3.1) is obtained from the coordinate transformation of the strain matrix $\mathbf{B}$. The determinant contains in its denominator a cubic polynomial of ξ, η and ζ, which reflects volume variations. Thus, the parameterization should also contain a cubic polynomial in the denominator. To establish the coefficients of this cubic polynomial, the volume variations of brick-type elements are considered. As shown in Fig. 3.1, one or several nodes on the top surface move to capture

thickness variations. The resulting volume can be expressed as

$$V = V_0 \left[1 + d\frac{p - p_0}{p_0}\right] = V_0 \left(1 + d\frac{\Delta p}{p_0}\right),$$

where V and V_0 are the final and the initial volume of the brick-type element, and p and p_0 are the target parameter value (thickness) and the initial parameter value. When only one node on the top surface moves, the coefficient d is 1/3. Similarly, when two nodes move, $d = 1/2$. Also, when three nodes move, $d = 1$. Finally, when four nodes move, the volume variation is proportional to Δp, i.e. $V = V_0 \frac{\Delta p}{p}$. This last type of variation, proportional to Δp, is very well captured by a regular interpolation. The other three cases, however, are not. To address this issue, a cubic polynomial which considers the volume variation of brick-type elements with a target parameter variation Δp is defined as

$$D(\Delta p) = \left(1 + \frac{\Delta p}{p_0}\right)\left(1 + \frac{1}{2}\frac{\Delta p}{p_0}\right)\left(1 + \frac{1}{3}\frac{\Delta p}{p_0}\right). \tag{3.2}$$

The new parameterization equation consists of a fourth-order interpolation in the numerator and the cubic polynomial in Eq. (3.2) in the denominator, which yields the new parameterization as

$$\mathbf{K}(p_0 + \Delta p) \approx \frac{\mathbf{K}_0 + \mathbf{K}_1 \Delta p + \mathbf{K}_2 (\Delta p)^2 + \mathbf{K}_3 (\Delta p)^3 + \mathbf{K}_4 (\Delta p)^4}{D(\Delta p)}. \tag{3.3}$$

To calculate the matrices $\mathbf{K}_0$, $\mathbf{K}_1$, $\mathbf{K}_2$, $\mathbf{K}_3$ and $\mathbf{K}_4$ in Eq. (3.3), five equations are needed. For that, stiffness matrices for five parameter values are computed. First, consider the case where $\Delta p = 0$. One obtains

$$\mathbf{K}(p_0) \approx \mathbf{K}_0. \tag{3.4}$$

Next, consider $\Delta p = i\delta p$ (with $i = 1, 2, 3, 4$), one obtains

$$\mathbf{K}(p_0 + i\delta p) \approx \frac{\mathbf{K}_0 + \mathbf{K}_1 (i\delta p) + \mathbf{K}_2 (i\delta p)^2 + \mathbf{K}_3 (i\delta p)^3 + \mathbf{K}_4 (i\delta p)^4}{D(\delta p)}. \tag{3.5}$$

Rearranging Eqs. (3.4) and (3.5) into matrix form, for each entry e,q of the matrices $\mathbf{K}_1$, $\mathbf{K}_2$, $\mathbf{K}_3$ and $\mathbf{K}_4$, one obtains

$$\mathbf{C}\begin{bmatrix}\mathbf{K}_{0,eq}\\ \mathbf{K}_{1,eq}\\ \mathbf{K}_{2,eq}\\ \mathbf{K}_{3,eq}\\ \mathbf{K}_{4,eq}\end{bmatrix}=\begin{bmatrix}\mathbf{K}(p_0)_{eq}\\ \mathbf{K}(p_0+\delta p)_{eq}\\ \mathbf{K}(p_0+2\delta p)_{eq}\\ \mathbf{K}(p_0+3\delta p)_{eq}\\ \mathbf{K}(p_0+4\delta p)_{eq}\end{bmatrix}, \tag{3.6}$$

where

$$\mathbf{C}=\begin{bmatrix}1 & 0 & 0 & 0 & 0\\ \frac{1}{D(\delta p)} & \frac{\delta p}{D(\delta p)} & \frac{(\delta p)^2}{D(\delta p)} & \frac{(\delta p)^3}{D(\delta p)} & \frac{(\delta p)^4}{D(\delta p)}\\ \frac{1}{D(2\delta p)} & \frac{(2\delta p)}{D(2\delta p)} & \frac{(2\delta p)^2}{D(2\delta p)} & \frac{(2\delta p)^3}{D(2\delta p)} & \frac{(2\delta p)^4}{D(2\delta p)}\\ \frac{1}{D(3\delta p)} & \frac{(3\delta p)}{D(3\delta p)} & \frac{(3\delta p)^2}{D(3\delta p)} & \frac{(3\delta p)^3}{D(3\delta p)} & \frac{(3\delta p)^4}{D(3\delta p)}\\ \frac{1}{D(4\delta p)} & \frac{(4\delta p)}{D(4\delta p)} & \frac{(4\delta p)^2}{D(4\delta p)} & \frac{(4\delta p)^3}{D(4\delta p)} & \frac{(4\delta p)^4}{D(4\delta p)}\end{bmatrix}.$$

Equation (3.6) can be easily solved by simply inverting the 5×5 matrix on the left hand side. This matrix is non-singular and very well behaved for inversion. Also, note that this

inversion has to be done only once (for a given δp). Let us denote by $\mathbf{A}$ this inverse matrix,

$$\mathbf{A} = \begin{bmatrix} 1 & 0 & 0 & 0 & 0 \\ \frac{1}{D(\delta p)} & \frac{\delta p}{D(\delta p)} & \frac{(\delta p)^2}{D(\delta p)} & \frac{(\delta p)^3}{D(\delta p)} & \frac{(\delta p)^4}{D(\delta p)} \\ \frac{1}{D(2\delta p)} & \frac{(2\delta p)}{D(2\delta p)} & \frac{(2\delta p)^2}{D(2\delta p)} & \frac{(2\delta p)^3}{D(2\delta p)} & \frac{(2\delta p)^4}{D(2\delta p)} \\ \frac{1}{D(3\delta p)} & \frac{(3\delta p)}{D(3\delta p)} & \frac{(3\delta p)^2}{D(3\delta p)} & \frac{(3\delta p)^3}{D(3\delta p)} & \frac{(3\delta p)^4}{D(3\delta p)} \\ \frac{1}{D(4\delta p)} & \frac{(4\delta p)}{D(4\delta p)} & \frac{(4\delta p)^2}{D(4\delta p)} & \frac{(4\delta p)^3}{D(4\delta p)} & \frac{(4\delta p)^4}{D(4\delta p)} \end{bmatrix}^{-1}$$

$$= \begin{bmatrix} A_{11} & A_{12} & A_{13} & A_{14} & A_{15} \\ A_{21} & A_{22} & A_{23} & A_{24} & A_{25} \\ A_{31} & A_{32} & A_{33} & A_{34} & A_{35} \\ A_{41} & A_{42} & A_{43} & A_{44} & A_{45} \\ A_{51} & A_{52} & A_{53} & A_{54} & A_{55} \end{bmatrix}.$$

Re-arranging Eq. (3.6) using the entries in $\mathbf{A}$, one obtains

$$\begin{aligned} \mathbf{K}(p_0 + \Delta p) &\approx b_0\mathbf{K}(p_0) + b_1\mathbf{K}(p_0 + \delta p) + b_2\mathbf{K}(p_0 + 2\delta p) \\ &+ b_3\mathbf{K}(p_0 + 3\delta p) + b_4\mathbf{K}(p_0 + 4\delta p), \end{aligned} \tag{3.7}$$

where

$$\begin{aligned} b_0 &= (A_{11} + A_{21}\Delta p + A_{31}\Delta p^2 + A_{41}\Delta p^3 + A_{51}\Delta p^4), \\ b_1 &= (A_{12} + A_{22}\Delta p + A_{32}\Delta p^2 + A_{42}\Delta p^3 + A_{52}\Delta p^4), \\ b_2 &= (A_{13} + A_{23}\Delta p + A_{33}\Delta p^2 + A_{43}\Delta p^3 + A_{53}\Delta p^4), \\ b_3 &= (A_{14} + A_{24}\Delta p + A_{34}\Delta p^2 + A_{44}\Delta p^3 + A_{54}\Delta p^4), \\ b_4 &= (A_{15} + A_{25}\Delta p + A_{35}\Delta p^2 + A_{45}\Delta p^3 + A_{55}\Delta p^4). \end{aligned}$$

Equation (3.7) shows that $\mathbf{K}(p_0+\Delta p)$ is simply a linear combination of five (pre-computed) matrices. The coefficients in the linear combination depend very nonlinearly on Δp. That

is the key factor which ensures the high accuracy of the new parameterization. Note that the computational cost of the new parameterization is the same as that for a regular fourth-order interpolation. The accuracy, however, is higher (as shown on Sec. 3.6.1).

3.3 Reduced-Order Models

The parameterization techniques proposed in Sec. 3.2 are for the full-order finite element model. However, the main objective of this work is to predict vibration responses using ROMs (as opposed to full-order models) to reduce the calculation time. To detail the construction of ROMs, the fixed-interface Craig-Bampton component mode synthesis (CB-CMS) [10] is reviewed briefly. Next, a new transformation matrix is presented and used in conjunction with the new parameterization technique discussed in Sec. 3.2. Finally, NX-PROMs are constructed.

3.3.1 Brief review of Craig-Bampton component mode synthesis

In this section, the fixed-interface CB-CMS [7] method is reviewed. This modeling approach is broadly used because of its simplicity and computational stability. To apply the CB-CMS, the complex structure of interest is partitioned into substructures. The DOFs of each substructure are further partitioned into active DOFs on the interface (indicated by the superscript A), and omitted DOFs in the interior (indicated by the superscript O). The mass and stiffness matrices for a component i can then be partitioned to obtain

$$\mathbf{M}_i = \begin{bmatrix} \mathbf{m}_i^{AA} & \mathbf{m}_i^{AO} \\ \mathbf{m}_i^{OA} & \mathbf{m}_i^{OO} \end{bmatrix}, \quad \text{and} \quad \mathbf{K}_i = \begin{bmatrix} \mathbf{k}_i^{AA} & \mathbf{k}_i^{AO} \\ \mathbf{k}_i^{OA} & \mathbf{k}_i^{OO} \end{bmatrix}.$$

Next, the physical coordinates are changed to a set of coordinates representing the amplitudes of a selected set of fixed-interface component-level normal modes $\mathbf{\Phi}_i^N$ (indicated by the superscript N), and the amplitudes of the full set of static constraint modes

$\mathbf{\Phi}_i^C = -\mathbf{k}_i^{OO^{-1}}\mathbf{k}_i^{OA}$ (indicated by the superscript C). The transformed mass and stiffness matrices for component i can be expressed as

$$\mathbf{M}_i^{CBCMS} = \begin{bmatrix} \hat{\mathbf{m}}_i^C & \hat{\mathbf{m}}_i^{CN} \\ \hat{\mathbf{m}}_i^{NC} & \hat{\mathbf{m}}_i^N \end{bmatrix}, \quad \text{and} \quad \mathbf{K}_i^{CBCMS} = \begin{bmatrix} \hat{\mathbf{k}}_i^C & \hat{\mathbf{k}}_i^{CN} \\ \hat{\mathbf{k}}_i^{NC} & \hat{\mathbf{k}}_i^N \end{bmatrix}.$$

In this work, the CB-CMS method is used $only$ for the substructures which do not have any parameter variation or damage.

3.3.2 Next-generation parametric reduced-order models

In this section, MC-PROMs are improved to be more robust and mathematically stable. The resulting models are referred to as NX-PROMs.

Transformation matrix for NX-PROMs

The transformation matrix for NX-PROMs is constructed somewhat similar to MC-PROMs (which was constructed by using the idea behind CB-CMS). It also has a set of static constraint modes $\mathbf{\Psi}^C$ and a set of fixed-interface normal modes $\mathbf{\Phi}^N$. However, the transformation matrix for NX-PROMs has a different set of static constraint modes and a different set of fixed-interface normal modes compared at CB-CMS and MC-PROM. This transformation matrix can be written for component i as

$$\mathbf{T}_i = \begin{bmatrix} \mathbf{I} & \mathbf{0} \\ \mathbf{\Psi}_{\text{aug},i}^C & \mathbf{\Phi}_{\text{aug},i}^N \end{bmatrix},$$

where $\mathbf{\Psi}_{\text{aug}}^C$ is referred to as the matrix of augmented constraint modes

$$\mathbf{\Psi}_{\text{aug},i}^C = \begin{bmatrix} \mathbf{\Psi}_{0,i}^C & \mathbf{\Psi}_{1,i}^C & \mathbf{\Psi}_{2,i}^C & \mathbf{\Psi}_{3,i}^C & \mathbf{\Psi}_{4,i}^C \end{bmatrix},$$

and $\mathbf{\Phi}_{\text{aug}}^N$ is referred to as the matrix of augmented fixed-interface normal modes

$$\mathbf{\Phi}_{\text{aug},i}^N = \begin{bmatrix} \mathbf{\Phi}_{0,i}^N & \mathbf{\Phi}_{1,i}^N & \mathbf{\Phi}_{2,i}^N & \mathbf{\Phi}_{3,i}^N & \mathbf{\Phi}_{4,i}^N \end{bmatrix}.$$

Matrices $\mathbf{\Psi}^C_{0,i}$ and $\mathbf{\Phi}^N_{0,i}$ correspond to the nominal parameter values, whereas matrices $\mathbf{\Psi}^C_{l,i}$ and $\mathbf{\Phi}^N_{l,i}$ $(l = 1, 2, 3, 4)$ correspond to four other parameter values.

In general, the columns of $\mathbf{\Phi}^N_{\text{aug}}$ are not orthogonal. Therefore, for numerical stability, an orthogonal basis for the space spanned by these modes is computed. This basis is obtained by a truncated set of left singular vectors $\mathbf{U}^N$ of $\mathbf{\Phi}^N_{\text{aug}}$ [35]. Thus, the new transformation matrix can be expressed as

$$\tilde{\mathbf{T}}_i = \begin{bmatrix} \mathbf{I} & \mathbf{0} \\ \mathbf{\Psi}^C_{\text{aug},i} & \mathbf{U}^N_i \end{bmatrix}. \tag{3.8}$$

The transformation matrix in Eq. (3.8) can be used to project the physical domain onto the NX-PROM domain. The stiffness matrix $\mathbf{K}^{NXPROM}_i = \tilde{\mathbf{T}}^{\mathrm{T}}_i \mathbf{K}^{FEM}_i \tilde{\mathbf{T}}_i$ for component i (where $\mathbf{K}^{FEM}_i$ represents the stiffness matrix of the full-order model of component i) can be partitioned to obtain

$$\mathbf{K}^{NXPROM}_i = \begin{bmatrix} \mathbf{K}^C_{00,i} & \mathbf{K}^C_{01,i} & \mathbf{K}^C_{02,i} & \mathbf{K}^C_{03,i} & \mathbf{K}^C_{04,i} & \mathbf{K}^{CN}_{00,i} \\ \mathbf{K}^C_{10,i} & \mathbf{K}^C_{11,i} & \mathbf{K}^C_{12,i} & \mathbf{K}^C_{13,i} & \mathbf{K}^C_{14,i} & \mathbf{K}^{CN}_{11,i} \\ \mathbf{K}^C_{20,i} & \mathbf{K}^C_{21,i} & \mathbf{K}^C_{22,i} & \mathbf{K}^C_{23,i} & \mathbf{K}^C_{24,i} & \mathbf{K}^{CN}_{22,i} \\ \mathbf{K}^C_{30,i} & \mathbf{K}^C_{31,i} & \mathbf{K}^C_{32,i} & \mathbf{K}^C_{33,i} & \mathbf{K}^C_{34,i} & \mathbf{K}^{CN}_{33,i} \\ \mathbf{K}^C_{40,i} & \mathbf{K}^C_{41,i} & \mathbf{K}^C_{42,i} & \mathbf{K}^C_{43,i} & \mathbf{K}^C_{44,i} & \mathbf{K}^{CN}_{44,i} \\ \mathbf{K}^{NC}_{00,i} & \mathbf{K}^{NC}_{11,i} & \mathbf{K}^{NC}_{22,i} & \mathbf{K}^{NC}_{33,i} & \mathbf{K}^{NC}_{44,i} & \mathbf{K}^N_i \end{bmatrix}.$$

A similar relation is obtained for the mass matrix of component i. Here, the DOFs corresponding to the constraint part (superscript C) are repeated for the five parameter values (denoted by subscript 0, 1, 2, 3 and 4). Note that in such an approach, the size of the mass and stiffness matrices can be quite large. Also, these matrices may be ill-conditioned because the columns of $\mathbf{\Psi}^C_{\text{aug},i}$ are not necessarily linearly independent.

To address this issue, a new method to account for the static constraint modes is developed. This new method avoids duplicating the interface DOFs (C) and captures the

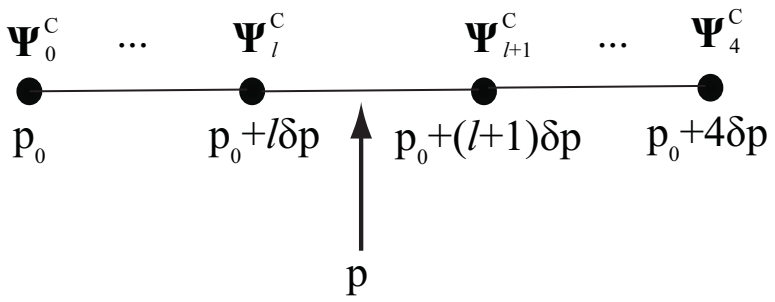

Figure 3.2: The case where the value of parameter p is between p_0+$l\delta p$ and p_0+$(l+1)\delta p$ for some l value between 0 and 3

interface effects more accurately. The approach reduces the number of sets of static constraint modes (used to obtain $\mathbf{M}_i^{NXPROM}$ and $\mathbf{K}_i^{NXPROM}$) from five sets to just one set. Consider that the actual value p of the parameter where the reanalysis is needed exists between the l^{th} and $(l+1)^{\text{th}}$ parameter values ($l = 0, 1, 2, 3$ or 4) which were used to construct $\mathbf{M}_i^{NXPROM}$. In that case (described in Fig. 3.2), a new static constraint mode can be generated by linearly interpolating between the static constraint modes for the l^{th} and the $(l+1)^{\text{th}}$ parameter values to obtain

$$\tilde{\mathbf{\Psi}}_i^C = \left(\frac{p_{l+1} - p}{p_{l+1} - p_l}\right) \mathbf{\Psi}_{l,i}^C + \left(\frac{p - p_l}{p_{l+1} - p_l}\right) \mathbf{\Psi}_{l+1,i}^C = \alpha_i \mathbf{\Psi}_{l,i}^C + \beta_i \mathbf{\Psi}_{l+1,i}^C. \tag{3.9}$$

This new static constraint mode $\tilde{\mathbf{\Psi}}_i^C$ replaces all five static constraint modes used to construct $\tilde{\mathbf{T}}_i$ in Eq. (3.8).

Note that this reduction can be implemented without re-constructing $\tilde{\mathbf{T}}_i$ for each case of parameter variation. Instead, only simple linear combinations of partitions of the matrices $\mathbf{M}_i^{NXPROM}$ and $\mathbf{K}_i^{NXPROM}$, are needed. Details are given in below section. In the end, the final NX-PROM mass and stiffness matrices have only a single set of constraint modes $\tilde{\mathbf{\Psi}}_i^C$ which always has linearly independent columns.

Parameterization for NX-PROMs

The new interpolation presented in Sec. 3.2 is applied to NX-PROMs. To that aim, five mass and five stiffness are constructed for each component i (for $l = 0, 1, 2, 3, 4$) as follows

$$\mathbf{M}_{l,i}^{NX} = \tilde{\mathbf{T}}_i^{\mathrm{T}} \mathbf{M}(p_0 + l\delta p)\tilde{\mathbf{T}}_i \quad \text{and} \quad \mathbf{K}_{l,i}^{NX} = \tilde{\mathbf{T}}_i^{\mathrm{T}} \mathbf{K}(p_0 + l\delta p)\tilde{\mathbf{T}}_i.$$

These matrices are not all used independently to form NX-PROMs. Instead, they are linearly combined to implement the single set of static constraint modes $\tilde{\mathbf{\Psi}}_i^C$ in Eq. (3.9). Thus, conceptually, $\tilde{\mathbf{T}}_i$ is replaced by $\hat{\mathbf{T}}_i$, given by

$$\hat{\mathbf{T}}_i = \begin{bmatrix} \mathbf{I} & \mathbf{0} \\ \mathbf{\Psi}_{\mathrm{aug},i}^C & \mathbf{U}_i^N \end{bmatrix} (\alpha_i \mathbf{R}_{l,i} + \beta_i \mathbf{R}_{l+1,i}) = \tilde{\mathbf{T}} \left(\alpha_i \mathbf{R}_{l,i} + \beta_i \mathbf{R}_{l+1,i}\right),$$

where $\mathbf{R}_{l,i}$ and $\mathbf{R}_{l+1,i}$ are masking matrices of zeros and ones. The matrix $\mathbf{R}_{l,i}$ is a 6×2 block matrix where the blocks $(l, 1)$ and $(6, 2)$ are unit matrices, while all other blocks are zero. The first five rows correspond to $\mathbf{\Psi}_{l,i}^C$ ($l = 0, 1, 2, 3, 4$) and the last row corresponds to $\mathbf{U}_i^N$. This new transformation matrix $\hat{\mathbf{T}}_i$ is applied to the mass and stiffness matrices of component i to construct NX-PROMs. First, five mass and stiffness matrices are constructed for each parameter variation $s\delta p$ (for $s = 0, 1, 2, 3, 4$) as follows

$$\begin{aligned} \hat{\mathbf{M}}_{s,i}^{NX} &= \left(\alpha_i \mathbf{R}_{l,i}^{\mathrm{T}} + \beta_i \mathbf{R}_{l+1,i}^{\mathrm{T}}\right) \mathbf{M}_{s,i}^{NX} \left(\alpha_i \mathbf{R}_{l,i} + \beta_i \mathbf{R}_{l+1,i}\right), \\ \hat{\mathbf{K}}_{s,i}^{NX} &= \left(\alpha_i \mathbf{R}_{l,i}^{\mathrm{T}} + \beta_i \mathbf{R}_{l+1,i}^{\mathrm{T}}\right) \mathbf{K}_{s,i}^{NX} \left(\alpha_i \mathbf{R}_{l,i} + \beta_i \mathbf{R}_{l+1,i}\right). \end{aligned}$$

Next, the new interpolation discussed in Sec. 3.2 is applied using $\hat{\mathbf{M}}_{s,i}^{NX}$ and $\hat{\mathbf{K}}_{s,i}^{NX}$. Eq. (3.7) is used to obtain

$$\begin{aligned} \mathbf{M}(p_0 + \Delta p)_i^{NX} &\approx b_0 \hat{\mathbf{M}}_{0,i}^{NX} + b_1 \hat{\mathbf{M}}_{1,i}^{NX} + b_2 \mathbf{M}_{2,i}^{NX} + b_3 \hat{\mathbf{M}}_{3,i}^{NX} + b_4 \hat{\mathbf{M}}_{4,i}^{NX} \\ \mathbf{K}(p_0 + \Delta p)_i^{NX} &\approx b_0 \hat{\mathbf{K}}_{0,i}^{NX} + b_1 \hat{\mathbf{K}}_{1,i}^{NX} + b_2 \mathbf{K}_{2,i}^{NX} + b_3 \hat{\mathbf{K}}_{3,i}^{NX} + b_4 \hat{\mathbf{K}}_{4,i}^{NX} \end{aligned}$$

where b_s ($s = 0, 1, 2, 3, 4$) are computed for each Δp by using the matrix $\mathbf{A}$ and the expression in Eq. (3.7). Note that the five coefficients b_s which depend on the actual Δp are easily calculated because they are just five scalars that depend only on Δp and δp irrespective of the size of the finite element mesh.

Finally, the mass and stiffness matrices for the i^{th} component of the NX-PROMs can be partitioned as follows

$$\begin{aligned} \mathbf{M}(p_0 + \Delta p)_i^{NX} &= \begin{bmatrix} \mathbf{M}_{\Delta p,i}^{C} & \mathbf{M}_{\Delta p,i}^{CN} \\ \mathbf{M}_{\Delta p,i}^{NC} & \mathbf{M}_{\Delta p,i}^{N} \end{bmatrix}, \\ \mathbf{K}(p_0 + \Delta p)_i^{NX} &= \begin{bmatrix} \mathbf{K}_{\Delta p,i}^{C} & \mathbf{K}_{\Delta p,i}^{CN} \\ \mathbf{K}_{\Delta p,i}^{NC} & \mathbf{K}_{\Delta p,i}^{N} \end{bmatrix}, \end{aligned} \tag{3.10}$$

where superscript C indicates a constraint partition, and superscript N indicates a nominal mode partition.

3.4 Local-Interface Reduction

If the finite element mesh used is very fine, the size of the reduced system-level matrices is dominated by the constraint DOFs corresponding to the C partition in Eq. (3.10). The constraint DOFs of matrices constructed by CMS-based techniques are difficult to reduce. This is an important issue because, if the constraint DOFs cannot be reduced, then the overall structure cannot be efficiently divided into many substructures. To address this issue, Castanier *et al.* [11] suggested the use of characteristic constraint (CC) modes. This technique is based on performing a secondary eigenanalysis of the constraint partition (C) of the system-level mass and stiffness matrices constructed by CB-CMS. This technique is applied after the system-level matrices are constructed. However, the core idea of NX-PROMs is that all analyses are accomplished at the substructure-level, and not at the system-level. Thus, an alternate interface reduction technique is proposed next. The

new approach is applied at the substructure-level, and it is referred to as local-interface reduction (LIR).

The local-interface reduction technique is also based on a secondary eigenanalysis of the constraint partition. However, the secondary eigenanalysis is executed on the constraint partitions (C) of the substructural matrices, not the system-level matrices. The secondary eigenanalyses on constraint DOFs (C) of the mass and stiffness matrices of component i constructed by either CB-CMS or the NX-PROM approach are given by

$$\mathbf{K}^{C}_{\Delta p,i}\mathbf{\Phi}^{CC}_{\Delta p,i} - \mathbf{M}^{C}_{\Delta p,i}\mathbf{\Phi}^{CC}_{\Delta p,i}\mathbf{\Lambda}_{\Delta p,i} = \mathbf{0},$$

where $\mathbf{\Lambda}_{\Delta p,i}$ is a diagonal matrix which contains the eigenvalues, and $\mathbf{\Phi}^{CC}_{\Delta p,i}$ are the characteristic constraint (CC) modes of the i^{th} substructure. They are truncated for the frequency range of interest by using the eigenvalues in $\mathbf{\Lambda}_{\Delta p,i}$. The rows of the CC modes indicate the constraint DOFs of the substructure, and the columns represent the set of truncated CC modes. The CC modes for each substructure are used to reduce the interface DOFs $for\ each\ boundary\ locally$. Note that joining all CC modes for each interface between different components may lead to vectors which are not necessarily linearly independent. However, they span the adequate space. Thus, the left singular values of the CC interface modes may have to be used for certain interfaces. To demonstrate the LIR procedure, a simple plate model is used in Sec. 3.6.2.

The set of orthogonal basis vectors used for all interfaces that a component i has with other components are grouped in a block diagonal matrix which contains the entire interface component i has. The number of blocks is equal to the number of components that are connected to component i. These matrices are denoted by $\mathbf{U}_{\Delta p,i}$. Of course, if component i connects to only one other component, then there is only one block in $\mathbf{U}_{\Delta p,i}$. Next, the

mass and stiffness matrices in Eq. (3.10) are projected using $\mathbf{U}_{\Delta p,i}$ as follows

$$\begin{aligned}\mathbf{M}^{CC}_{\Delta p,i} &= \mathbf{U}^{\mathrm{T}}_{\Delta p,i}\mathbf{M}^{C}_{\Delta p,i}\mathbf{U}_{\Delta p,i},\ \ \mathbf{M}^{CCN}_{\Delta p,i} = \mathbf{U}^{\mathrm{T}}_{\Delta p,i}\mathbf{M}^{CN}_{\Delta p,i},\ \ \mathbf{M}^{NCC}_{\Delta p,i} = \mathbf{M}^{CN}_{\Delta p,i}\mathbf{U}_{\Delta p,i},\\ \mathbf{K}^{CC}_{\Delta p,i} &= \mathbf{U}^{\mathrm{T}}_{\Delta p,i}\mathbf{K}^{C}_{\Delta p,i}\mathbf{U}_{\Delta p,i},\ \ \mathbf{K}^{CCN}_{\Delta p,i} = \mathbf{U}^{\mathrm{T}}_{\Delta p,i}\mathbf{K}^{CN}_{\Delta p,i},\ \ \mathbf{K}^{NCC}_{\Delta p,i} = \mathbf{K}^{CN}_{\Delta p,i}\mathbf{U}_{\Delta p,i}.\end{aligned} \tag{3.11}$$

Thus, the final mass and stiffness matrices with reduced constraint DOFs are given for component i by

$$\mathbf{M}^{LIR}_{\Delta p,i} = \begin{bmatrix} \mathbf{M}^{CC}_{\Delta p,i} & \mathbf{M}^{CCN}_{\Delta p,i} \\ \mathbf{M}^{NCC}_{\Delta p,i} & \mathbf{M}^{N}_{\Delta p,i} \end{bmatrix},\ \mathbf{K}^{LIR}_{\Delta p,i} = \begin{bmatrix} \mathbf{K}^{CC}_{\Delta p,i} & \mathbf{K}^{CCN}_{\Delta p,i} \\ \mathbf{K}^{NCC}_{\Delta p,i} & \mathbf{K}^{N}_{\Delta p,i} \end{bmatrix},$$

where superscript LIR indicates that the matrices are constructed using local-interface reduction. An example is provided in Sec. 3.6.2.

3.5 Assembly

To predict the system-level dynamics, the mass and stiffness matrices obtained in Sections 3.3 and 3.4 for each substructure have to be assembled. To do that, geometric compatibility conditions must be enforced. In the following, we discuss separately the case where LIR is not used and the case where it is used.

Let us consider the case where the geometric compatibility conditions are used for models without LIR. In this case, the constraint partitions (C) of component-level matrices keep the meaning of the physical interface DOFs of matrices obtained from FEMs. This means that the geometric compatibility conditions between interface DOFs (constraint DOFs) can be applied directly to construct the system-level matrices. The complete component-level equations of motion for component i based on CB-CMS or the NX-PROM approach can be expressed as

$$\mathbf{M}^{ROM}_{i}\ddot{\mathbf{q}}^{ROM}_{i} + \mathbf{K}^{ROM}_{i}\mathbf{q}^{ROM}_{i} = \mathbf{F}^{ROM}_{i}, \tag{3.12}$$

where ROM indicates component-level matrices obtained using either CB-CMS or the NX-PROM approach. The stiffness matrices in Eq. (3.12) obtained for components without parameter variability can be expressed as

$$\mathbf{K}_i^{ROM} = \mathbf{K}_i^{CBCMS} = \begin{bmatrix} \mathbf{K}_i^{C} & \mathbf{K}_i^{CN} \\ \mathbf{K}_i^{NC} & \mathbf{K}_i^{N} \end{bmatrix}^{CBCMS} . \tag{3.13}$$

For component with parameter variability, the stiffness matrices in Eq. (3.12) can be expressed as

$$\mathbf{K}_i^{ROM} = \mathbf{K}_i^{NX} = \begin{bmatrix} \mathbf{K}_{\Delta p,i}^{C} & \mathbf{K}_{\Delta p,i}^{CN} \\ \mathbf{K}_{\Delta p,i}^{NC} & \mathbf{K}_{\Delta p,i}^{N} \end{bmatrix}^{NXPROM} . \tag{3.14}$$

The formulas for the mass matrices are similar to those for the system matrices in Eqs. (3.13) and (3.14) (and are omitted here for the sake of brevity).

Next, the matrices in Eq. (3.12) are grouped for all i to obtain

$$\begin{aligned} \hat{\mathbf{M}} &= \mathbf{Bdiag}\begin{bmatrix} \mathbf{M}_1^{ROM} & \dots & \mathbf{M}_n^{ROM} \end{bmatrix}, \\ \hat{\mathbf{K}} &= \mathbf{Bdiag}\begin{bmatrix} \mathbf{K}_1^{ROM} & \dots & \mathbf{K}_n^{ROM} \end{bmatrix}, \\ \hat{\mathbf{F}} &= \begin{bmatrix} \mathbf{F}_1^{ROM\,\mathrm{T}} & \dots & \mathbf{F}_n^{ROM\,\mathrm{T}} \end{bmatrix}^{\mathrm{T}}, \end{aligned} \tag{3.15}$$

where n is the number of components, and $\mathbf{Bdiag}[\cdot]$ denotes a block-diagonal matrix.

The geometric compatibility condition for the ROM is expressed as

$$\mathbf{q}_i^C = \mathbf{q}_j^C, \tag{3.16}$$

where, $\mathbf{q}_i$ and $\mathbf{q}_j$ are the generalized coordinates for the constraint partitions (C for CB-CMS or NX-PROMs) that correspond to the interface between components i and j. Of course, there is no compatibility condition to be enforced for two components which do not have a common interface.

Equation (3.16) is used to transform the matrices in Eq. (3.15) similar to the assembly process in all finite element modeling methods. The final assembled, reduced-order, system-level matrices are given by

$$\begin{aligned}
\mathbf{M}_{sys}^{ROM} &= \begin{bmatrix} \mathbf{M}^{C} & \mathbf{M}^{CN} \\ \mathbf{M}^{NC} & \mathbf{M}^{N} \end{bmatrix}, \mathbf{K}_{sys}^{ROM} = \begin{bmatrix} \mathbf{K}^{C} & \mathbf{K}^{CN} \\ \mathbf{K}^{NC} & \mathbf{K}^{N} \end{bmatrix}, \\
\mathbf{F}_{sys}^{ROM} &= \begin{bmatrix} \mathbf{F}^{C} \\ \mathbf{F}^{N} \end{bmatrix},
\end{aligned}$$

where

$$\begin{aligned}
\mathbf{K}^{CN} &= \begin{bmatrix} \mathbf{K}_1^{CN} & \mathbf{K}_2^{CN} & \cdots & \mathbf{K}_n^{CN} \end{bmatrix}, \ \mathbf{K}^{NC} = \mathbf{K}^{CN^{\mathrm{T}}}, \\
\mathbf{K}^{N} &= \begin{bmatrix} \mathbf{K}_1^{N} & \mathbf{0} & \cdots & \mathbf{0} \\ \mathbf{0} & \mathbf{K}_2^{N} & \cdots & \mathbf{0} \\ \vdots & \vdots & \ddots & \mathbf{0} \\ \mathbf{0} & \mathbf{0} & \cdots & \mathbf{K}_n^{N} \end{bmatrix},
\end{aligned}$$

and $\mathbf{K}^{C}$ is a matrix which is obtained by the assembly of each interface. In general, $\mathbf{K}^{C}$ is a matrix which has a smaller size than the C partitions in $\hat{\mathbf{K}}$. The same process is applied to obtain $\mathbf{F}^{C}$. Also, similar relations are obtained for the mass matrix $\mathbf{M}_{sys}^{ROM}$ (and are omitted here for the sake of brevity).

Finally, the compatibility conditions for models constructed using LIR can be expressed almost identically to those for models without LIR. The only difference is that the generalized coordinates in Eq. (3.16) represent amplitudes of characteristic constraint modes or amplitudes of the basis vectors used to capture the space spanned by the characteristic constraint modes.

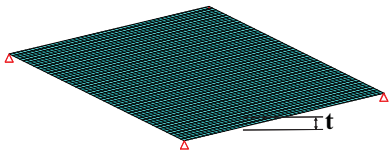

Figure 3.3: Simple plate structure modeled with shell-type elements

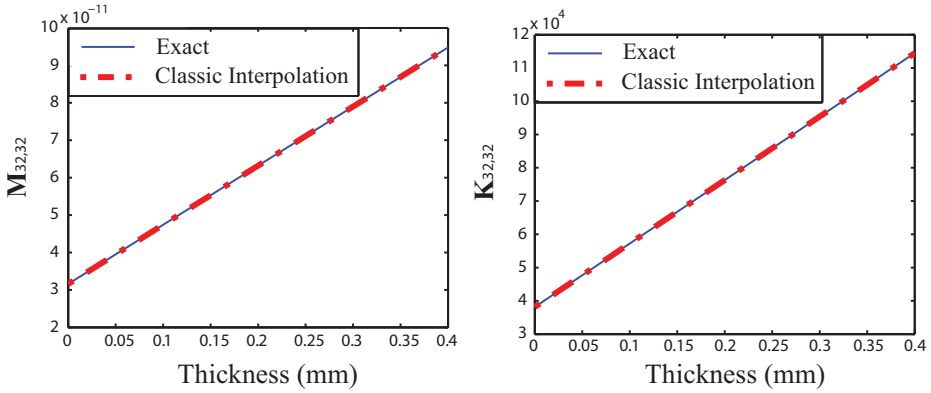

Figure 3.4: The 32^{nd} diagonal entries of the exact and the parametrized mass and stiffness matrices obtained by using a classic cubic interpolation for shell-type elements

3.6 Numerical Results

3.6.1 Element-level nonlinearity of brick and other types of finite elements

Figure 3.3 shows a simple plate structure modeled with a shell-type finite elements, where t is the thickness of the plate ($t = 0.2\ mm$). To examine the variation in the entries of the finite element mass and stiffness matrices for this substructure, the thickness t is varied by increments of $\Delta t = 0.01\ mm$.

The size of the mass and stiffness matrices of the simple structure shown in Fig. 3.3 is $15,582 \times 15,582$. As an example, the 32^{nd} diagonal entries of the mass and stiffness matrices, $\mathbf{M}_{32,32}$ and $\mathbf{K}_{32,32}$, are shown in Fig. 3.4 as the thickness varies (approximated matrices are shown by a dash-dot line, and the actual matrices are shown by a solid-line for

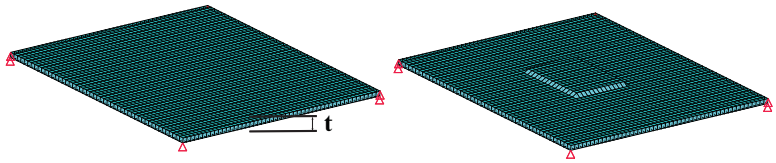

Figure 3.5: Simple plate structure modeled with brick-type elements

various values of Δp). One may observe that those entries of the mass and stiffness matrices vary almost linearly. To capture these variations very accurately, a cubic interpolation is used as follows

$$\mathbf{K}(p_0 + \Delta p) \approx \tilde{\mathbf{K}}_0 + \tilde{\mathbf{K}}_1 \Delta p + \tilde{\mathbf{K}}_2 \Delta p^2 + \tilde{\mathbf{K}}_3 \Delta p^3. \tag{3.17}$$

The matrices $\tilde{\mathbf{K}}_0$, $\tilde{\mathbf{K}}_1$, $\tilde{\mathbf{K}}_2$, and $\tilde{\mathbf{K}}_3$ are computed by using the stiffness matrices evaluated at three parameter values. These values are the reference value p_0, the first perturbed value $p_1 = p_0 + \delta p$, the second perturbed value $p_2 = p_0 + 2\delta p$ and the third perturbed value $p_3 = p_0 + 3\delta p$. The procedure is standard and similar to the one used in Sec. 3.2, so its details are omitted here for the sake of brevity. A similar interpolation is used for the mass matrix. Note that, in contrast to Taylor series, the cubic interpolation does not require the calculation of derivative terms.

Next, to examine the variations in the entries of the mass and stiffness matrices for brick-type elements, the same plate structure is modeled with brick-type elements. The nominal thickness of the plate is (the same) $0.2\ mm$ and is varied by (the same) increments of $\Delta t = 0.01\ mm$, as shown in Fig. 3.5. The thickness is varied in a region near the center of the plate. The entries of the mass and stiffness matrices near the DOFs where the thickness is varied are affected. A sample DOF affected is the 645^{th}. The 645^{th} diagonal entry of the mass matrix varies linearly (and is omitted for the sake of brevity). The same entry of the stiffness matrix, however, does not vary linearly, as shown in Fig. 3.6 (left),

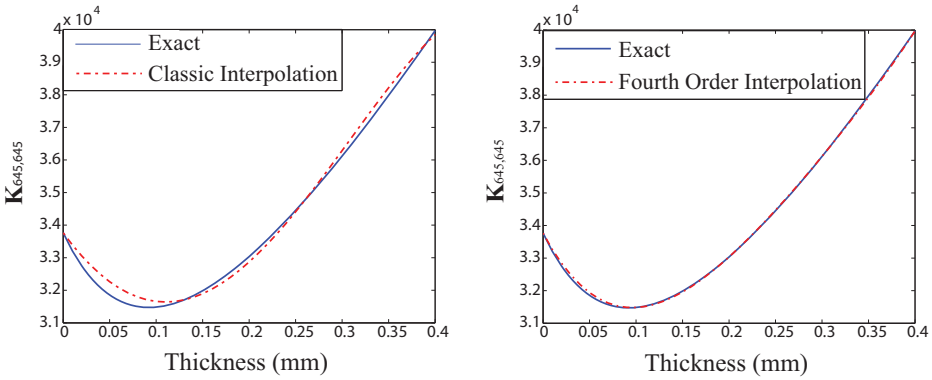

Figure 3.6: The 645^{th} diagonal entry of the exact and the parametrized stiffness matrices obtained by using a classic cubic interpolation (left) and an classic fourth order interpolation (right) for brick-type elements

where exact values are shown by a solid-line. To capture this nonlinear variation, the cubic interpolation function in Eq. (3.17) is used. The approximate values obtained are shown by a dash-dot line. These results show that Eq. (3.17) is not good enough to capture the highly nonlinear variation of the stiffness matrix. Therefore, a fourth-order interpolation is used as follows

$$\mathbf{K}(p_0 + \Delta p) \approx \tilde{\mathbf{K}}_0 + \tilde{\mathbf{K}}_1 \Delta p + \tilde{\mathbf{K}}_2 \Delta p^2 + \tilde{\mathbf{K}}_3 \Delta p^3 + \tilde{\mathbf{K}}_4 \Delta p^4. \tag{3.18}$$

This fourth-order interpolation captures well the nonlinear variation in the entries of the stiffness matrix as shown in Fig. 3.6 (right).

Based on the results in Fig. 3.6, one may assume that the errors obtained based on Eq. (3.18) are negligible. However, that is not correct, as demonstrated by the forced response of the plate calculated using exact and approximated matrices. Figure 3.7 shows the forced response at one of the DOFs on the plate for excitation frequencies near the first resonance. The solid-line represents the response computed by the actual mass and stiffness matrices, and the dash-dot line indicates the response computed by the mass and stiffness matrices parametrized using Eq. (3.18) for the case of $\Delta t = 0.37\ mm$. Clearly,

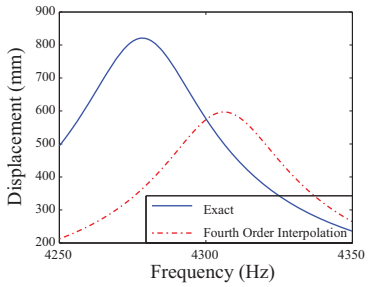

Figure 3.7: Forced responses calculated for $\Delta p = 0.37\ mm$ using the exact and parametrized mass and stiffness matrices obtained based on a fourth-order interpolation for brick-type elements

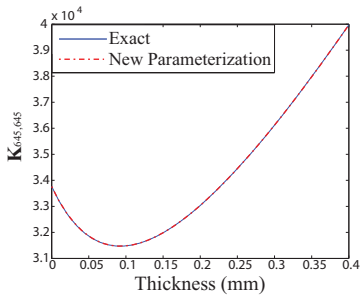

Figure 3.8: The 645^{th} diagonal entry of the exact and the parametrized stiffness matrices obtained by using the new interpolation for brick-type elements

the forced response computed by the parametrized mass and stiffness matrices does not agree with that computed by the actual matrices. This means that the errors in the entries of the stiffness matrix from the fourth-order interpolation are not small enough to capture accurately the dynamic response of the structure with a modified thickness. Note that, the errors in the dynamic response are induced by inaccuracies in the stiffness matrix, not in the mass matrix. These results demonstrated that a new parameterization technique focused on capturing element-level nonlinear variations in the stiffness is needed for brick-type finite elements.

The parametrized stiffness matrix was calculated using Eq. (3.7) for $\Delta p = 0.37\ mm$.

Table 3.1: 10 lowest natural frequencies for exact and parametrized matrices with volume variations

Mode	Exact	Approximated
1	4278.24	4278.24
2	9024.39	9011.52
3	9068.45	9053.21
4	14323.12	14323.11
5	24952.70	24952.34
6	25024.01	25023.94
7	27463.11	27460.10
8	27656.15	27654.70
9	36098.49	36098.51
10	41275.58	41262.95

As a sample of results, Fig. 3.8 shows that the 645^{th} diagonal entry of the exact and the approximated stiffness matrices match extremely well. Similar matches are observed for all entries of the matrices. Next, forced responses were calculated using these matrices. The results are shown in Fig. 3.9. The solid-line indicates the response computed using the exact matrices, and the dash-dot line indicates the response computed by using the new parametrized matrices. The results closely match. Moreover, the natural frequencies for the exact matrices and the new parametrized matrices, match also, as shown in Tab. 3.1.

3.6.2 Example of local-interface reduction

Consider a structure composed of 5 substructures and 3 boundaries as shown in Fig. 3.10. Γ_j represents the j^{th} boundary. First, using the constraint partitions (C) of the reduced

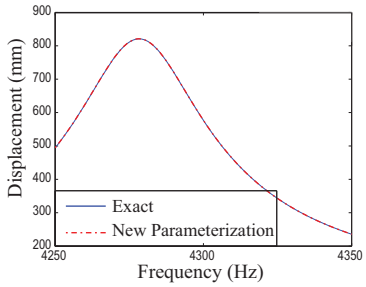

Figure 3.9: Forced response calculated for $\Delta p = 0.37\ mm$ using the exact and the parametrized mass and stiffness matrices obtained based on the new interpolation for brick-type elements

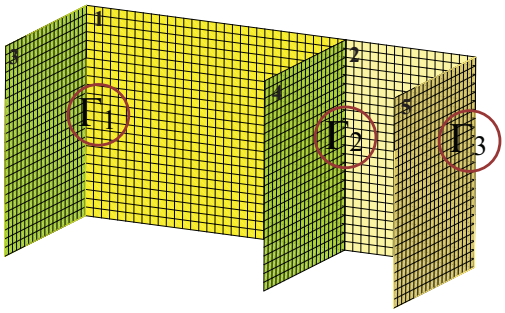

Figure 3.10: A simple structure used to demonstrate the local-interface reduction

mass and stiffness matrices, the CC modes are computed. These are $\mathbf{\Phi}^{CC}_{\Delta p,1}$, $\mathbf{\Phi}^{CC}_{\Delta p,2}$, $\mathbf{\Phi}^{CC}_{\Delta p,3}$, $\mathbf{\Phi}^{CC}_{\Delta p,4}$ and $\mathbf{\Phi}^{CC}_{\Delta p,5}$. $\mathbf{\Phi}^{CC}_{\Delta p,1}$ has interface DOFs for boundary Γ_1 and Γ_2, while $\mathbf{\Phi}^{CC}_{\Delta p,2}$ has interface DOFs for Γ_2 and Γ_3. Substructures 3, 4 and 5 each have one boundary Γ_1, Γ_2, and Γ_3, respectively. The mathematical representation for these partitions for each CC mode can be expressed as

$$\boldsymbol{\Phi}^{CC}_{\Delta p,1} = \begin{bmatrix} \left(\boldsymbol{\Phi}^{CC}_{\Delta p,1}\right)^{\Gamma_1} \\ \left(\boldsymbol{\Phi}^{CC}_{\Delta p,1}\right)^{\Gamma_2} \end{bmatrix}, \quad \boldsymbol{\Phi}^{CC}_{\Delta p,2} = \begin{bmatrix} \left(\boldsymbol{\Phi}^{CC}_{\Delta p,2}\right)^{\Gamma_2} \\ \left(\boldsymbol{\Phi}^{CC}_{\Delta p,2}\right)^{\Gamma_3} \end{bmatrix},$$
$$\boldsymbol{\Phi}^{CC}_{\Delta p,3} = \left(\boldsymbol{\Phi}^{CC}_{\Delta p,3}\right)^{\Gamma_1}, \quad \boldsymbol{\Phi}^{CC}_{\Delta p,4} = \left(\boldsymbol{\Phi}^{CC}_{\Delta p,4}\right)^{\Gamma_2}, \quad \boldsymbol{\Phi}^{CC}_{\Delta p,5} = \left(\boldsymbol{\Phi}^{CC}_{\Delta p,5}\right)^{\Gamma_3}.$$

By using each boundary partition of the CC modes, the augmented set of CC modes for each boundary is constructed as

$$\begin{aligned} \boldsymbol{\Phi}^{\Gamma_1}_{\Delta p,\text{aug}} &= \begin{bmatrix} \left(\boldsymbol{\Phi}^{CC}_{\Delta p,1}\right)^{\Gamma_1} & \left(\boldsymbol{\Phi}^{CC}_{\Delta p,3}\right)^{\Gamma_1} \end{bmatrix}, \\ \boldsymbol{\Phi}^{\Gamma_2}_{\Delta p,\text{aug}} &= \begin{bmatrix} \left(\boldsymbol{\Phi}^{CC}_{\Delta p,1}\right)^{\Gamma_2} & \left(\boldsymbol{\Phi}^{CC}_{\Delta p,2}\right)^{\Gamma_2} & \left(\boldsymbol{\Phi}^{CC}_{\Delta p,4}\right)^{\Gamma_2} \end{bmatrix}, \\ \boldsymbol{\Phi}^{\Gamma_3}_{\Delta p,\text{aug}} &= \begin{bmatrix} \left(\boldsymbol{\Phi}^{CC}_{\Delta p,2}\right)^{\Gamma_3} & \left(\boldsymbol{\Phi}^{CC}_{\Delta p,5}\right)^{\Gamma_3} \end{bmatrix}. \end{aligned} \tag{3.19}$$

Equation (3.19) describes the augmented CC bases for boundaries Γ_1, Γ_2, and Γ_3. However, the augmented bases $\boldsymbol{\Phi}^{\Gamma_1}_{\Delta p,\text{aug}}$, $\boldsymbol{\Phi}^{\Gamma_2}_{\Delta p,\text{aug}}$, and $\boldsymbol{\Phi}^{\Gamma_3}_{\Delta p,\text{aug}}$ are not guaranteed to be linearly independent. Thus, they cannot be directly used to reduce the constraint DOFs because of lack of numerical stability. Thus, an orthogonal basis for the space spanned by the augmented CC basis is used. Specifically, the left singular vectors $\tilde{\mathbf{U}}^{\Gamma_1}_{\Delta p}$, $\tilde{\mathbf{U}}^{\Gamma_2}_{\Delta p}$ and $\tilde{\mathbf{U}}^{\Gamma_3}_{\Delta p}$ of the three augmented CC bases $\boldsymbol{\Phi}^{\Gamma_1}_{\Delta p,\text{aug}}$, $\boldsymbol{\Phi}^{\Gamma_2}_{\Delta p,\text{aug}}$, and $\boldsymbol{\Phi}^{\Gamma_3}_{\Delta p,\text{aug}}$ in Eq. (3.19) are computed for each substructure, and the left singular vector corresponding to singular values larger than 0.01% of the maximum singular value are selected for each boundary. The rows of the orthogonal bases $\tilde{\mathbf{U}}^{\Gamma_1}_{\Delta p}$, $\tilde{\mathbf{U}}^{\Gamma_2}_{\Delta p}$ and $\tilde{\mathbf{U}}^{\Gamma_3}_{\Delta p}$ are (re)sorted for each substructure to match the interface DOFs for each boundary. The resorted matrices are denoted by $\mathbf{U}^{\Gamma_1}_{\Delta p}$, $\mathbf{U}^{\Gamma_2}_{\Delta p}$ and $\mathbf{U}^{\Gamma_3}_{\Delta p}$. The (re)sorted matrices are grouped for each component i to obtain matrices $\mathbf{U}_{\Delta p,i}$ which $\mathbf{U}_{\Delta p,i}$ are used to project the interface DOFs onto the secondary generalized coordinates (CC domain). For example, substructure 1 includes the Γ_1 and Γ_2 boundaries. To reduce the interface DOFs of substructure 1, the orthogonal bases $\mathbf{U}^{\Gamma_1}_{\Delta p}$ and $\mathbf{U}^{\Gamma_2}_{\Delta p}$ are

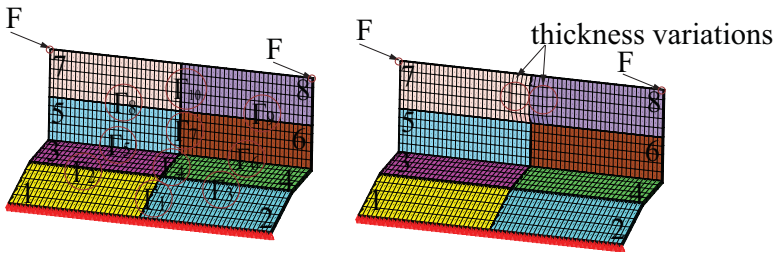

Figure 3.11: An L-shaped plate shown without thickness variation (left) and with thickness variation (right); interfaces between components are denoted by Γ_i

grouped in a matrix $\mathbf{U}_{\Delta p,1}$ given by

$$\mathbf{U}_{\Delta p,1} = \begin{bmatrix} \mathbf{U}_{\Delta p}^{\Gamma_1} & \mathbf{0}^{\Gamma_1} \\ \mathbf{0}^{\Gamma_2} & \mathbf{U}_{\Delta p}^{\Gamma_2} \end{bmatrix}. \tag{3.20}$$

The orthogonal basis for substructure 2 is constructed in the same way, to obtain

$$\mathbf{U}_{\Delta p,2} = \begin{bmatrix} \mathbf{U}_{\Delta p}^{\Gamma_2} & \mathbf{0}^{\Gamma_2} \\ \mathbf{0}^{\Gamma_3} & \mathbf{U}_{\Delta p}^{\Gamma_3} \end{bmatrix}. \tag{3.21}$$

For some of the substructures, the grouping of $\mathbf{U}_{\Delta p}^{\Gamma}$ matrices is not necessary. For example, the bases used for substructures 3, 4 and 5 are simply given by

$$\mathbf{U}_{\Delta p,3} = \mathbf{U}_{\Delta p}^{\Gamma_1}, \;\; \mathbf{U}_{\Delta p,4} = \mathbf{U}_{\Delta p}^{\Gamma_2}, \;\; \text{and} \;\; \mathbf{U}_{\Delta p,5} = \mathbf{U}_{\Delta p}^{\Gamma_3} \tag{3.22}$$

Next, the orthogonal basis for each substructure is constructed using Eqs. (3.20), (3.21) and (3.22), and the interface DOFs (C) of the NX-PROMs generalized coordinates are projected into the secondary generalized CC coordinates as shown in Eq. (3.11).

3.6.3 L-shaped plate modeled with brick-type finite elements

To demonstrate the proposed NX-PROM and LIR methodologies, an L-shaped structure modeled with brick-type elements (shown in Fig. 3.11) and containing thickness variations is investigated numerically. Figure 3.11 shows the pristine structure and the structure

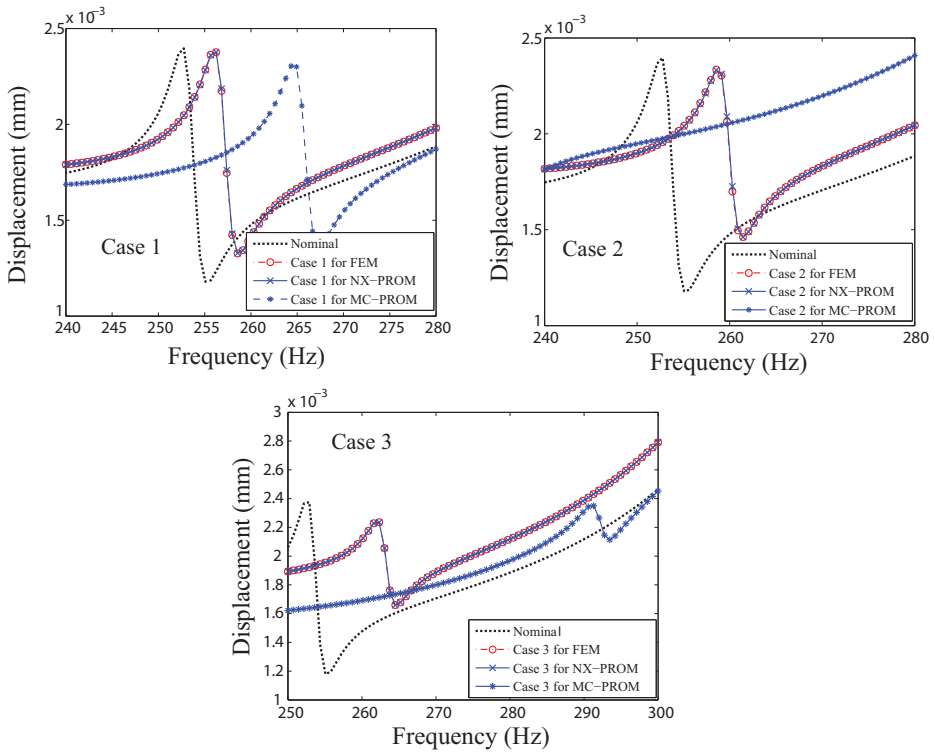

Figure 3.12: Forced response predictions of the L-shaped plate for the nominal structure and for cases 1, 2 and 3 computed using full-order models, MC-PROMs and the novel NX-PROMs

with thickness variations. The structure consists of eight substructures. Substructures 7 and 8 have three cases of thickness variations, as given in Tab. 3.2. The nominal thickness of the structure is $1\ mm$ and the elemental thickness is $0.2\ mm$. The thickness variations applied are very large compared to the nominal elemental thickness considered. This causes the entries of the mass and stiffness matrices to vary nonlinearly. CB-CMS is applied for the 1^{st} to the 6^{th} substructure, and the NX-PROM approach is applied for the 7^{th} and the 8^{th} substructures.

Figure 3.12 shows the system-level forced responses of the nominal structure and the three cases of thickness variation. The dotted lines represent the vibration response of the nominal structure. The crosses and circles represent the responses of the structure

Table 3.2: Thickness variations in substructures 7 and 8 of the L-shaped plate

Substructure	Thickness, case 1	Thickness, case 2	Thickness, case 3
7	$1.00\ mm \rightarrow 1.22\ mm$	$1.00\ mm \rightarrow 1.42\ mm$	$1.00\ mm \rightarrow 1.81\ mm$
8	$1.00\ mm \rightarrow 1.22\ mm$	$1.00\ mm \rightarrow 1.42\ mm$	$1.00\ mm \rightarrow 1.81\ mm$

with thickness variations predicted using NX-PROMs and full-order models, respectively. To reveal the enhanced performance of the NX-PROMs, the vibration response predicted by MC-PROMs is also shown by the stars in Fig. 3.12. For all three cases, the forced response predicted by the full-order models and the NX-PROMs show excellent matching. However, the forced responses predicted by MC-PROMs are not accurate compared to the full-order models. This is due to the fact that MC-PROMs cannot capture the volume variation of brick-type finite elements, which leads to poor predictions of the vibration response. Note also that the thickness variations affect significantly the structure, as shown by the significant differences between the response of the nominal structure and the other responses.

The number of DOFs of the full-order model and the NX-PROMs are 18,300 and 3,502, respectively. The system-level DOFs of the NX-PROMs include 3,000 interface DOFs and 502 generalized internal DOFs. The number of generalized internal DOFs is small. However, the number of interface DOFs is large, and should be reduced. Thus, the LIR technique described in Sec. 3.4 was applied. Fig. 3.11 shows the interfaces which are reduced, where Γ_m indicates the m^{th} interface. Fig. 3.13 shows the forced responses for the nominal structure and the three cases of thickness variations. The dotted lines represent the response of the nominal structure. The crosses and circles indicate the responses of the structure with thickness variations predicted using NX-PROMs with full interface DOFs

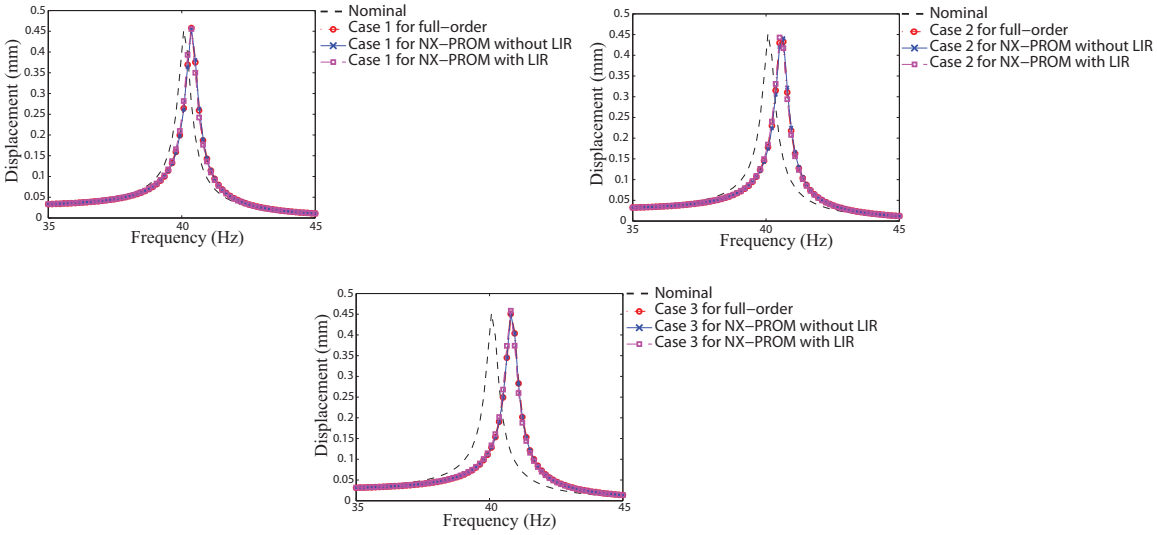

Figure 3.13: Forced response predictions of the L-shaped plate for the nominal structure and for cases 1, 2 and 3 computed using full-order models, NX-PROM, and NX-PROM with LIR

and full-order models, respectively. The squares represent the responses predicted using NX-PROMs with LIR. These latter models use only 533 interface DOFs, reduced by LIR from 2,498. The response predicted by NX-PROMs with LIR agree very well with the responses of the full-order model.

3.6.4 Results for a high mobility multipurpose wheeled vehicle model

In this section, NX-PROMs are used to predict the dynamic response of a realistic vehicle model. We consider the base frame of a high mobility multipurpose wheeled vehicle (HMMWV). The finite element model for the HMMWV is a conventional model used to examine its dynamic response [30–32, 35, 64]. Figure 3.14 shows the system-level and substructure-level finite element models of the HMMWV frame. The cross-bar structure is composed of substructures C_L and C_R, which are modeled with solid-

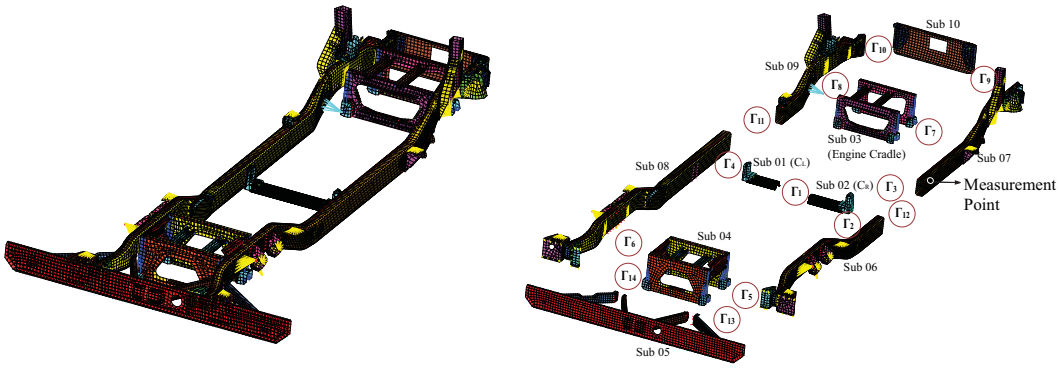

Figure 3.14: System-level and substructure-level finite element models of the frame of a high mobility multipurpose wheeled vehicle

Table 3.3: Thickness variations in substructures C_L and C_R of the HMMWV frame

Substructure	Thickness, case 1	Thickness, case 2
C_L	$5\ mm \rightarrow 20\ mm$	$5\ mm \rightarrow 32\ mm$
C_R	$5\ mm \rightarrow 20\ mm$	$5\ mm \rightarrow 32\ mm$

type finite elements, as shown in Fig. 3.15. The marked region in Fig. 3.15 indicates the nodes which move due to thickness variation. Tab. 3.3 indicates two cases of thickness variation for C_L and C_R. The thickness variations applied are much larger than those used in the L-shaped example. We chose these large variations to demonstrate that the proposed methods are very accurate even when the thickness variations are very large. Such large variations are encountered in practice especially when components are re-designed. The structural and the elemental thicknesses of the C_L and C_R substructures are $5\ mm$ and $2.5\ mm$, respectively. NX-PROMs were created for the C_L and C_R substructures, and CB-CMS was applied to the remaining substructures. Next, forces and moments were applied to the engine cradle, and the resulting forced response were computed. Figure 3.16 shows the response of the HMMWV frame for cases 1 and 2. The measured point is

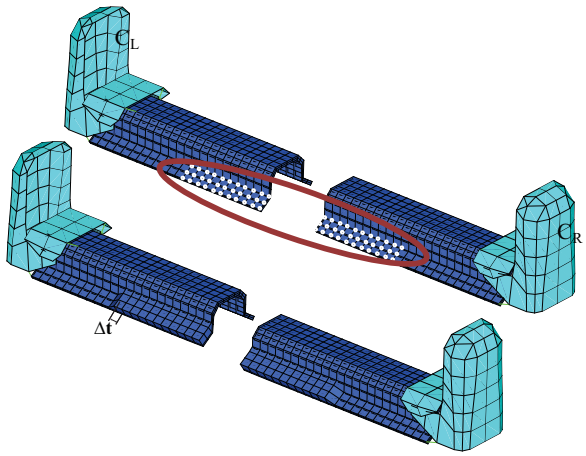

Figure 3.15: Nominal and re-designed cross-bar composed of C_L and C_R

shown in Fig. 3.14. The dotted line shows the forced response of the nominal HMMWV structure. The circles and crosses indicate the responses of the re-designed HMMWV frame predicted by full-order models and NX-PROMs, respectively. The stars show the responses predicted by MC-PROMs. Results obtained using the full-order models and the NX-PROMs show excellent agreement for both cases 1 and 2, but the results predicted by MC-PROMs do not agree well with the response obtained using the full-order models. Also, note that the re-design has important effects on the structure, as demonstrated by the significant difference between the responses of the nominal and the re-designed structures.

The full-order model of the HMMWV has 123,201 DOFs. The NX-PROMs have 2,683 DOFs, of which 1,473 are constraint DOFs and 1,210 are fixed-interface generalized DOFs. To reduce the number of constraint DOFs, LIR was applied. Figure 3.14 shows the interfaces of the substructures in the HMMWV frame. Tab. 3.4 shows what are the

Table 3.4: Interfaces between substructures in the HMMWV model

Interface \ Substructure	1	2	3	4	5	6	7	8	9	10
Γ_1	O	O								
Γ_2	O								O	
Γ_3	O							O		
Γ_4		O					O			
Γ_5			O						O	
Γ_6			O				O			
Γ_7				O				O		
Γ_8				O		O				
Γ_9					O			O		
Γ_{10}					O	O				
Γ_{11}						O	O			
Γ_{12}								O	O	
Γ_{13}									O	O
Γ_{14}							O			O

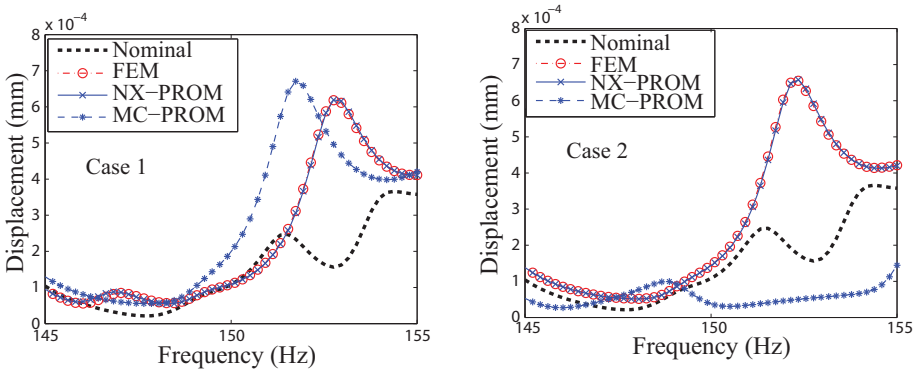

Figure 3.16: Forced response predictions for the HMMWV frame for the nominal structure and for cases 1 (top) and 2 (bottom)

interface DOFs for each substructure. Figure 3.17 shows the response of the HMMWV model predicted by NX-PROMs for cases 1 and 2 using different levels of reduction of the overall interface DOFs. Magnified plots near the resonant frequencies are included also. Note that the accuracy of the response predicted by LIR depends on the number of remaining interface DOFs. In these two cases, an acceptable accuracy is obtained when the remaining interface DOFs are not fewer than approximately 1,000.

3.7 Conclusions and Discussion

The key contributions of this paper are as follows. The proposed next-generation parametric reduced-order models (NX-PROMs) were developed by using a new parameterization technique to capture the element-level nonlinearity due to volume variations of finite elements of brick or other types. In addition, to establish a mathematically stable formulation for NX-PROMs, a new transformation matrix was developed using a novel interpolation of static constraint modes. Finally, a local-interface reduction (LIR) technique was proposed for further enhancing the computational efficiency of the NX-PROMs.

Novel, next-generation parametric reduced order models (NX-PROMs) for predicting

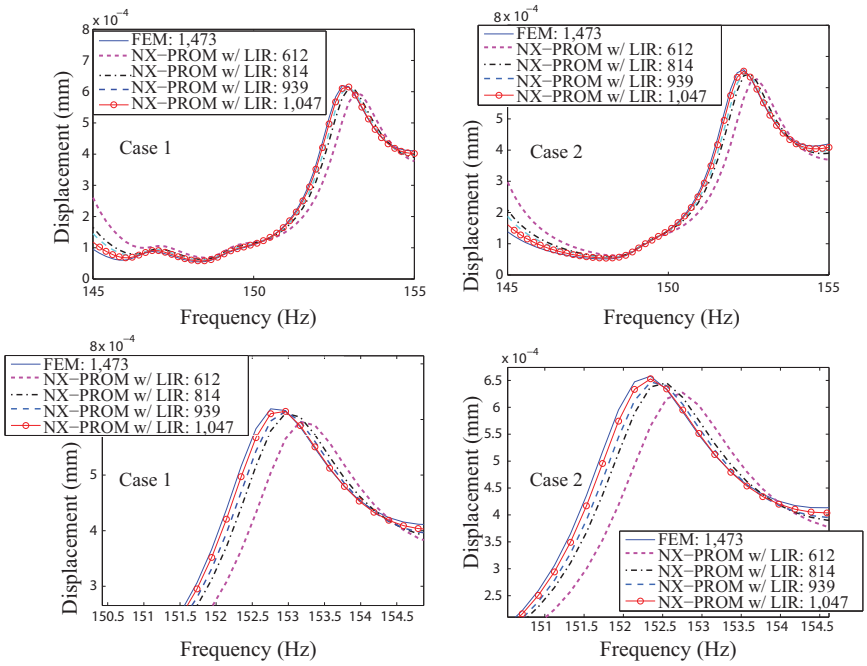

Figure 3.17: Forced response predictions for the HMMWV frame obtained using NX-PROMs with LIR for different levels of reduction; the total number of DOFs obtained for each model using LIR are indicated for case 1 (left) and 2 (right)

the vibration response of complex structures have been presented. These models address two main drawbacks of MC-PROMs. The first is that the parameterization techniques used in MC-PROMs cannot capture the thickness variation of brick and other types of finite elements due to element-level nonlinearity of the stiffness matrix. The second drawback is that the transformation matrix for MC-PROMs is not numerically stable. Thus, a new parameterization technique was developed to capture the nonlinearity of the stiffness matrix, and a new transformation matrix was proposed to make the NX-PROMs more stable numerically and more accurate compared to MC-PROMs.

To reduce the interface DOFs, a new method called local-interface reduction (LIR) was developed. NX-PROMs were developed for realistic substructural analysis. In such cases, the interface DOFs should be reduced before the system-level matrices are constructed.

The LIR technique uses characteristic constraint modes computed $for\ each\ substructure$ by using the constraint partition of the reduced mass and stiffness matrices constructed by CB-CMS or the NX-PROM approach. By using these characteristic constraint modes, orthogonal bases were defined to reduce the interface DOFs of each substructure. That is a key advantage of this reduction technique, and it is very useful for substructural analysis.

Similar to MC-PROMs, the novel NX-PROMs also provide smaller system matrices and shorter analysis and reanalysis time to predict the vibration response of complex structures. This means that NX-PROMs are especially useful for the repetitive analyses needed in optimization problems where geometric changes are applied in the design cycle for structures modeled with brick and other types of finite elements.

CHAPTER IV

Robust Signal Processing for Damaged Vehicles with Variability

4.1 Introduction

Vibration-based structural health monitoring (SHM) techniques are of current interest in identifying damage and assessing the integrity of structures such as ground vehicles. Predicting the dynamic characteristics of damaged structures is an important challenge for vibration-based SHM. The numbers of degrees of freedom (DOFs) of the finite element models used to predict the dynamic response of complex structures are prohibitively large, so conventional finite element analysis are hard to employ. Thus, alternative techniques have been developed recently to predict the dynamic response of complex structures with models having a dramatically lower number of DOFs [6–10]. These reduced-order models (ROMs) are increasingly used to predict the vibration response of the structures, especially their resonant frequencies and mode shapes, using a short computational time and a low computational cost. One method for constructing ROMs is based on the fixed-interface component mode synthesis (CB-CMS) [7]. That well known approach is employed herein for a few portions of the model. Specifically, CB-CMS is useful and applied only to the invariant components of overall/entire structures. A component is considered invariant if it does not have any geometrical or structural variations. However, for the vibration-

based SHM, the challenge is to predict the vibration characteristics of damaged structures, not those of pristine structures. If one attempts to use standard reduced order modeling techniques when parametric changes (such as thickness and geometrical variations) are applied by design or exist through damage, the finite element model has to be modified, and new ROMs have to be reconstructed (through a reanalysis) to predict the structural vibration response. That is a manual and a very costly process computationally. Recently, design oriented ROMs have been developed to avoid such prohibitively expensive reanalyses of complex structures. These models are parametric reduced order models (PROMs). Initially, global PROMs have been developed (see e.g. the work of [28, 29]). However, global PROMs are impractical because they require one to repeatedly solve many sample eigenproblems for the entire structure. Thus, component-mode-based PROMs [30] have been developed to adopt component normal modes and characteristic constraint modes as projection basis instead of global modes. However, constructing component-mode-based PROMs as done in [30] is also time consuming because the approach still requires the calculation of system-level (global) interface modes. Thus, [32] introduced truly component-level analysis for constructing PROMs, referred to as component-PROMs. However, in their approach, component-PROMs can be applied only to one component. Thus, the multiple-component PROMs (MC-PROMs) have been developed by the authors [35] and are adopted herein to allow complex structures to be divided into several, much simpler, substructures. Each substructure can have variability in characteristics such as geometric parameters (e.g. thickness) or material properties (e.g. Young's modulus).

In this work, PROM techniques employing CB-CMS and MC-PROM are applied to analyze the vibration response of a cracked complex structure. Also, note that the cracked structure generates a nonlinear dynamic problem because of the nonlinear contact force between the crack surfaces. One approach to handle this nonlinear contact force is to use

a hybrid frequency-time domain (HFT) method developed by [36], [37], and [65]. In that method, a forced response analysis is applied to determine the resonant frequencies of the cracked structure. While powerful, that approach is computationally intensive, and difficult to use to predict resonant responses (due to the nonlinearity). Thus, an alternate approach (based on linear analyses) has been developed for predicting resonant frequencies. The alternate approach builds on earlier work on the bilinear frequency approximation (BFA) [39]. The resonant frequencies predicted by the generalized BFA have been shown to agree very well with those obtained using nonlinear HFT analyses for applications such as cracked turbine bladed disks [40]. Herein, the concept of BFA is adopted together with the bilinear mode approximation (BMA) [66]. BMA is introduced to approximate the mode shapes of cracked structures. In addition, to reduce computational cost for BMA, PROM techniques based on CB-CMS and MC-PROMs are used.

The characteristics of the dynamic response obtained using PROMs technique are useful signals for vibration-based SHM. However, all signals obtained from PROM cannot be used in practice due to limited accessibility constraints and cost of the needed sensors. Thus, robust signal processing techniques to find the best sensor locations are an important challenge. There are many previous studies of sensor placement for SHM. For example, Ansari [41] has implemented SHM strategies which require selection and placement of sensors suitable for measuring key parameters that influence the performance and health of civil structures. Flynn and Todd [42] have proposed a novel approach for optimal actuator and sensor placement for SHM. Krommer *et al.* [43] have investigated a sensor network composed of strain-type patch sensors with constant intensity designed to replace distributed strain-type sensors for monitoring beam-type structures. Herein, a novel robust signal processing technique is employed to find the optimal number of sensor locations for gathering mode shape information of cracked structures. The novel approach is devel-

oped starting from an algorithm based on the effective independence distribution vector (EIDV) [44, 45]. The key idea of EIDV is to choose sensor locations for measuring physical mode shapes as linearly independent as possible in the frequency range of interest. Herein, the EIDV method is modified to select optimal sensor locations for cracked complex structures. The number of selected locations based on the modified EIDV method is not only limited to the frequency range of interest, but also limited in the effects of measurement noise. To address this noise, over-sampling is often performed. EIDV cannot provide optimal locations for over-sampling. Herein, a new signal processing technique is developed to select over-sampled measurement locations.

To approximate the mode shapes of cracked structures, BMA is formulated based on PROM mode shapes. For completeness, this paper briefly describes also the PROMs approach to construct models for structures with parametric variabilities. Finally, robust signal processing techniques are proposed to select the optimal and minimal sensor locations to capture the mode shapes of the structures. The technique to find optimal sensor locations is specifically designed for cases where the structure has structural variability and a crack.

4.2 Bilinear Mode Approximation

In this section, the mode shapes of a structure with a crack of various lengths are examined. When a structure has a crack, the resonant responses are hard to compute due to the nonlinearity of dynamics. This dynamics is caused by the periodic opening and closing of the crack surface (which leads to a piece-wise linear dynamics). Hence, to predict the mode shapes, standard modal analyses cannot be directly employed. To address this challenge, a novel technique to characterize the spatial correlations among the vibration of various points within the structure has been developed. These correlations are akin to

mode shapes, but they characterize the dynamics of the cracked (nonlinear) structure. This approach is based on the observation that, when the structure has a crack and vibrates at some (nonlinear) resonant frequency, two states can be identified: crack open and crack closed. These two states correspond to two shapes for the deformation of the structure at that frequency. Next, we assume that all the shapes the structure takes during its nonlinear vibration at a resonant frequency are linear combinations of these two shapes (open and closed at that resonant frequency). Furthermore, the open and closed shapes are assumed to be very similar to the shapes the structure would have if the crack surface were permanently open (i.e., penetration would be allowed) or permanently closed (with sliding occurring between DOFs within the crack surface). These linear modes can be easily computed by standard linear techniques. This novel approach is referred to as BMA, and complements BFA [39] originally developed for discrete low-dimensional systems and later generalized for cracked structures. The bilinear (BL) modes $\mathbf{\Phi}_{\mathrm{BL}}$ can be expressed as

$$\mathbf{\Phi}_{\mathrm{BL}} = \begin{bmatrix} \mathbf{\Phi}_{\mathrm{open}} \\ \\ \mathbf{\Phi}_{\mathrm{closed}} \end{bmatrix}, \tag{4.1}$$

where $\mathbf{\Phi}_{\mathrm{open}}$ are the mode shapes of the structure with a permanently open crack (penetration allowed) and $\mathbf{\Phi}_{\mathrm{closed}}$ are the mode shapes of the structure with a permanently closed crack (sliding allowed).

4.3 Parametric Reduced Order Models

In this section, the well known fixed-interface Craig-Bampton CMS (CB-CMS) method [7] and multiple-component parametric reduced-order models (MC-PROM) [35] used to construct PROMs for healthy substructures and substructures with parameter variations are briefly reviewed.

First, the CB-CMS approach [7] is used to model only the substructures which do not

have any structural variability. This modeling approach is used because it is very simple and computationally stable. Also, this technique is derivable because it can be exploited when modeling cracked structures by managing the geometric compatibility conditions between substructures. To apply CB-CMS, the complex structure of interest is partitioned into substructures, and the substructures have interface DOF and internal DOFs. The physical coordinates of these interface and internal DOFs are projected onto the generalized coordinates by using the fixed-interface normal mode ($\mathbf{\Phi}_i^N$) and static constraint mode ($\mathbf{\Psi}_i^C$). Then, the size of the mass and stiffness matrices, and force vector for substructure i are significantly reduced.

Second, MC-PROMs [35] are adopted to manage the substructures with variability in parameters such as Young's modulus and thickness variations. One important advantage of MC-PROMs is that the finite element mesh of the nominal structure does not need to be modified, although the substructures have parametric variability. That is because the mass and stiffness matrices are parameterized (by using Taylor series). For example, for a linear thin plate element, the modification of the stiffness matrix due to variations in the thickness of the plate can be accurately represented by a Taylor series up to third order within an upper and a lower limit for the parameterization. In addition, similar to the CB-CMS, an appropriate transformation matrix is constructed for converting from physical coordinates to generalized coordinates by using fixed-interface normal modes and static constraint modes. The distinct feature between CB-CMS and MC-PROM is that the transformation matrix for MC-PROM is constructed for all configurations in the parameter space of the corresponding component. In contrast, CB-CMS is applied only to components with no parameter variability.

The i^{th} and j^{th} component mass and stiffness matrices for CB-CMS and MC-PROM are partitioned as [35] and are explained as

$$\hat{\mathbf{M}}_i^{CMS} = \begin{bmatrix} \mathbf{m}_i^{CC} & \mathbf{m}_i^{CF} & \mathbf{m}_i^{CCN} \\ \mathbf{m}_i^{FC} & \mathbf{m}_i^{FF} & \mathbf{m}_i^{FFN} \\ \mathbf{m}_i^{NCC} & \mathbf{m}_i^{NFF} & \mathbf{m}_i^{NN} \end{bmatrix}, \quad \hat{\mathbf{K}}_i^{CMS} = \begin{bmatrix} \mathbf{k}_i^{CC} & \mathbf{k}_i^{CF} & \mathbf{k}_i^{CCN} \\ \mathbf{k}_i^{FC} & \mathbf{k}_i^{FF} & \mathbf{k}_i^{FFN} \\ \mathbf{k}_i^{NCC} & \mathbf{k}_i^{NFF} & \mathbf{k}_i^{NN} \end{bmatrix}, \tag{4.2}$$

$$\begin{aligned} \mathbf{M}_j^{PROM} &= \begin{bmatrix} \mathbf{m}_j^{CC_{00}} & \mathbf{m}_j^{CF_{00}} & \mathbf{m}_j^{CC_{0U}} & \mathbf{m}_j^{CF_{0U}} & \mathbf{m}_j^{CCN_{00}} \\ \mathbf{m}_j^{FC_{00}} & \mathbf{m}_j^{FF_{00}} & \mathbf{m}_j^{FC_{0U}} & \mathbf{m}_j^{FF_{0U}} & \mathbf{m}_j^{FFN_{00}} \\ \mathbf{m}_j^{CC_{U0}} & \mathbf{m}_j^{CF_{U0}} & \mathbf{m}_j^{CC_{UU}} & \mathbf{m}_j^{CF_{UU}} & \mathbf{m}_j^{CCN_{UU}} \\ \mathbf{m}_j^{FC_{U0}} & \mathbf{m}_j^{FF_{U0}} & \mathbf{m}_j^{FC_{UU}} & \mathbf{m}_j^{FF_{UU}} & \mathbf{m}_j^{FFN_{UU}} \\ \mathbf{m}_j^{NCC_{00}} & \mathbf{m}_j^{NFF_{00}} & \mathbf{m}_j^{NCC_{UU}} & \mathbf{m}_j^{NFF_{UU}} & \mathbf{m}_j^{N_d} \end{bmatrix}, \\ \mathbf{K}_j^{PROM} &= \begin{bmatrix} \mathbf{k}_j^{CC_{00}} & \mathbf{k}_j^{CF_{00}} & \mathbf{k}_j^{CC_{0U}} & \mathbf{k}_j^{CF_{0U}} & \mathbf{k}_j^{CCN_{00}} \\ \mathbf{k}_j^{FC_{00}} & \mathbf{k}_j^{FF_{00}} & \mathbf{k}_j^{FC_{0U}} & \mathbf{k}_j^{FF_{0U}} & \mathbf{k}_j^{FFN_{00}} \\ \mathbf{k}_j^{CC_{U0}} & \mathbf{k}_j^{CF_{U0}} & \mathbf{k}_j^{CC_{UU}} & \mathbf{k}_j^{CF_{UU}} & \mathbf{k}_j^{CCN_{UU}} \\ \mathbf{k}_j^{FC_{U0}} & \mathbf{k}_j^{FF_{U0}} & \mathbf{k}_j^{FC_{UU}} & \mathbf{k}_j^{FF_{UU}} & \mathbf{k}_j^{FFN_{UU}} \\ \mathbf{k}_j^{NCC_{00}} & \mathbf{k}_j^{NFF_{00}} & \mathbf{k}_j^{NCC_{UU}} & \mathbf{k}_j^{NFF_{UU}} & \mathbf{k}_j^{N_d} \end{bmatrix}, \end{aligned} \tag{4.3}$$

where the superscript 0 indicates the nominal parameter values, and the superscript U indicate quantities computed for the upper limit parameter values in Eq. (4.3).

To model the dynamics of cracked structures and to apply BMA, the partitioning of the structure is done such that all crack surfaces are along interfaces between adjacent substructures. That way, the crack model can be obtained by simply managing the geometric compatibility conditions. In Eqs. (4.2) and (4.3), the interface DOFs are divided into constraint DOFs (superscript CC) and free DOFs (superscript FF). For the open crack case, the DOFs between the crack surfaces are completely free, which means that those DOFs are allowed to inter-penetrate. These DOFs on the crack surfaces are free DOF (superscript FF) in Eqs. (4.2) and (4.3). For the closed crack case, sliding boundary

conditions are applied at the DOFs on the crack surfaces. Hence, the DOFs on the crack interface can slide, but they are not allowed to inter-penetrate. The constrained DOFs which are not allowed to inter-penetrate are denoted by superscript CC in Eqs. (4.2) and (4.3). The constrained (CC) and the free (FF) DOFs for the open and closed states of the cracked structure are different between shell-type and solid-type finite elements. That is because the DOFs of a nodal point are different between shell and solid-type finite elements. Thus, the DOF which are constrained (CC) or free (FF) for open and close state should be chosen carefully for each type of finite element. Using these two kinds of geometric compatibility conditions, the mode shapes of a cracked structure with an open crack and separately a closed crack are obtained through two separate linear analyses. Note also that, if component i has a crack surface, the component-level mass and stiffness matrices are partitioned as in [35].

Since all crack surfaces are at interfaces between components, all boundary DOFs are active DOFs. Finally, the geometric compatibility conditions used to assemble every substructure are applied only to the DOFs marked as CC in Eq. (4.2). The detailed formulation and description of PROMs technique are provided in [35].

4.4 Signal Processing for Cracked Structures

The objective of the signal processing technique is to select optimal sensor locations to represent the mode shapes of structures with various crack lengths. These mode shapes are useful in vibration-based SHM. An important related challenge is how to determine the frequency range of interest together with the sensor locations as to capture the shapes of the cracked structure during its vibration. Thus, a methodology to determine the sensitive modes due to the crack is investigated first.

4.4.1 Generalized modal assurance criterion

Some of the shapes of the resonant response of the healthy structure are similar to those of the cracked structure, and some are different. For instance, when the structure has a small crack, the mode shapes of the healthy structure are very similar to those of the cracked structure. Such a resonant response is not good for detecting the location and size of the crack. To address that, the most sensitive bilinear (BL) modes are used. To identify these BL modes, a modal assurance criterion (MAC) [67, 68] has been generalized and used to obtain the $\mathbf{MAC}$ matrix between the BL modes for the healthy and the cracked structures. The new $\mathbf{MAC}$ matrix needs the BL mass matrix obtained separately using ROMs for the open and closed crack vibration cases because the BL mode shapes for the open and closed states are mass normalized, and their sizes are different due to the distinct geometric compatibility conditions. The BL mass matrix can be expressed as

$$\mathbf{M}_{\mathrm{BL}} = \begin{bmatrix} \mathbf{M}_{\mathrm{ROM}}^{\mathrm{open}} & \mathbf{0} \\ \mathbf{0} & \mathbf{M}_{\mathrm{ROM}}^{\mathrm{closed}} \end{bmatrix}, \tag{4.4}$$

where the two mass matrices for open and closed states are obtained from ROMs. Herein, ROMs are obtained by using CB-CMS and MC-PROMs. This BL mass matrix is used together with the BL modes to define a new MAC as

$$\mathbf{MAC}_{ij} = \frac{[(\mathbf{\Phi}_{\mathrm{BL,i}}^{\mathrm{h}})^{\mathrm{T}}\mathbf{M}_{\mathrm{BL}}(\mathbf{\Phi}_{\mathrm{BL,j}}^{\mathrm{d}})]^2}{[(\mathbf{\Phi}_{\mathrm{BL,i}}^{\mathrm{h}})^{\mathrm{T}}\mathbf{M}_{\mathrm{BL}}(\mathbf{\Phi}_{\mathrm{BL,i}}^{\mathrm{h}})][(\mathbf{\Phi}_{\mathrm{BL,j}}^{\mathrm{d}})^{\mathrm{T}}\mathbf{M}_{\mathrm{BL}}(\mathbf{\Phi}_{\mathrm{BL,j}}^{\mathrm{d}})]}, \tag{4.5}$$

where the subscripts i and j indicate the i^{th} and j^{th} modes, and the BL mode shapes for the healthy structure (indicated by the superscript h) are defined as in Eq. (4.1) but for a zero crack length, while the BL modes for a non-zero crack are indicated by the superscript d. The value $\mathbf{MAC}_{ij}$ reflects how distinct is the i^{th} BL mode of the healthy structure from the j^{th} BL mode of the cracked structure. Note that the $\mathbf{MAC}$ matrix can be computed for structures with different crack lengths. The (diagonal) entries that correspond to non-

sensitive BL modes are close to 1.0 because the BL modes are normalized by the BL mass matrix. A specific example of selecting sensitive modes is shown in the next sections.

4.4.2 Modified effective independence distribution vector algorithm

In a practical implementation for structural inspection or damage identification, information of the BL modes has to be obtained through measurements by using sensors. To address that challenge, a signal processing algorithm for selecting the minimal and optimal locations to be measured or instrumented with sensors has been developed. This algorithm is generalized from a derivative of the EIDV method [45]. Generally, the EIDV method requires only a portion of the modal matrix of a structure in a frequency range of interest. This portion is allocated based on the generalized MAC discussed in the previous section and is applied to the BL modes and not the usual linear modes. The portion indicates also that the modal matrix has information of a set of candidate DOFs, not all DOFs of the structure. The partial modal matrix is used to compute a Fisher (information) matrix which, in turn, allows the computation of an effective independence distribution vector. This vector identifies the DOFs that are best to measure in terms of ensuring the linear independence of the measurements. To apply EIDV, the augmented bilinear modal matrix $\mathbf{\Phi}_{\text{aug}}^{\text{EIDV}}$ of the cracked structure is used instead of real nonlinear mode shapes of the cracked structure. $\mathbf{\Phi}_{\text{aug}}^{\text{EIDV}}$ is formed by grouping BL modes for the healthy structure (without a crack) $\hat{\mathbf{\Phi}}_{\text{BL}}^{\text{h}}$ and the BL modes for cracked structures with various crack lengths. The matrix $\hat{\mathbf{\Phi}}_{\text{BL}}^{\text{h}}$ and all mode shapes of various cracked structures are assembled in the frequency range of interest as follows

$$\mathbf{\Phi}_{\text{aug}}^{\text{EIDV}} = [\ \hat{\mathbf{\Phi}}_{\text{BL}}^{\text{h}}\ \ \hat{\mathbf{\Phi}}_{\text{BL}}^{a\%}\ \ \hat{\mathbf{\Phi}}_{\text{BL}}^{b\%}\ \ \cdots\ ], \tag{4.6}$$

where $\hat{\mathbf{\Phi}}_{\text{BL}}^{a\%}$ and $\hat{\mathbf{\Phi}}_{\text{BL}}^{b\%}$ indicate the modal matrices of cracked structures with a crack length of $a\%$ and $b\%$ of a reference length. This reference length can be interpreted as the largest

crack length of interest. Also, each modal matrix for the cracked structures can correspond to different frequency ranges because the sensitive modes can be different for each crack length. For instance, if the sensitive mode shapes based on $\mathbf{MAC}$ are 3^{rd}, 4^{th} and 5^{th} for the cracked structure with $a\%$ crack length, then the $\hat{\mathbf{\Phi}}_{\mathrm{BL}}^{a\%}$ modal matrix has only three coherences with candidate DOFs. However, the sensitive modes for the cracked structure with $b\%$ can be different and can contain more (or fewer) modes such as 4^{th}, 5^{th}, 6^{th} and 7^{th}.

If the number of sensors to be used are not sufficient and optimal to represent the modes of interest for the structure with various crack lengths, then the selected signals are very hard to use for vibration-based SHM. Hence, one must ensure that the sensors are placed optimally despite the fact that not all vectors $\hat{\mathbf{\Phi}}_{\mathrm{BL}}^{a\%}$, and $\hat{\mathbf{\Phi}}_{\mathrm{BL}}^{b\%}$ are necessarily linearly independent. Thus, the EIDV methodology was generalized. A subset of the left singular vectors $\mathbf{U}_{\mathrm{aug}}^{\mathrm{EIDV}}$ of $\mathbf{\Phi}_{\mathrm{aug}}^{\mathrm{EIDV}}$ is used instead of the full augmented modal matrix in Eq. (4.6). To select this subset, the singular values of $\mathbf{\Phi}_{\mathrm{aug}}^{\mathrm{EIDV}}$ are computed, and the left vectors corresponding to the largest singular values are selected.

Using the resulting matrix $\mathbf{U}_{\mathrm{aug}}^{\mathrm{EIDV}}$, the generalized EIDV algorithm for establishing locations for sensor placement can be summarized as follows.

(1) Calculate the BL modes for the healthy structure and cracked structures based on PROM (with crack lengths in a range of interest).

(2) Calculate the generalized $\mathbf{MAC}$ matrix using Eq. (4.5) and select sensitive modes for each crack length.

(3) Construct BL modes for the healthy and the cracked structures by selecting candidate measurement DOFs (by transforming PROM coordinates to physical coordinates) with the sensitive modes chosen at step (2).

(4) Construct the augmented BL modal matrix $\mathbf{\Phi}_{\text{aug}}^{\text{EIDV}}$ using Eq. (4.6).

(5) Apply singular value decomposition, and obtain the left singular vectors of $\mathbf{\Phi}_{\text{aug}}^{\text{EIDV}}$. Select the singular vectors $\mathbf{U}_{\text{aug}}^{\text{EIDV}}$ corresponding to the largest singular values.

(6) Calculate the Fisher information matrix given by $\mathbf{A} = \mathbf{U}_{\text{aug}}^{\text{EIDV}^{\text{T}}}\mathbf{U}_{\text{aug}}^{\text{EIDV}}$.

(7) Calculate the effective independence distribution vector, defined as the diagonal of the matrix $\mathbf{E} = \mathbf{U}_{\text{aug}}^{\text{EIDV}}\mathbf{A}^{-1}\mathbf{U}_{\text{aug}}^{\text{EIDV}^{\text{T}}}$.

The number of significant (or nontrivial) singular values of $\mathbf{\Phi}_{\text{aug}}^{\text{EIDV}}$ are indicative of the number of sensors needed for sensing and the generalized EIDV technique.

4.4.3 Over-sampled measurement locations

There are several possible criteria to assess the suitability of the selected measurement locations. They include the modal assurance criterion, the modified modal assurance criterion, the singular value decomposition, the measured energy per mode, and the Fisher information matrix [45]. Herein, the singular value decomposition is used to assess the suitability of selected measurement locations. The method simply evaluates the ratio of the largest to the smallest singular value of the BL modal matrix based on the measurement DOFs. If this ratio is close to unity, then the choice of measurement locations is good. In contrasts, the larger the ratio, the worst the choice of locations. Thus, if the ratio of the largest and smallest singular values of $\mathbf{U}_{\text{aug}}^{\text{EIDV}}$ with selected measurement DOFs is not close to 1.0, additional locations are likely necessary to guarantee linear independence of $\mathbf{U}_{\text{aug}}^{\text{EIDV}}$, especially in the presence of measurement noise.

Note that the number of selection points is dominated by the number of singular values of $\mathbf{\Phi}_{\text{aug}}^{\text{EIDV}}$ because the rank of the left singular vectors $\mathbf{U}_{\text{aug}}^{\text{EIDV}}$ (from $\mathbf{\Phi}_{\text{aug}}^{\text{EIDV}}$) which guarantees linear independence is same as the number of selected singular values. Thus, addi-

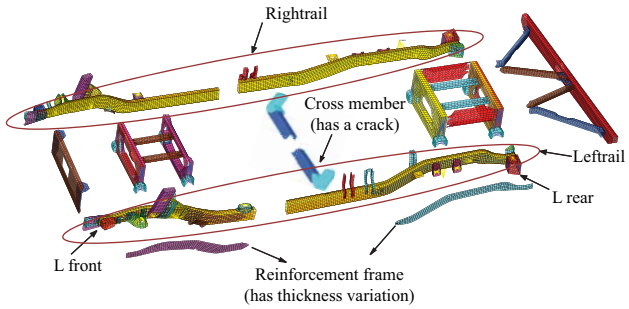

Figure 4.1: Substructuring of the HMMWV frame

tionally selected measurement locations based on the modified EIDV techniques cannot be chosen based on linear independence. Assumption of that fact is that the most important DOFs which are additionally selected are the DOFs nearest to the DOFs already selected. For instance, consider that the size of the matrix $\mathbf{U}_{\text{aug}}^{\text{EIDV}}$ is 300×5, where 300×5 indicates the number of candidate DOFs and the number of modes respectively. Consider also that number of modes (which is 5) is the same as the number of selected singular values. By using the modified EIDV technique, a maximum 5 measurement DOFs can be selected and the size of $\mathbf{U}_{\text{aug}}^{\text{EIDV}}$ (with the selected DOFs) is 5×5. However, if the ratio of the maximum and the minimum singular values for the final $\mathbf{U}_{\text{aug}}^{\text{EIDV}}$ (with the selected DOFs) is not closed to 1.0, then the 5 selected measurement locations are not enough to guarantee linear independence of the final $\mathbf{U}_{\text{aug}}^{\text{EIDV}}$. Thus, a new technique to select additional measurement DOFs in addition to the ones selected based on singular values is necessary to guarantee that the final augmented modal matrix has linearly independent columns (and thus, the ratio of the maximum and the minimum singular values of the final $\mathbf{U}_{\text{aug}}^{\text{EIDV}}$ is close to 1.0.). The additional measurement locations are referred to as over-sampled measurement locations.

Herein, a new technique to select over-sampled measurement locations is proposed.

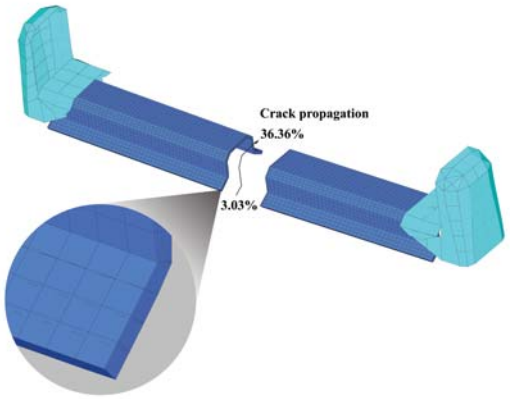

Figure 4.2: Substructure for the cracked cross-bar

Table 4.1: Thickness variations in substructures

Substructure	Case 1	Case 2
L_{rear}	3.038 mm $\rightarrow 5.562$ mm	3.038 mm $\rightarrow 4.114$ mm
L_{front}	3.038 mm $\rightarrow 4.991$ mm	3.038 mm $\rightarrow 3.552$ mm

Specifically, denote by $\mathbf{R}$ the left eigenvectors of $\mathbf{\Phi}_{\text{aug}}^{\text{EIDV}}$ which contain the remainder (unselected) DOFs, and denote by $\mathbf{S}$ the left eigenvectors of $\mathbf{\Phi}_{\text{aug}}^{\text{EIDV}}$ which contain the selected DOFs. After the generalized EIDV technique is executed, the $\mathbf{U}_{\text{aug}}^{\text{EIDV}}$ is divided into $\mathbf{S}$ and $\mathbf{R}$. The main idea is that $\mathbf{R}$ can be represented as a linear combination of the columns of $\mathbf{S}$ as follows,

$$\mathbf{R} = \mathbf{SC}, \tag{4.7}$$

where $\mathbf{C}$ is coefficient matrix which can be calculated using Eq. (4.7). By managing the matrix $\mathbf{C}$, the most important DOFs which should be added to previously selected DOFs (based on the generalized EIDV) can be selected. This procedure is applied until the

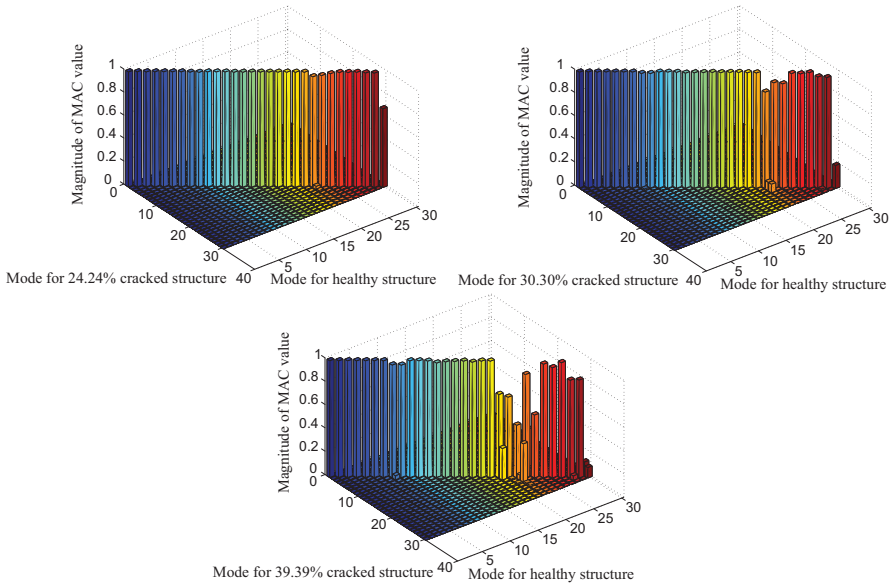

Figure 4.3: $\mathbf{MAC}$ between modes for healthy HMMWV and the structure with 24.24% crack, with 30.30% crack, and with 39.39% crack

desired number of over-sampled measurement DOFs is reached. Following is the specific procedure to select over-sampled measurement locations.

(1) The generalized EIDV technique is executed to select optimal measurement DOFs by using $\mathbf{U}_{\text{aug}}^{\text{EIDV}}$ with all candidate DOFs.

(2) The $\mathbf{U}_{\text{aug}}^{\text{EIDV}}$ is divided into $\mathbf{R}$ and $\mathbf{S}$.

(3) The coefficient matrix $\mathbf{C}$ is calculated by using Eq. (4.7).

(4) The standard deviation of the entries in each row of the matrix $\mathbf{C}$ is computed.

(5) The DOF which corresponds to the minimum standard deviation (computed at step (4)) is selected as an additional DOF to measure.

(6) The additional DOF is added to $\mathbf{S}$, and omitted from $\mathbf{R}$.

(7) Steps (3) to (6) are repeated until the desired number of additional DOFs is reached.

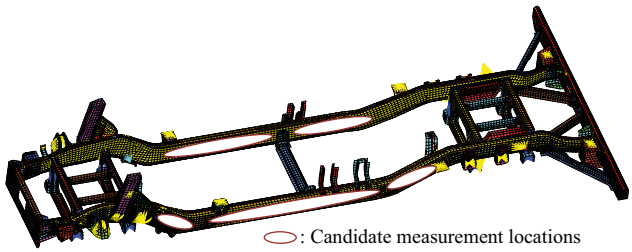

Figure 4.4: Finite element model for a HMMWV frame

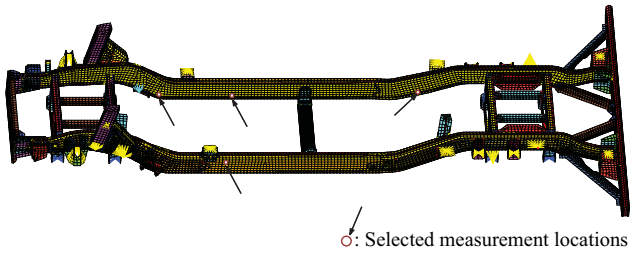

Figure 4.5: 4 optimal sensor locations based on the 30^{th} mode by using the modified EIDV method for cases 1 and 2 of thickness variation

4.5 Numerical Example

4.5.1 HMMWV models

In this section, we demonstrate the generalized EIDV techniques based on PROMs for a high mobility multipurpose wheeled vehicle (HMMWV) base frame with a crack. Figure 4.4 shows the finite element model along with the candidate measurement locations. Figure 4.1 shows each substructure of the HMMWV frame used to construct PROMs. The reinforcement frames in the rear and the front are attached to the leftrails and rightrails. The reinforcement frames which are attached to the leftrails have thickness variations as shown in Tab. 4.1. For example, a nominal thickness of L_{rear} of 3.038 mm (on the left of the arrow) is considered in case 1 to change to 5.562 mm (on the right of the arrow). The same nominal value of the thickness of L_{rear} is considered to change to 4.114 mm in case

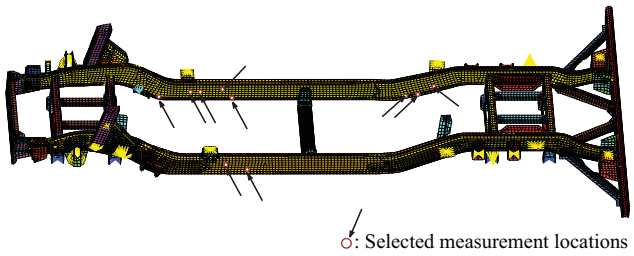

Figure 4.6: 10 optimal sensor locations based on the 30^{th} mode by using the modified EIDV method and the over-sampled algorithm for the case 1 of thickness variation

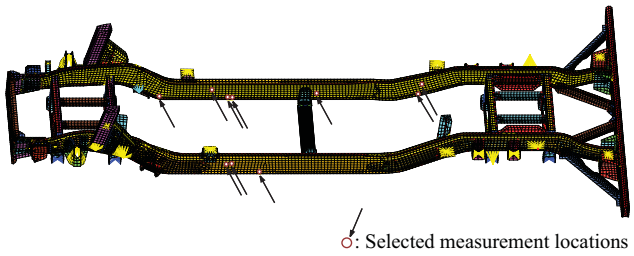

Figure 4.7: 10 optimal sensor locations based on the 30^{th} mode by using the modified EIDV method for the case 1 of thickness variation

2, and so on. The cross-member is considered to have a crack, as shown in Fig. 4.2. The crack length varies (across the cross-member component) from 3.03% to 36.36%. The CB-CMS method is applied for healthy substructures (the parts of the structure which do not have any variations). The MC-PROM method is implemented for the substructures with thickness variations. The BMA approach is implemented to approximate the BL modes of the cracked HMMWV frame.

To select the frequency range of interest, the sensitive BL modes are identified by using the generalized $\mathbf{MAC}$ matrix in Eq. (4.5). The crack lengths of interest are 24.24%, 30.30%, and 39.39%. Fig. 4.3 shows the $\mathbf{MAC}$ matrices computed between the healthy and the cracked structure with 24.24%, 30.30%, and 39.39% crack length. For these

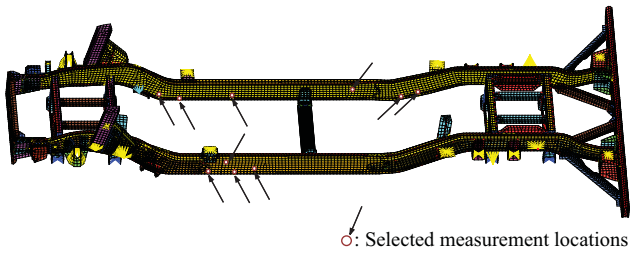

Figure 4.8: 10 optimal sensor locations based on the 30^{th} mode by using the modified EIDV method and the over-sampled algorithm for the case 2 of thickness variation

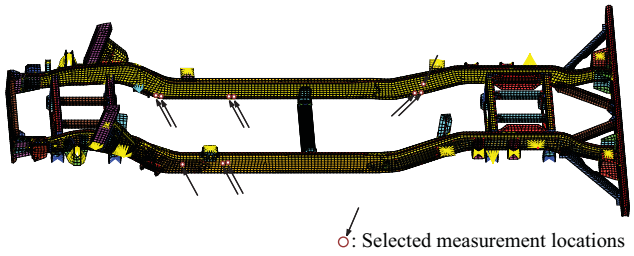

Figure 4.9: 10 optimal sensor locations based on the 30^{th} mode by using the modified EIDV method for the case 2 of thickness variation

cracked structures, the 30^{th} mode is the most sensitive compared to the healthy structure. Thus, the 30^{th} modes of the healthy and cracked structures are used to construct the augmented modal matrix $\mathbf{\Phi}_{\text{aug}}^{\text{EIDV}}$.

Next, the generalized EIDV technique is applied to obtain the optimal sensor locations. Figure 4.5 shows the best four sensor locations to capture the 30^{th} mode for the cases 1 and 2 of thickness variation. The BL mode shapes of the cracked structure are considered to be measured only at those four locations. The selected sensor locations are identical for each case of thickness variation. These results show that, for this structure, the optimal sensor locations are affected much more by the crack length than by the thickness variations.

The ratio of the largest and the smallest singular values of the set of left singular vec-

Table 4.2: The ratio of the largest and the smallest singular value

Case	Type of selection method	Ratio for singular value
1	Over-sampled	1.041
	Modified EIDV	1.197
2	Over-sampled	1.024
	Modified EIDV	1.212

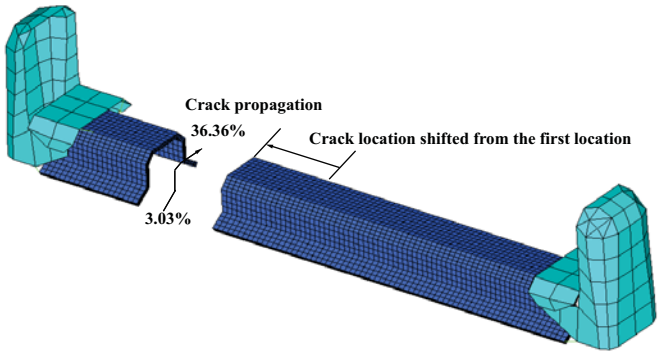

Figure 4.10: Cross-bar with a different crack location

tors (only with the selected measurement DOFs represented in Fig. 4.5) are not very close to 1.0. For the cases 1 and 2 of thickness variation, the ratios are 1.41. Thus, additional over-sampled measurement locations are needed. For that, 6 additional over-sampled measurement DOFs can be selected by the algorithm for over-sampled measurement locations. Figures 4.6 and 4.7 show these 6 additional over-sampled locations along with the 4 optimal sensor locations based on the modified EIDV method. These figures show also the 10 optimal sensor locations obtained only from the modified EIDV method for the case 1 of

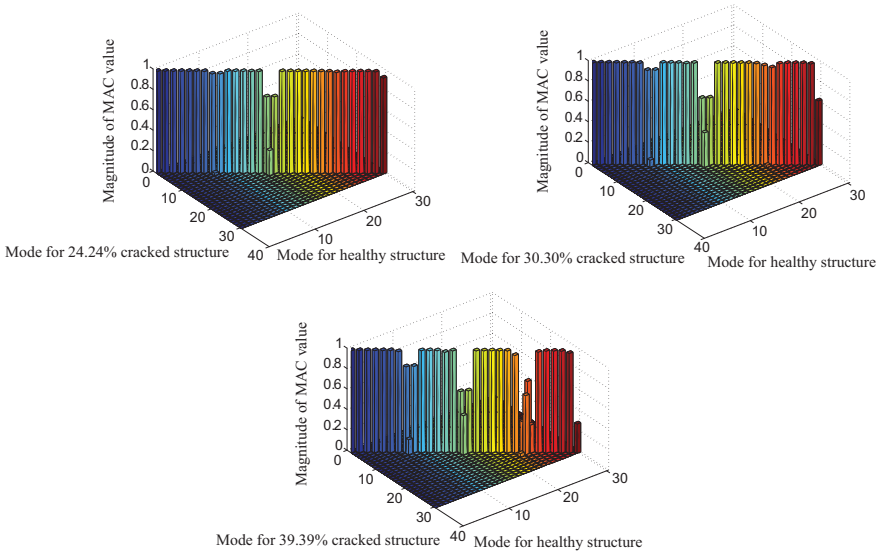

Figure 4.11: **MAC** between modes for healthy HMMWV and the structure with 24.24% crack, with 30.30% crack, and with 39.39% crack; crack is at a different location compared to Fig. 4.2

thickness variation. The 10 sensor locations in Fig. 4.6 (from the over-sampled algorithm) are well distributed. In contrast, some of the measurement locations in Fig. 4.7 (from the modified EIDV only) are doubled selected. This result demonstrates that the additional measurement locations above and beyond the number of selected singular values cannot be selected well by the modified EIDV method. Figures 4.8 and 4.7 also show the 10 optimal measurement locations for the case 2 of thickness variation by using the over-sampled algorithm and the EIDV method respectively. The results are similar to the results of case 1 of thickness variation. Table 4.2 shows the ratio of the largest and the smallest singular values of $\mathbf{U}_{\text{aug}}^{\text{EIDV}}$ with 10 measurement DOFs selected by generalized EIDV, and with 10 measurement locations selected by the generalized EIDV and over-sampled algorithm. The ratio of $\mathbf{U}_{\text{aug}}^{\text{EIDV}}$ with selected DOFs by using the over-sampled algorithm is closer to 1.0 because those 10 measurement locations are well distributed.

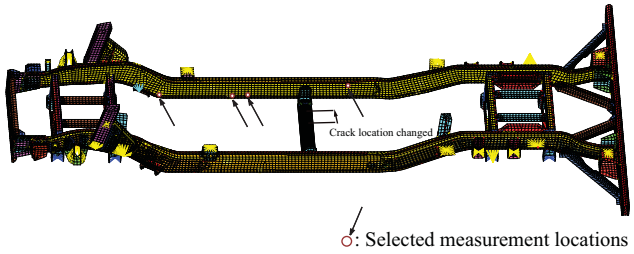

Figure 4.12: 4 optimal sensor locations based on the 30^{th} mode by using the modified EIDV method for cases 1 and 2 of thickness variation; crack is at a different location compared to Fig. 4.2

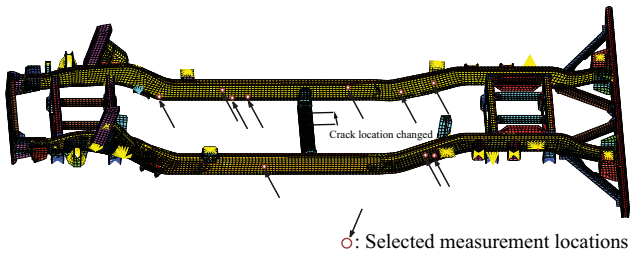

Figure 4.13: 10 optimal sensor locations based on the 30^{th} mode by using the modified EIDV method and the over-sampled algorithm for case 1 of thickness variation; crack is at a different location compared to Fig. 4.2

Additionally, we also investigated the sensor placement for a different crack location. In Fig. 4.2, the crack is located closed to the center of the cross-bar. Now, the crack is considered at a different location, as shown in Fig. 4.10. The crack lengths of interest are 24.24%, 30.30%, and 39.39% for the two cases of thickness variation listed in Tab. 4.1. Figure 4.11 shows the $\mathbf{MAC}$ matrices computed between the healthy and the cracked structure with the three crack lengths. For the shifted crack case, the 30^{th} mode is also the most sensitive compared to the healthy structure. Thus, the augmented modal matrix $\mathbf{\Phi}_{\text{aug}}^{\text{EIDV}}$ is constructed by using the 30^{th} mode.

Next, the generalized EIDV technique is applied to select the optimal sensor locations.

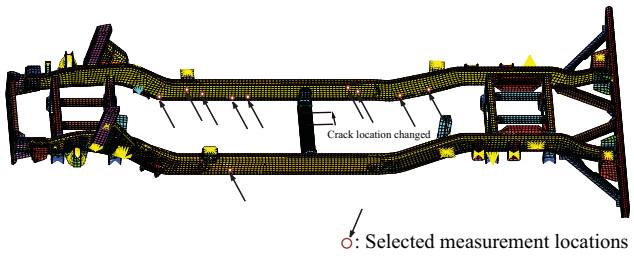

Figure 4.14: 10 optimal sensor locations based on the 30^{th} mode by using the modified EIDV method and the over-sampled algorithm for the case 2 of thickness variation; crack is at a different location compared to Fig. 4.2

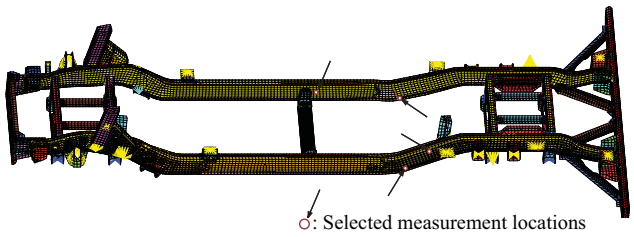

Figure 4.15: Statistically optimal sensor locations obtained from 400 cases of thickness variation; crack is at the first location (shown in Fig. 4.2)

Figure 4.12 shows the four optimal sensor locations for cases 1 and 2 of thickness variation. The selected sensor locations are identical for the two cases of thickness variation. That result is the same as for the first crack location considered. We also applied the generalized EIDV technique and the over-sampled algorithm to obtain 10 optimal sensor locations. Figures 4.13 and 4.14 indicate the 10 optimal sensor locations for cases 1 and 2 of thickness variation. The selected sensor locations for the case where the crack is at the new location are different compared to the sensor locations obtained for the first crack location considered. This indicates that the optimal sensor locations can be sensitive to the crack locations.

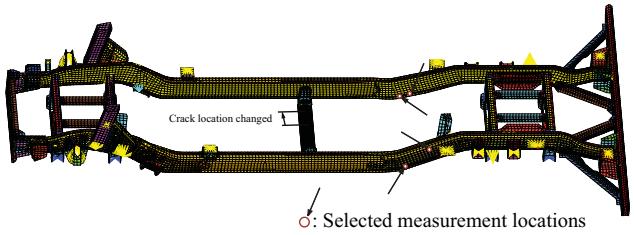

Figure 4.16: Statistically optimal sensor locations obtained from 400 cases of thickness variation; crack is at a different location compared to Fig. 4.2

4.5.2 Robust signal processing based on a Monte-Carlo technique

It is often desirable to select optimal and minimal sensor locations to capture the mode shapes of cracked structures. However, when the thickness of some components of the structure vary, the structural characteristics (especially mode shapes) are affected. Then, the optimal sensor locations may also be affected by the change in the mode shapes. That means that robust sensor locations are required to capture the mode shapes of the structures in the presence of thickness variations. Herein, a Monte-Carlo technique is applied to determine statistically optimal and robust sensor locations. To apply the Monte-Carlo technique, a large number of possible thickness variations are considered, and optimal sensor locations for the resulting mode shapes are obtained. To compute the mode shapes for each thickness variation, PROM techniques are applied. One of the main advantages of PROMs is that reanalysis (for each thickness variation) is almost 100 times faster because any parameter value in the parameter range can be easily applied [35].

The reinforcement frames in the rear and the front (which are attached to the leftrails) have thickness variations. For the Monte-Carlo technique, 400 separate cases of possible thickness variations are applied to these reinforcement frames. Each of the two reinforcement frames has been considered to have a thickness of a value randomly drawn from a

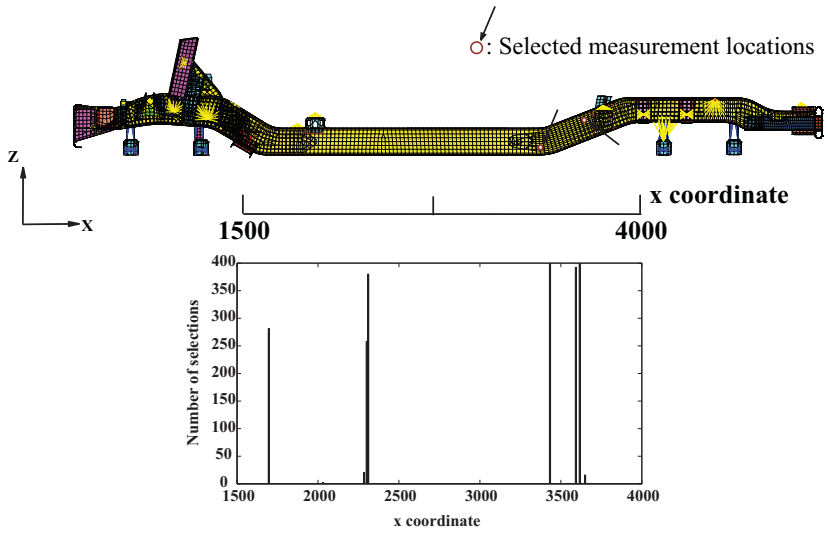

Figure 4.17: Optimal sensor locations for the leftrail frame structure for all cases of thickness variation; crack is at the first location (shown in Fig. 4.2)

uniform distribution between 3.038 mm and 6.038 mm. A total of 20 sample thicknesses were randomly selected for each of the 2 substructures (L_{front} and L_{rear}), and that leads to a total of 400 samples. The 26^{th} through the 30^{th} modes are identified and selected as sensitive modes (based on $\mathbf{MAC}$ matrices obtained using Eq. (4.5)) and are used for sensor placement. The total number of modes for the augmented bilinear modal matrix in Eq. (4.6) is 20. Then, the optimal number of measurement locations are decided based on the selected number of singular value of $\mathbf{\Phi}_{\text{aug}}^{\text{EIDV}}$ for each case of thickness variation. For instance, if all columns of $\mathbf{\Phi}_{\text{aug}}^{\text{EIDV}}$ in Eq. (4.6) are linearly independent, then the selected number of singular values is 20. In contrast, if the columns of $\mathbf{\Phi}_{\text{aug}}^{\text{EIDV}}$ are not linearly independent, then the selected number of singular values is smaller than 20. During the Monte-Carlo simulations, 14 or 15 optimal measurement locations are selected for each case of thickness variation. Then, only four measurement points are selected for all cases of thickness variation. These four selected measurement locations are chosen to be the

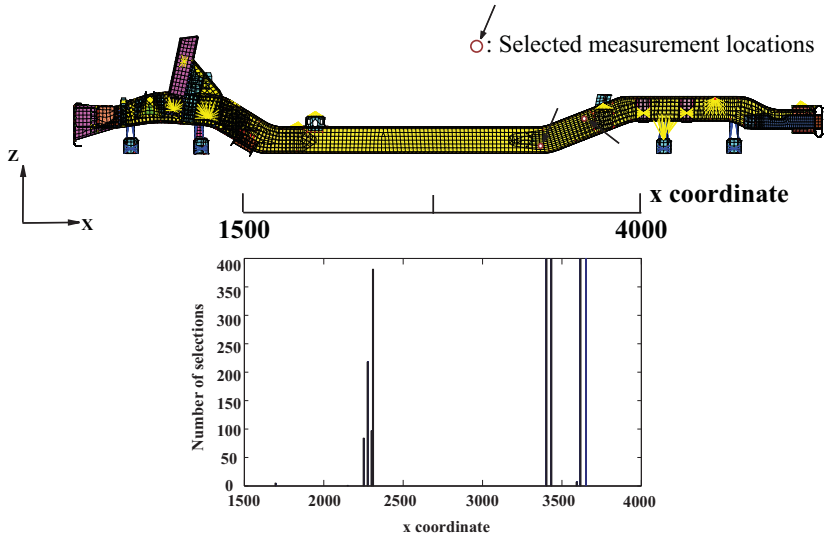

Figure 4.18: Optimal sensor locations for the leftrail frame structure for all cases of thickness variation; crack is at a different location compared to Fig. 4.2

statistically optimal locations. Thus, they are the most robust when used to capture the BL modes of the cracked structures for any thickness variation (in the range of interest). Figures 4.15 and 4.16 show the four statistically optimal measurement locations obtained for the first and the second crack locations. Figures 4.17 and 4.18 represent the distribution of optimal sensor locations chosen along the leftrail (i.e. along the x coordinate) for all cases of thickness variation for the first and the second crack locations. Also, Figs. 4.19 and 4.20 show the distribution of the sensor locations chosen along the rightrail. The distribution for all cases of thickness variation in Figs. 4.17-4.20 are slightly different for the two crack locations. However, statistically optimal sensor locations (which are the 4 locations most often selected) are almost identical, as shown in Figs 4.15 and 4.16. That indicates that the statistically optimal sensor locations are robust for the two cases of crack locations considered.

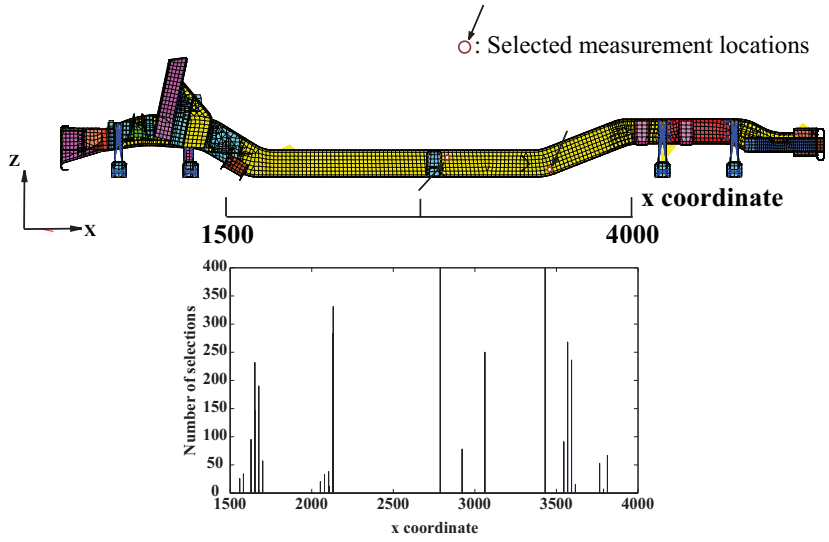

Figure 4.19: Optimal sensor locations for the rightrail frame structure for all cases of thickness variation; crack is at the first location (shown in Fig. 4.2)

4.6 Conclusions and Discussion

Identifying structural inspection points or desired sensor locations for the purpose of vibration-based structural health monitoring is an important challenge for cracked structures because of the nonlinearity created by the crack opening and closing. A new concept of bilinear (BL) modes has been used to address this issue. The BL modes are obtained using linear analysis techniques, and can be used to obtain BL mode approximations. To alleviate high computational costs in design applications and to find statistical simulation results based on Monte-Carlo simulations, a reduced order modeling method based on Craig-Bampton component mode synthesis and multi-component parametric reduced-order models was used. A generalized modal assurance criterion has been developed and used to find the BL modes that are most sensitive to the presence of a crack. Using the selected BL modes, an augmented BL modal matrix has been formed and used in an algorithm based on a modified effective independence distribution vector (EIDV) method

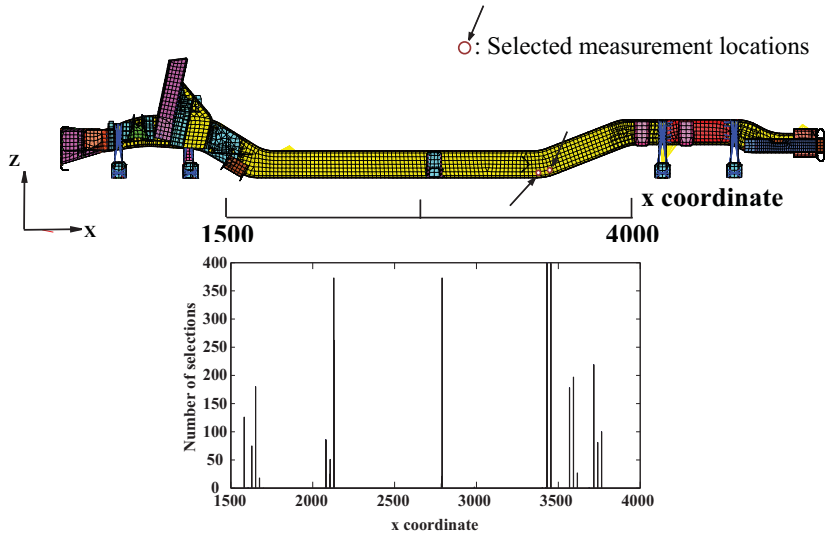

Figure 4.20: Optimal sensor locations for the rightrail frame structure for all cases of thickness variation; crack is at a different location compared to Fig. 4.2

to select optimal inspection points (or measurement locations). When the selected optimal measurement locations based on the generalized EIDV method are not enough to maintain the linear independence of the set of left singular vector, a novel over-sampled algorithm was applied to select additional measurement locations. Finally, the optimal set of measurement locations (for the cracked structure) was selected (by the generalized EIDV method and the over-sampled algorithm), and the measurement locations were assessed by the ratio of the largest and the smallest singular values of the set of the left singular vectors. To select robust sensor locations for any thickness variation in a range of interest, a Monte-Carlo technique was implemented based on PROMs to select statistically optimal measurement locations. 400 cases of possible thickness variation were considered for a HMMWV frame, and 4 statistically optimal and robust measurement locations were selected. These four points are robust and statistically optimal to capture the mode shapes of the cracked HMMWV structure.

The approach proposed is not a novel statistical analysis. Rather, PROMs provide a method to solve very quickly for samples rather than a method to choose parameter values where samples are to be computed. The user of the proposed solver can choose the statistical analysis method to be used. In this work, a Monte Carlo approach was used. Any sampling method can be used to obtain a statistical solution. For example, Latin Hypercube sampling can be used. Also, the number of samples to be used is a choice of the user. In general, more or fewer samples may be necessary depending on the specifics of the structure.

If one would choose to use a full-order model in the same statistical analysis (i.e. the same number of samples), then the computational time would increase dramatically compared to the computational cost of using PROMs. That is because each sample requires a much longer computational time when using a full-order model compared to PROMs. In addition, if a different method for statistical analysis is used (e.g., one that requires fewer samples than a Monte-Carlo approach), then using PROMs is faster because each sample is obtained faster.

If one ignores the possible structural variability altogether, and selects sensor locations based on a single calculation (for a single set of structural parameter values), then the selected measurement locations can be inadequate. That is because structural characteristics (such as mode shapes) are affected when there are changes in structural parameter values. As a consequence, the optimal sensor locations may also be affected (e.g., by the change in the mode shapes). The fact that the sensor locations are inadequate means that the sensors will not provide signals that are optimally uncorrelated. To quantify the level of correlation, one can use the singular values of matrix $\mathbf{U}_{\text{aug}}^{\text{EIDV}}$. If all these singular values are of similar magnitude, then the signals are optimally uncorrelated. The smaller the ratio $\sigma_{\max}/\sigma_{\min}$ is, the more correlated the signals are (where $\sigma_{\min}$ and $\sigma_{\max}$ are the smallest

and the largest singular values). For example, consider that the HMMWV structure has geometrical parameters as the ones used to obtain the results shown in Fig. 4.6. The sensor locations shown in Fig. 4.6 for that structure lead to $\sigma_{\max}/\sigma_{\min} = 1.04$. In contrast, if one uses these same same sensor locations, but for a structure which has slightly different geometrical parameters (e.g., the parameters used to obtain the results in Fig. 4.8), then one obtains to $\sigma_{\max}/\sigma_{\min} = 1.58$. This latter set of singular values indicates that the locations which are best for the structure with the first set of structural parameter values are worse for the structure with the second set of structural parameter values. In general, sensors selected for one set of structural parameter values are not necessarily adequate for other structural parameter values. A statistically optimal choice for sensor locations has to be made to reach a compromise between signal correlation and robustness to parameter variability in the structure. PROMs are specifically designed to account for parameter variability, and hence enable such desirable statistical analyses, which in turn allow one to obtain the statistically robust/optimal sensor locations.

The structural variability considered in the numerical example is geometric (thickness variations). Nonetheless, the proposed method applies to a much larger class of variability, including material variability (such as variability in the modulus of elasticity, or other parameters of the material). From a structural dynamics standpoint these cases are treated the same way: as changes in the mass and stiffness matrices of the system. PROMs have been applied because they provide a fast solution for systems where such variability can be present and should be accounted for.

CHAPTER V

Novel Sensor Placement for Damage Identification in a Cracked Complex Structure with Structural Variability

5.1 Introduction

Robust techniques for sensor placement and damage detection are of current interest because of the increased need to reduce the time and the cost of examining the structural integrity of military ground vehicles and aircraft. To assess integrity, structural information must be obtained using a variety of sensors. Both the number and the locations of sensors are limited due to cost and accessibility constraints. There are many previous studies of sensor placement for structural health monitoring. Ansari [41] has implemented health monitoring strategies which require selection and placement of sensors suitable for measuring key parameters that influence the performance and health of civil structures. Flynn and Todd [42] have proposed a novel approach for optimal actuator and sensor placement for structural health monitoring. Krommer *et al.* [43] have investigated a sensor network composed of strain-type patch sensors with constant intensity designed to replace distributed strain-type sensors for monitoring beam-type structures.

Herein, a novel sensor placement technique is employed to find the optimal and minimal number of sensor locations for gathering modal information. The novel approach uses an algorithm similar to the effective independence distribution vector (EIDV) [44,45]. The

EIDV approach is designed for selecting locations for measuring physical mode shapes. The key idea of EIDV is to choose locations which make the measured partial eigenstructure as linearly independent as possible. Herein, the EIDV method is modified to select optimal sensor location for cracked structures. The information collected is then used to detect the crack length.

In addition to the need to determine the optimal locations for gathering structural information, predicting the dynamic response of complex structures is another important challenge. The number of degrees of freedom (DOFs) of complex structures are prohibitively large, and thus they are hard to use for solving inverse problems such as damage detection. To alleviate this problem, techniques have been developed recently to predict the dynamic response of complex structures with models employing a dramatically lower number of DOFs [6–10]. These advanced reduced order models (ROMs) are increasingly used for structural health monitoring because of the complexity of the structures of interest. One method for constructing ROMs is based on the fixed-interface Craig-Bampton component mode synthesis (CB-CMS) [7]. That well known approach is employed herein for a few portions of the model. Specifically CB-CMS is useful and applied only to the invariant components of overall/entire structures. A component is considered invariant if it does not have any geometrical or structural variations. However, the overall/entire structure can have such kinds of variations due to manufacturing or damage. If one attempts to use standard reduced order modeling techniques when parametric changes are applied by design or exist through damage, the finite element model has to be modified, and new ROMs have to be reconstructed to predict the structural vibration response. That is a very costly process computationally. Recently, design oriented ROMs have been developed to avoid such prohibitively expensive reanalyses of complex structures. These models are referred to as parametric reduced order models (PROMs). Initially, global PROMs have been de-

veloped [28, 29]. However, global PROMs are impractical because they require that one repeatedly solves many sample eigenproblems for the entire structure. Thus, component-mode-based PROMs [30] have been developed to adopt component normal modes and characteristic constraint modes as projection basis instead of global modes. However, constructing component-mode-based PROMs as done is also time consuming because the approach still requires the calculation of system-level (global) interface modes. Thus, Park [32] introduced truly component-level analysis for constructing PROMs, referred to as component-PROMs. However, in their approach, component-PROMs can be applied only to one component. Thus, the multiple-component PROMs (MC-PROMs) [35] have been developed by the authors and are adopted herein to allow complex structures to be divided into several, much simpler, substructures. Each substructure can have variability in characteristics such as geometric parameters (e.g. thickness) or material properties (e.g. Young's modulus).

In this work, PROM techniques employing CB-CMS and MC-PROMs are applied to analyze the vibration response of a cracked complex structure. Also, note that the cracked structure generates a nonlinear dynamic problem because of the nonlinear contact force between the crack surfaces. One approach to handle this nonlinear contact force is to use a hybrid frequency-time domain (HFT) method developed by Poudou and Pierre [36], Poudou [37], and Saito [40]. In that method, a forced response analysis is applied to determine the resonant frequencies of cracked structures. While powerful, that approach is computationally intensive, and difficult to use to predict resonant responses (due to the nonlinearity). Thus, an alternate approach (based on linear analyses) has been developed for predicting resonant frequencies. The alternate approach builds on earlier work on the bilinear frequency approximation (BFA) [39]. The resonant frequencies predicted by the generalized BFA have been shown to agree very well with those obtained using nonlinear

HFT analyses for applications such as cracked turbine bladed disks [65]. Herein, the concept of BFA is adopted together with the bilinear mode approximation (BMA) [66]. BMA is introduced to approximate the mode shapes of cracked structures. In addition, to reduce computational cost for BMA, ROM techniques based on CB-CMS and MC-PROMs are used. Finally, the bilinear mode shapes of cracked structures in the reduced order domain are used to estimate the crack length.

This paper provides an algorithm to detect the crack length in the complex structures with structural variations. A novel crack detection algorithm is obtained by using the bilinear mode shapes of cracked complex structure in the reduced order domain together with a method to select optimal sensor locations based on a modified EIDV algorithm. The technique to find optimal sensor locations is specifically designed for cases where the structure has structural variability and a crack. This technique is for estimating the size of the crack, not for finding the crack location. To apply this technique, knowledge of the hot spots in the structure is needed. Next, by using the algorithm proposed in this paper, the presence of the crack can be detected. Then, the proposed approach can be applied to estimate the size of the crack. However, herein, it is assumed that the presence and the location of the crack are known. Of course, detecting the size, location and presence of the crack are very important issues for structural health monitoring. These three features of cracks are all significant. Here, the focus is to estimate the size of the crack, not to find the location or the presence of the crack. An example application would be to monitor a crack located in ground vehicle component that requires partial teardown to inspect visually.

5.2 Bilinear Mode Approximation

In this section, the shapes of the resonant responses of a structure with a crack of various lengths are examined. When a structure has a crack, it also exhibits nonlinear dy-

namics. This dynamics is caused by the periodic opening and closing of the crack surface (which leads to a piece-wise linear dynamics). Hence, standard modal analyses cannot be directly employed. To address this challenge, a novel technique to characterize the spatial correlations among the vibration of various points within the structure has been developed. These correlations are akin to mode shapes, but they characterize the dynamics of the cracked (nonlinear) structure. This approach is based on the observation that, when the structure has a crack and vibrates at some (nonlinear) resonant frequency, two states can be identified: crack open and crack closed. These two states correspond to two shapes for the deformation of the structure at that frequency. Next, we assume that all the shapes the structure takes during its nonlinear vibration at a resonant frequency are linear combinations of these two shapes (open and closed at that resonant frequency). Furthermore, the open and closed shapes are assumed to be very similar to the shapes the structure would have if the crack surface were permanently open (i.e. penetration would be allowed) or permanently closed (with sliding occurring between DOFs within the crack surface). These linear modes can be easily computed by standard linear techniques. This novel approach is referred to as BMA, and complements BFA [39] originally developed for discrete low-dimensional systems and later generalized for cracked structures. The bilinear (BL) modes $\mathbf{\Phi}_{BL}$ can be expressed as

$$\mathbf{\Phi}_{BL} = \begin{bmatrix} \mathbf{\Phi}_{open} \\ \\ \mathbf{\Phi}_{closed} \end{bmatrix}, \tag{5.1}$$

where $\mathbf{\Phi}_{open}$ are the mode shapes of the structure with a permanently open crack (penetration allowed) and $\mathbf{\Phi}_{closed}$ are the mode shapes of the structure with a permanently closed crack (sliding allowed). Note that the assumptions made in this section for the bilinear approximation are not appropriate for the cases where the crack surface has intermediate contact, when the impact between crack surfaces is not negligible, or when the crack opens

and closes gradually [66].

5.3 Fixed-Interface Craig-Bampton Component Mode Synthesis (CB-CMS)

In this section, the well known fixed-interface Craig-Bampton CMS (CB-CMS) [7] method used to construct ROMs for healthy substructures is briefly reviewed. This approach is used to model only the substructures which do not have any structural variability. This modeling approach is used because it is very simple and computationally stable. Also, this technique can be exploited when modeling cracked structures by managing the geometric compatibility conditions between substructures.

To apply CB-CMS, the complex structure of interest is partitioned into substructures, and the DOFs of each substructure are further partitioned into active (A) DOFs on the interface, and omitted (O) DOFs in the interior. Then, the mass and stiffness matrices of the finite element model for a component i can be partitioned as follows

$$\mathbf{M}_i = \begin{bmatrix} \mathbf{m}_i^{AA} & \mathbf{m}_i^{AO} \\ \mathbf{m}_i^{OA} & \mathbf{m}_i^{OO} \end{bmatrix} \quad \text{and} \quad \mathbf{K}_i = \begin{bmatrix} \mathbf{k}_i^{AA} & \mathbf{k}_i^{AO} \\ \mathbf{k}_i^{OA} & \mathbf{k}_i^{OO} \end{bmatrix}.$$

Next, the physical coordinates are projected onto the generalized coordinates. In this context, the generalized coordinates are a set of coordinates representing the amplitudes of a selected set of fixed-interface component-level normal modes $\mathbf{\Phi}_i^N$ (indicated by the superscript N) and the amplitudes of the full set of static constraint modes $\mathbf{\Psi}_i^C = -\mathbf{k}_i^{OO^{-1}}\mathbf{k}_i^{OA}$ (indicated by the superscript C). The transformed mass and stiffness matrices for component i can be expressed as

$$\hat{\mathbf{M}}_i = \begin{bmatrix} \mathbf{m}_i^{C} & \mathbf{m}_i^{CN} \\ \mathbf{m}_i^{NC} & \mathbf{m}_i^{NN} \end{bmatrix} \quad \text{and} \quad \hat{\mathbf{K}}_i = \begin{bmatrix} \mathbf{k}_i^{C} & \mathbf{k}_i^{CN} \\ \mathbf{k}_i^{NC} & \mathbf{k}_i^{NN} \end{bmatrix}. \tag{5.2}$$

To model the dynamics of cracked structures and to apply BMA, the partitioning of the

structure is done such that all crack surfaces are along interfaces between adjacent substructures. That way, the crack model can be obtained by simply managing the geometric compatibility conditions. To apply geometric compatibility conditions in Eq. (5.2), the C DOFs which represent interface DOFs are further divided into constraint DOFs (superscript CC) and free DOFs (superscript FF). For the open crack case, the DOFs between the crack surfaces are completely free, which means that those DOFs are allowed to inter-penetrate. These DOFs on the crack surfaces are free DOFs (superscript FF) in Eq. (5.3). For the closed crack case, sliding boundary conditions are applied at the DOFs on the crack surfaces. Hence, the DOFs on the crack interface can slide, but they are not allowed to inter-penetrate. The constrained DOFs which are not allowed to inter-penetrate are denoted by superscript CC in Eq. (5.3). Using these two kinds of geometric compatibility conditions, the mode shapes of a cracked structure with an open crack and separately a closed crack are obtained through two separate linear analyses. Thus, if component i has a crack surface, the component-level mass and stiffness matrices are partitioned as [35]

$$\hat{\mathbf{M}}_i = \begin{bmatrix} \mathbf{m}_i^{CC} & \mathbf{m}_i^{CF} & \mathbf{m}_i^{CCN} \\ \mathbf{m}_i^{FC} & \mathbf{m}_i^{FF} & \mathbf{m}_i^{FFN} \\ \mathbf{m}_i^{NCC} & \mathbf{m}_i^{NFF} & \mathbf{m}_i^{NN} \end{bmatrix}, \text{ and } \hat{\mathbf{K}}_i = \begin{bmatrix} \mathbf{k}_i^{CC} & \mathbf{k}_i^{CF} & \mathbf{k}_i^{CCN} \\ \mathbf{k}_i^{FC} & \mathbf{k}_i^{FF} & \mathbf{k}_i^{FFN} \\ \mathbf{k}_i^{NCC} & \mathbf{k}_i^{NFF} & \mathbf{k}_i^{NN} \end{bmatrix}. \quad (5.3)$$

Since all crack surfaces are at interfaces between components, all boundary DOFs are active DOFs. The geometric compatibility conditions used to assemble every substructure are lastly applied only to the DOFs marked as CC in Eq. (5.3).

5.4 Multiple-Component Parametric Reduced-Order Models

MC-PROMs [35] are adopted to manage the substructures with parameter variability. One important advantage of MC-PROMs is that the finite element mesh of the nominal structure does not need to be modified despite parameter variability. That is because the

mass and stiffness matrices are parameterized by using Taylor series within an upper and a lower limit for the parameterization. For example, for a linear thin plate element, the modification of the stiffness matrix due to variations in the thickness of the plate can be accurately represented by a Taylor series up to third order, while the mass matrix can be approximated by a Taylor series up to first order. Consider a parameter p. The first and the third order Taylor series approximations about the nominal parameter value p_0 can be expressed as follows [35]

$$\begin{aligned} \mathbf{M}_i(p) &\approx \mathbf{M}_i(p_0) + \frac{\partial \mathbf{M}_i}{\partial p}(p-p_0), \\ \mathbf{K}_i(p) &\approx \mathbf{K}_i(p_0) + \frac{\partial \mathbf{K}_i}{\partial p}(p-p_0) \\ &\quad + \frac{1}{2}\frac{\partial^2 \mathbf{K}_i}{\partial p^2}(p-p_0)^2 + \frac{1}{6}\frac{\partial^3 \mathbf{K}_i}{\partial p^3}(p-p_0)^3. \end{aligned} \tag{5.4}$$

Computationally, the partial derivatives in Eq. (5.4) are approximated by using finite differences (for a small parameter variation Δp). For example,

$$\begin{aligned} \mathbf{M}^1_{FD} &= \frac{\partial \mathbf{M}_i}{\partial p} \approx \frac{\mathbf{M}_i(p_0+\Delta p) - \mathbf{M}_i(p_0)}{\Delta p}, \\ \mathbf{K}^1_{FD} &= \frac{\partial \mathbf{K}_i}{\partial p} \approx \frac{\mathbf{K}_i(p_0+\Delta p) - \mathbf{K}_i(p_0)}{\Delta p}, \\ \mathbf{K}^2_{FD} &= \frac{\partial^2 \mathbf{K}_i}{\partial p^2} \approx \frac{\mathbf{K}_i(p_0+2\Delta p) - 2\mathbf{K}_i(p_0+\Delta p) + \mathbf{K}_i(p_0)}{\Delta p^2}. \end{aligned} \tag{5.5}$$

Following closely the approach in Hong *et al.* [35], the parameterized component matrices can be obtained by substituting Eq. (5.5) into Eq. (5.4) to obtain

$$\begin{aligned} \mathbf{M}_i(p) &\approx \mathbf{M}_i(p_0) + \mathbf{M}^1_{FD}(p-p_0), \\ \mathbf{K}_i(p) &\approx \mathbf{K}_i(p_0) + \mathbf{K}^1_{FD}(p-p_0) \\ &\quad + \frac{1}{2}\mathbf{K}^2_{FD}(p-p_0)^2 + \frac{1}{6}\mathbf{K}^3_{FD}(p-p_0)^3, \end{aligned} \tag{5.6}$$

where $\mathbf{K}^3_{FD} = \frac{\partial^3 \mathbf{K}_i}{\partial p^3}$.

Similar to the previous section, the concept of CB-CMS is used to construct an appropriate transformation matrix for converting physical coordinates into generalized coordinates. In the standard CB-CMS formulation, the fixed-interface normal modes $\mathbf{\Phi}_i^N$ and static constraint modes $\mathbf{\Psi}_i^C$ of the nominal structure are used to construct the transformation matrix. However, for MC-PROMs, the mass and stiffness matrices are parameterized. Thus, the transformation matrix is also constructed for all configurations in the parameter space of the corresponding component. This approach is distinct from standard CB-CMS. Herein, the component-level modal basis $\hat{\mathbf{\Phi}}_i$ for the i^{th} component can be expressed as

$$\hat{\mathbf{\Phi}}_i = \begin{bmatrix} \mathbf{I} & \mathbf{I} & \mathbf{0} \\ \mathbf{\Psi}_i^0 & \mathbf{\Psi}_i^U & \mathbf{\Phi}_i^{aug} \end{bmatrix}, \tag{5.7}$$

where $\mathbf{\Phi}_i^{aug}$ is referred to as the matrix of augmented fixed-interface normal modes

$$\mathbf{\Phi}_i^{aug} = \begin{bmatrix} \mathbf{\Phi}_i^0 & \mathbf{\Phi}_i^1 & \mathbf{\Phi}_i^2 & \mathbf{\Phi}_i^3 \end{bmatrix}, \tag{5.8}$$

and the superscript 0 indicates the nominal parameter values, while the superscript U, 1, 2 and 3 indicate quantities computed for perturbed parameter values. These perturbed parameter values can be same values as the ones used in Eq. (5.5) to approximate the mass and stiffness matrices. Vectors $\mathbf{\Phi}_i$ and $\mathbf{\Psi}_i$ in Eq. (5.7) represent fixed-interface normal modes and static constraint modes.

A third order Taylor series is used to represent the parameterized stiffness matrix. Hence, the fixed-interface normal modes for three perturbed structures are computed to form a transformation matrix. Note that, in general, taken all together, the modes in $\mathbf{\Phi}_i^{aug}$ are not orthogonal. For numerical stability, an orthogonal basis for the space spanned by these modes is used. To that aim, the left singular vectors of $\mathbf{\Phi}_i^{aug}$ are computed, and the left singular vectors $\mathbf{U}_i$ corresponding to singular values larger than 0.01% of the maximum singular value are selected. Next, $\mathbf{U}_i$ is used to construct a transformation matrix

(instead of the augmented fixed-interface normal modes $\mathbf{\Phi}_i^{aug}$). The final transformation matrix can be expressed as

$$\hat{\mathbf{\Phi}}_i = \begin{bmatrix} \mathbf{I} & \mathbf{I} & \mathbf{0} \\ \mathbf{\Psi}_i^0 & \mathbf{\Psi}_i^U & \mathbf{U}_i \end{bmatrix}. \tag{5.9}$$

Using Eq. (5.9) into Eq. (5.6), the physical coordinates are transformed into generalized coordinates along the collected set of modes $\hat{\mathbf{\Phi}}_i$ for the i^{th} component. The transformed mass and stiffness matrices can be expressed as [35]

$$\begin{aligned} \hat{\mathbf{M}}_i(p) &\approx \hat{\mathbf{\Phi}}_i^T \mathbf{M}_i(p_0)\hat{\mathbf{\Phi}}_i + \hat{\mathbf{\Phi}}_i^T \mathbf{M}_{FD}^1 \hat{\mathbf{\Phi}}_i(p-p_0), \\ \hat{\mathbf{K}}_i(p) &\approx \hat{\mathbf{\Phi}}_i^T \mathbf{K}_i(p_0)\hat{\mathbf{\Phi}}_i + \hat{\mathbf{\Phi}}_i^T \mathbf{K}_{FD}^1 \hat{\mathbf{\Phi}}_i(p-p_0) \\ &\quad + \frac{1}{2}\hat{\mathbf{\Phi}}_i^T \mathbf{K}_{FD}^2 \hat{\mathbf{\Phi}}_i(p-p_0)^2 + \frac{1}{6}\hat{\mathbf{\Phi}}_i^T \mathbf{K}_{FD}^3 \hat{\mathbf{\Phi}}_i(p-p_0)^3. \end{aligned}$$

The modal bases used in MC-PROMs and CB-CMS consist of internal and interface DOFs for each substructure. Thus, the mass and stiffness matrices for the i^{th} component used for MC-PROMs can be partitioned as follows

$$\begin{aligned} \mathbf{M}_i^{PROM} &= \begin{bmatrix} \mathbf{m}_i^{C_{00}} & \mathbf{m}_i^{C_{0U}} & \mathbf{m}_i^{CN_{00}} \\ \mathbf{m}_i^{C_{U0}} & \mathbf{m}_i^{C_{UU}} & \mathbf{m}_i^{CN_{UU}} \\ \mathbf{m}_i^{NC_{00}} & \mathbf{m}_i^{NC_{UU}} & \mathbf{m}_i^{N_d} \end{bmatrix} \text{ and} \\ \mathbf{K}_i^{PROM} &= \begin{bmatrix} \mathbf{k}_i^{C_{00}} & \mathbf{k}_i^{C_{0U}} & \mathbf{k}_i^{CN_{00}} \\ \mathbf{k}_i^{C_{U0}} & \mathbf{k}_i^{C_{UU}} & \mathbf{k}_i^{CN_{UU}} \\ \mathbf{k}_i^{NC_{00}} & \mathbf{k}_i^{NC_{UU}} & \mathbf{k}_i^{N_d} \end{bmatrix}, \end{aligned} \tag{5.10}$$

where superscript N_d refers to the interior generalized DOFs used in the MC-PROMs approach.

Similar to CB-CMS, the interface DOFs (C) are also further divided into constrained DOFs (superscript (CC)) and free DOFs (superscript FF) to apply open and sliding boundary conditions for BMA, as done in Eq. (5.3). Thus, the interface DOFs marked

as C can also be divided into CC and FF DOFs. Then, the MC-PROMs mass and stiffness matrices can be partitioned as [35]

$$\mathbf{M}_i^{PROM} = \begin{bmatrix} \mathbf{m}_i^{CC_{00}} & \mathbf{m}_i^{CF_{00}} & \mathbf{m}_i^{CC_{0U}} & \mathbf{m}_i^{CF_{0U}} & \mathbf{m}_i^{CCN_{00}} \\ \mathbf{m}_i^{FC_{00}} & \mathbf{m}_i^{FF_{00}} & \mathbf{m}_i^{FC_{0U}} & \mathbf{m}_i^{FF_{0U}} & \mathbf{m}_i^{FFN_{00}} \\ \mathbf{m}_i^{CC_{U0}} & \mathbf{m}_i^{CF_{U0}} & \mathbf{m}_i^{CC_{UU}} & \mathbf{m}_i^{CF_{UU}} & \mathbf{m}_i^{CCN_{UU}} \\ \mathbf{m}_i^{FC_{U0}} & \mathbf{m}_i^{FF_{U0}} & \mathbf{m}_i^{FC_{UU}} & \mathbf{m}_i^{FF_{UU}} & \mathbf{m}_i^{FFN_{UU}} \\ \mathbf{m}_i^{NCC_{00}} & \mathbf{m}_i^{NFF_{00}} & \mathbf{m}_i^{NCC_{UU}} & \mathbf{m}_i^{NFF_{UU}} & \mathbf{m}_i^{N_d} \end{bmatrix},$$

$$\mathbf{K}_i^{PROM} = \begin{bmatrix} \mathbf{k}_i^{CC_{00}} & \mathbf{k}_i^{CF_{00}} & \mathbf{k}_i^{CC_{0U}} & \mathbf{k}_i^{CF_{0U}} & \mathbf{k}_i^{CCN_{00}} \\ \mathbf{k}_i^{FC_{00}} & \mathbf{k}_i^{FF_{00}} & \mathbf{k}_i^{FC_{0U}} & \mathbf{k}_i^{FF_{0U}} & \mathbf{k}_i^{FFN_{00}} \\ \mathbf{k}_i^{CC_{U0}} & \mathbf{k}_i^{CF_{U0}} & \mathbf{k}_i^{CC_{UU}} & \mathbf{k}_i^{CF_{UU}} & \mathbf{k}_i^{CCN_{UU}} \\ \mathbf{k}_i^{FC_{U0}} & \mathbf{k}_i^{FF_{U0}} & \mathbf{k}_i^{FC_{UU}} & \mathbf{k}_i^{FF_{UU}} & \mathbf{k}_i^{FFN_{UU}} \\ \mathbf{k}_i^{NCC_{00}} & \mathbf{k}_i^{NFF_{00}} & \mathbf{k}_i^{NCC_{UU}} & \mathbf{k}_i^{NFF_{UU}} & \mathbf{k}_i^{N_d} \end{bmatrix}. \quad (5.11)$$

The geometric compatibility conditions for the cracked structure are applied the same way as for the components modeled with the standard CB-CMS.

Numerical results have shown the efficiency of MC-PROMs. The computational time required by MC-PROMs for the reanalysis is approximately 100 times shorter than the time required by full-order model analyses [35]

5.5 Generalized Modal Assurance Criterion (MAC)

Some of the shapes of the resonant response of the healthy and the cracked structures are very similar, and some are not. For example, when the resonant response is not large near the crack, the response of the cracked structure is very similar to the response of the healthy structure. Such a resonant response is not very good for detecting the presence and length of a crack. For detection, monitoring the modes most sensitive to the crack is a better choice. Thus, the most sensitive bilinear (BL) modes are identified first. For that,

a novel modal assurance criterion (MAC) [67, 68] has been developed and used to obtain the generalized $\mathbf{MAC}$ matrix between the BL modes for the healthy and the cracked structures. The new MAC needs the BL mass matrix obtained separately using ROMs for the open and closed crack vibration cases because the mode shapes for the open and closed states are mass normalized, and their sizes are different due to the distinct geometric compatibility conditions. The BL mass matrix can be expressed as

$$\mathbf{M}_{BL} = \begin{bmatrix} \mathbf{M}_{ROM}^{open} & \mathbf{0} \\ \mathbf{0} & \mathbf{M}_{ROM}^{closed} \end{bmatrix}, \tag{5.12}$$

where the two mass matrices for open and closed states are obtained from ROMs. Herein, ROMs are obtained by using CB-CMS and MC-PROMs. This BL mass matrix is used together with the BL modes to define a new MAC as

$$\mathbf{MAC}_{ij} = \frac{[(\mathbf{\Phi}_{BL,i}^{h})^T \mathbf{M}_{BL} (\mathbf{\Phi}_{BL,j}^{d})]^2}{[(\mathbf{\Phi}_{BL,i}^{h})^T \mathbf{M}_{BL} (\mathbf{\Phi}_{BL,i}^{h})][(\mathbf{\Phi}_{BL,j}^{d})^T \mathbf{M}_{BL} (\mathbf{\Phi}_{BL,j}^{d})]}, \tag{5.13}$$

where the subscripts i and j indicate the i^{th} and j^{th} modes, and the BL mode shapes for the healthy structure (indicated by the superscript h) are defined as in Eq. (5.1) but for a zero crack length, while the BL modes for a non-zero crack are indicated by the superscript d. The value $\mathbf{MAC}_{ij}$ reflects how distinct is the i^{th} healthy BL mode from the j^{th} cracked BL mode. Note that the $\mathbf{MAC}$ matrix can be computed for structures with different crack lengths. The (diagonal) entries that correspond to non-sensitive BL modes are close to 1.0 because the BL modes are normalized by the BL mass matrix. A specific example of selecting sensitive modes is showed in the next sections.

5.6 Detection Algorithm for Crack Length

The $\mathbf{MAC}$ matrix in Eq. (5.13) quantifies the sensitivity of the bilinear (BL) modes to the crack. Accordingly, a frequency range of interest is defined such that it includes

the most sensitive BL modes. Based on this frequency range of interest, a new sensor placement algorithm is applied to identify crack lengths. The procedure to estimate the length of a crack can be summarized as follows.

(1) The mode shapes of the healthy and the cracked structures (with up to 3 crack lengths) are obtained using ROMs (using methods such as CB-CMS and MC-PROMs).

(2) The candidate measurement DOFs are used to truncate the the full BL modes. The resulting $partial$ BL modes for the healthy and the cracked structures are denoted by $\mathbf{\Phi}^h_{BL,i}$ and $\mathbf{\Phi}^d_{BL,i}$. Each partial BL mode is normalized as follows

$$\hat{\mathbf{\Phi}}^{\,h}_{BL,i} = \frac{\mathbf{\Phi}^h_{BL,i}}{\parallel \mathbf{\Phi}^h_{BL,i} \parallel_2} \quad \text{and} \quad \hat{\mathbf{\Phi}}^{\,d}_{BL,i} = \frac{\mathbf{\Phi}^d_{BL,i}}{\parallel \mathbf{\Phi}^d_{BL,i} \parallel_2}. \tag{5.14}$$

(3) The normalized (partial) BL modes are assumed to depend on the crack length (denoted by d) approximately as follows

$$\hat{\mathbf{\Phi}}^{\,d}_{BL,i} = \hat{\mathbf{\Phi}}^{\,h}_{BL,i} + \delta\hat{\mathbf{\Phi}}^{\,d_a}_{BL,i} \cdot d + \delta\hat{\mathbf{\Phi}}^{\,d_b}_{BL,i} \cdot d^2 + \delta\hat{\mathbf{\Phi}}^{\,d_c}_{BL,i} \cdot d^3. \tag{5.15}$$

(4) The variations in the (partial) mode shapes $\delta\hat{\mathbf{\Phi}}^{\,d_a}_{BL,i}$, $\delta\hat{\mathbf{\Phi}}^{\,d_b}_{BL,i}$ and $\delta\hat{\mathbf{\Phi}}^{\,d_c}_{BL,i}$ are computed using 3 separate ROMs for the same structure but with 3 distinct crack lengths. The dependence of the partial BL modes on the crack length in Eq. (5.15) can be used for the 3 lengths of the crack d_a, d_b, and d_c to obtain

$$\begin{aligned}
\hat{\mathbf{\Phi}}^{\,d_a}_{BL,i} &= \hat{\mathbf{\Phi}}^{\,h}_{BL,i} + \delta\hat{\mathbf{\Phi}}^{\,d_a}_{BL,i} \cdot d_a + \delta\hat{\mathbf{\Phi}}^{\,d_b}_{BL,i} \cdot d_a^2 + \delta\hat{\mathbf{\Phi}}^{\,d_c}_{BL,i} \cdot d_a^3, \\
\hat{\mathbf{\Phi}}^{\,d_b}_{BL,i} &= \hat{\mathbf{\Phi}}^{\,h}_{BL,i} + \delta\hat{\mathbf{\Phi}}^{\,d_a}_{BL,i} \cdot d_b + \delta\hat{\mathbf{\Phi}}^{\,d_b}_{BL,i} \cdot d_b^2 + \delta\hat{\mathbf{\Phi}}^{\,d_c}_{BL,i} \cdot d_b^3, \\
\hat{\mathbf{\Phi}}^{\,d_c}_{BL,i} &= \hat{\mathbf{\Phi}}^{\,h}_{BL,i} + \delta\hat{\mathbf{\Phi}}^{\,d_a}_{BL,i} \cdot d_c + \delta\hat{\mathbf{\Phi}}^{\,d_b}_{BL,i} \cdot d_c^2 + \delta\hat{\mathbf{\Phi}}^{\,d_c}_{BL,i} \cdot d_c^3.
\end{aligned} \tag{5.16}$$

Rearranging Eq. (5.16), one obtains

$$\begin{aligned}
&\begin{bmatrix} \vdots & \vdots & \vdots \\ \hat{\mathbf{\Phi}}^{d_a}_{BL,i} - \hat{\mathbf{\Phi}}^{h}_{BL,i} & \hat{\mathbf{\Phi}}^{d_b}_{BL,i} - \hat{\mathbf{\Phi}}^{h}_{BL,i} & \hat{\mathbf{\Phi}}^{d_c}_{BL,i} - \hat{\mathbf{\Phi}}^{h}_{BL,i} \\ \vdots & \vdots & \vdots \end{bmatrix} \\
&= \begin{bmatrix} \vdots & \vdots & \vdots \\ \delta\hat{\mathbf{\Phi}}^{d_a}_{BL,i} & \delta\hat{\mathbf{\Phi}}^{d_b}_{BL,i} & \delta\hat{\mathbf{\Phi}}^{d_c}_{BL,i} \\ \vdots & \vdots & \vdots \end{bmatrix} \begin{bmatrix} d_a & d_b & d_c \\ d_a^2 & d_b^2 & d_c^2 \\ d_a^3 & d_b^3 & d_c^3 \end{bmatrix} \\
&= \delta\hat{\mathbf{\Phi}}_{BL,i} \begin{bmatrix} d_a & d_b & d_c \\ d_a^2 & d_b^2 & d_c^2 \\ d_a^3 & d_b^3 & d_c^3 \end{bmatrix},
\end{aligned} \tag{5.17}$$

where $\delta\hat{\mathbf{\Phi}}_{BL,i}$ is referred to as the BL mode variation matrix (for mode i). For example, we consider the structure with $d_a = 5\%$, $d_b = 7\%$ and $d_c = 10\%$ crack lengths separately.

(5) Once, $\delta\hat{\mathbf{\Phi}}^{d_a}_{BL,i}$, $\delta\hat{\mathbf{\Phi}}^{d_b}_{BL,i}$ and $\delta\hat{\mathbf{\Phi}}^{d_c}_{BL,i}$ are obtained, they can be used into Eq. (5.15) to identify the crack length. Specifically, one measures a partial BL mode $\hat{\mathbf{\Phi}}^{d}_{i}$ and uses Eq. (5.15) to determine d. For each mode of index i, a value d_i is obtained as an estimate for the crack length. Note that Eq. (5.15) can be interpreted as a vector equation for a scalar unknown (d). To solve this vector equation, Eq. (5.15) is projected along $(\hat{\mathbf{\Phi}}^{d}_{BL,i} - \hat{\mathbf{\Phi}}^{h}_{BL,i})$.

The algorithm requires the measurement of one or a few BL modes of the cracked structure. These modes can be measured by separating physical measurements into two groups. One group corresponds to maximum positive deformations in a given direction, whereas the second group represents maximum (in absolute value) negative deformations. The positive measurements are used to obtain one of the components of each BL mode

(e.g., the open crack linear mode). The negative measurements are used to obtain the other component (e.g., the closed crack linear mode).

To apply this algorithm and to detect the size of the crack as precisely as possible, it is best if the crack location is known. Nonetheless, the existence of the crack can be detected by this technique also. In Eq. (5.15), the bilinear mode variation vectors $\delta\hat{\mathbf{\Phi}}^{d_a}_{BL,i}$, $\delta\hat{\mathbf{\Phi}}^{d_b}_{BL,i}$ and $\delta\hat{\mathbf{\Phi}}^{d_c}_{BL,i}$ can be calculated separately for various possible/expected cracks at specific locations (hot spots). Next, these mode variation vectors can be used to detect the presence of a crack as follows. If a crack is not present in the structure, then the i^{th} measured bilinear mode shapes of the healthy and the cracked structures, $\hat{\mathbf{\Phi}}^{h}_{BL,i}$ and $\hat{\mathbf{\Phi}}^{d}_{BL,i}$, are the same. Then, the variable d in Eq. (5.15) is zero. In contrast, when a crack is present in the structure, $\hat{\mathbf{\Phi}}^{h}_{BL,i}$ and $\hat{\mathbf{\Phi}}^{d}_{BL,i}$ are not the same, and the variable d is not zero. A non-zero value for d indicates that a crack is present at the specific location where the mode variation vectors were computed. Nonetheless, when d is not zero, its value is not precisely the length of the crack. To $accurately$ identify the size of the crack, its location has to be known.

The polynomial dependence of $\hat{\mathbf{\Phi}}^{h}_{BL,i}$ on the crack length d described in Eq. (5.15) is an appropriate functional dependence for small cracks. To construct the bilinear modal matrix, two types of eigenvectors of the cracked structure are used. These eigenvectors are computed from the mass and stiffness matrices for two states (open and closed). For the case of small cracks, the mass and stiffness matrices vary smoothly as the crack increases in size. Hence, the polynomial dependence is expected to be reasonable for small cracks.

Using this algorithm, the length of a crack can be estimated by using all candidate measurement DOFs (locations). However, this total number of candidate measurement DOFs is typically too large to instrument in a practical case. Thus, a new sensor placement algorithm was developed based on the EIDV algorithm as discussed in the next section. This

placement algorithm is designed to identify the minimum measurement DOFs (locations) needed to identify the length of the crack.

5.7 Modified Effective Independence Distribution Vector (EIDV) Algorithm

In a practical implementation of the proposed approach for structural inspection or damage detection, partial information about the bilinear (BL) modes has to be obtained through measurements. To address that challenge, an algorithm for establishing the minimal and optimal locations to be measured or instrumented with sensors has been developed. This algorithm is a derivative of the EIDV method [45]. Generally, the EIDV method requires only a portion of the modal matrix of a structure. This portion corresponds to the mode shapes of a structure (in a frequency range of interest allocated based on the generalized MAC discussed in the previous section) and to a set of candidate DOFs. The partial modal matrix is used to compute a Fisher (information) matrix which, in turn, allows the computation of an effective independence distribution vector. This vector identifies the DOFs that are best to measure in terms of ensuring the linear independence of the measurements. To apply EIDV, the augmented bilinear modal matrix $\mathbf{\Phi}_{aug}^{EIDV}$ of the cracked structure is formed instead of real mode shapes of the structure. $\mathbf{\Phi}_{aug}^{EIDV}$ is formed by grouping BL modes for the healthy structure (without a crack) $\hat{\mathbf{\Phi}}_{BL}^{h}$ and the three mode variation vectors $\delta\hat{\mathbf{\Phi}}_{BL,i}^{d_a}$, $\delta\hat{\mathbf{\Phi}}_{BL,i}^{d_b}$, and $\delta\hat{\mathbf{\Phi}}_{BL,i}^{d_c}$ which are obtained from Eq. (5.17). The matrix $\hat{\mathbf{\Phi}}_{BL}^{h}$ and all mode variation vectors in the frequency range of interest are assembled as follows

$$\mathbf{\Phi}_{aug}^{EIDV} = [\ \hat{\mathbf{\Phi}}_{BL}^{h}\ \ \delta\hat{\mathbf{\Phi}}_{BL,1}^{d_a}\ \ \delta\hat{\mathbf{\Phi}}_{BL,1}^{d_b}\ \ \delta\hat{\mathbf{\Phi}}_{BL,1}^{d_c}\ \ \cdots\ \ \delta\hat{\mathbf{\Phi}}_{BL,i}^{d_a}\ \ \delta\hat{\mathbf{\Phi}}_{BL,i}^{d_b}\ \ \delta\hat{\mathbf{\Phi}}_{BL,i}^{d_c}\ \ \cdots\ ]. \quad (5.18)$$

The sensors used in a measurement must be sufficient in number and placed optimally for measuring the modes of interest for the structure with an unknown crack length. Hence,

one must ensure that the sensors are placed optimally despite the fact that not all vectors $\delta\hat{\mathbf{\Phi}}^{d_a}_{BL,i}$, $\delta\hat{\mathbf{\Phi}}^{d_b}_{BL,i}$, and $\delta\hat{\mathbf{\Phi}}^{d_c}_{BL,i}$ are necessarily linearly independent. Hence, the EIDV methodology was generalized. A subset of the left singular vectors $\mathbf{U}^{EIDV}_{aug}$ of $\mathbf{\Phi}^{EIDV}_{aug}$ is used instead of the full augmented modal matrix. To select this subset, the singular values of $\mathbf{\Phi}^{EIDV}_{aug}$ are computed, and the left vectors corresponding to the largest singular values are selected. This process is similar to the one used in Eq. (5.8) for constructing PROMs. Using the resulting matrix $\mathbf{U}^{EIDV}_{aug}$, the generalized EIDV algorithm for establishing locations for sensor placement can be summarized as follows.

(1) Calculate the BL modes for the healthy structure and three mode variation vectors with all candidate measurement locations.

(2) Construct the augmented BL modal matrix $\mathbf{\Phi}^{EIDV}_{aug}$ as given in Eq. (5.18) in a frequency range of interest based on the $\mathbf{MAC}$ in Eq. (5.13).

(3) Apply singular value decomposition, and obtain the left singular vectors of $\mathbf{\Phi}^{EIDV}_{aug}$. Select the singular vectors $\mathbf{U}^{EIDV}_{aug}$ corresponding to the largest singular values.

(4) Calculate the Fisher information matrix given by $\mathbf{A} = \mathbf{U}^{EIDV^T}_{aug}\mathbf{U}^{EIDV}_{aug}$.

(5) Calculate the effective independence distribution vector, defined as the diagonal of matrix $\mathbf{E} = \mathbf{U}^{EIDV}_{aug}\mathbf{A}^{-1}\mathbf{U}^{EIDV^T}_{aug}$.

The number of significant or nontrivial singular values of $\mathbf{\Phi}^{EIDV}_{aug}$ are indicative of the number of sensors needed for identifying the crack length. After obtaining the optimal number of measurement locations, the crack detection algorithm is implemented to detect the crack length using only the optimal number of DOFs identified based on generalized EIDV algorithm.

5.8 Numerical Results

5.8.1 High mobility multipurpose wheeled vehicle model with shell-type elements

In this section, we demonstrate the new PROM and EIDV-based approach and the crack detection algorithm presented above for a realistic vehicle model. The structure is a high mobility multipurpose wheeled vehicle (HMMWV) base frame with a crack. The finite element model of the HMMWV frame is a conventional shell element model. Fig. 5.1 shows this model along with the candidate measurement locations. Fig. 5.2 shows each substructure of the HMMWV frame used to construct ROMs. The reinforcement frames in the rear and the front are attached to the leftrails. These reinforcement frames are considered to have thickness variations. Tab. 5.1 shows the thickness variations in the reinforcement frames. The cross-member is considered to have a crack, as shown in Fig. 5.3. The crack length varies (across the cross-member component) from 3.03% to 36.36%. The CB-CMS method is applied for the remainder of the structure (the part of the structure which does not have any thickness variations or cracks). The MC-PROMs method and the BMA approach are implemented for the substructures with thickness variations and for approximate bilinear (BL) modeling of the response of the cracked HMMWV frame. Note that the HMMWV model exhibits a particular behavior because it is constructed of shell ele-

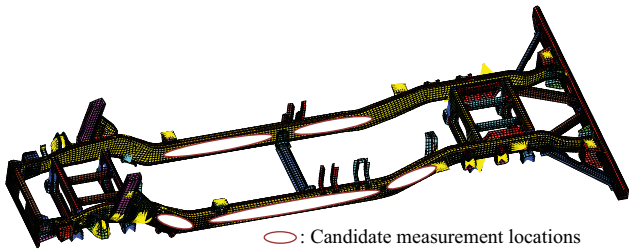

Figure 5.1: Finite element model for a high mobility multipurpose wheeled vehicle (HMMWV) frame

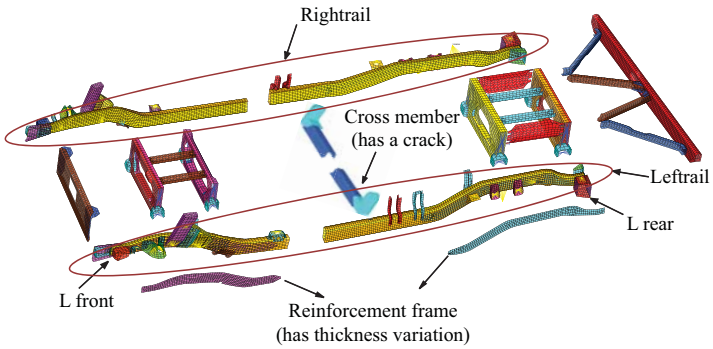

Figure 5.2: Substructuring of the high mobility multipurpose wheeled vehicle (HMMWV) frame

Table 5.1: Thickness variations in substructures

Substructure	Thickness variation
L_{rear}	3.0378 mm $\rightarrow 4.6268$ mm
L_{front}	3.0378 mm $\rightarrow 5.3838$ mm

ments (with very small thickness). Specifically, the deformation of the structure is always similar to an open crack motion and never similar to a closed crack vibration. Thus, only open crack modes were needed in this computational example. Prior to calculating the BL mode variation matrix $\delta\hat{\mathbf{\Phi}}_{BL,i}$ for mode i, the most sensitive BL mode is identified by using the generalized $\mathbf{MAC}$ matrix. Fig. 5.4 shows the $\mathbf{MAC}$ matrices computed between the healthy and the cracked structures with 30.30% and 36.36% crack length. For these 30.30% and 36.36% crack structures, the 30^{th} mode is the most sensitive compared to the healthy structure. Thus, $i = 30$ and the 30^{th} mode of the healthy and cracked structures are used to identify the crack length. Fig. 5.5 and Fig. 5.6 show that the 30^{th} mode shapes of the healthy and the 36.36% cracked HMMWV models are significantly different. Thus, the crack affects the 30^{th} mode which is hence the best mode to use in the crack

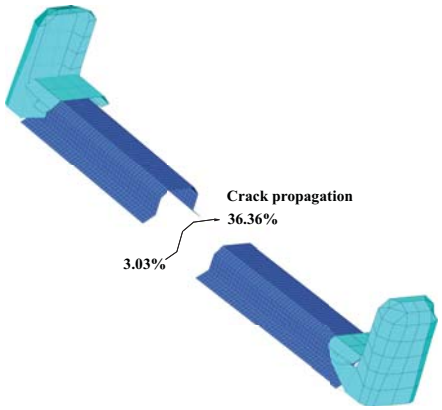

Figure 5.3: Substructure for the cracked cross-member

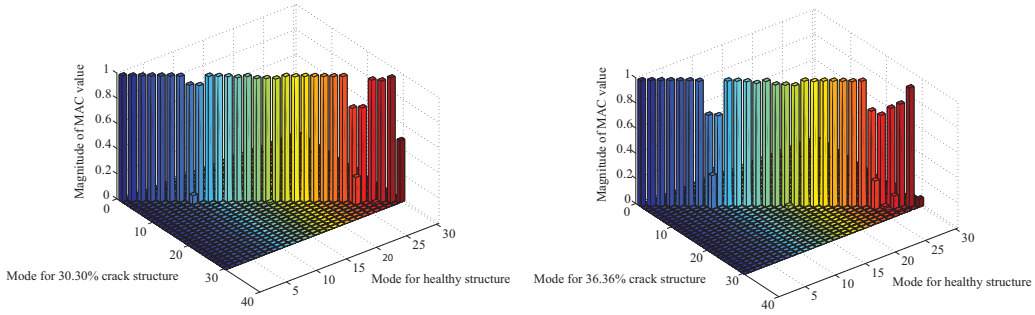

Figure 5.4: $\mathbf{MAC}$ between models for the healthy structure and the structure with a 30.30% crack and a 36.36% crack

detection algorithm. The crack detection algorithm is applied to calculate the BL mode variation matrix $\delta\hat{\mathbf{\Phi}}_{BL,30}$ for mode shapes of the structure with three distinct crack lengths: $d_a = 15.15\%$, $d_b = 21.21\%$, and $d_c = 30.30\%$.

Next, the generalized EIDV algorithm is applied to obtain the optimal sensor locations. Fig. 5.7 shows the best four sensor locations to capture the 30^{th} mode and identify the crack length. The BL mode shapes of the cracked structure are considered to be measured only at those four locations. Using those measurements, the crack length is detected

Figure 5.5: The 30^{th} mode shape of the healthy high mobility multipurpose wheeled vehicle (HMMWV) frame

Figure 5.6: The 30^{th} mode shape of the high mobility multipurpose wheeled vehicle (HMMWV) frame with a 36.36% crack

using Eq. (5.15). Thus, herein the assumption is that the BL mode shape $\hat{\mathbf{\Phi}}^{d}_{BL,30}$ is well approximated by real open crack mode shapes of the structure. In Eq. (5.15), d is a variable for crack estimation. Note that only $\hat{\mathbf{\Phi}}^{d}_{BL,30}$ has to be measured. Vectors $\hat{\mathbf{\Phi}}^{h}_{BL,30}$, $\delta\hat{\mathbf{\Phi}}^{d_a}_{BL,30}$, $\delta\hat{\mathbf{\Phi}}^{d_b}_{BL,30}$ and $\delta\hat{\mathbf{\Phi}}^{d_c}_{BL,30}$ are calculated. Thus, d can be calculated and used as an estimated crack length. The cases considered are 18.18% and 27.27% crack lengths. Tab. 5.2 shows the results obtained for the estimated crack length d. The d values obtained in both crack cases are very accurate.

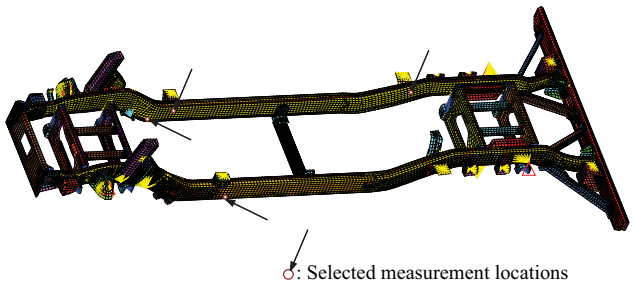

Figure 5.7: Optimal sensor locations based on the 30^{th} mode

Table 5.2: Estimated crack length d for high mobility multipurpose wheeled vehicle (HMMWV) modeled with shell-type elements

Actual crack length	d (30^{th} mode)
18.18%	18.97%
27.27%	27.41%

5.8.2 HMMWV model with solid-type elements

In the previous section, the sensor placement and crack length detection algorithm have been applied to a HMMWV model which uses shell-type elements. An important unanswered question is whether the in-plane motion of the two faces of the crack is very small. The thickness of the shell elements is considered very small. Hence, such in-plane motion cannot be modeled. Thus, only the open state motion of the structure is considered for the bilinear mode approximations. However, BMA can compute the resonant response of cracked structure by using both open and closed state motions. To demonstrate a more challenging case of application of BMA, the type of finite element used to discretize the structure was changed to solid elements. Specifically, the finite elements used to discretize the cross-member frame in the HMMWV model were solid-type elements. Fig. 5.8 shows

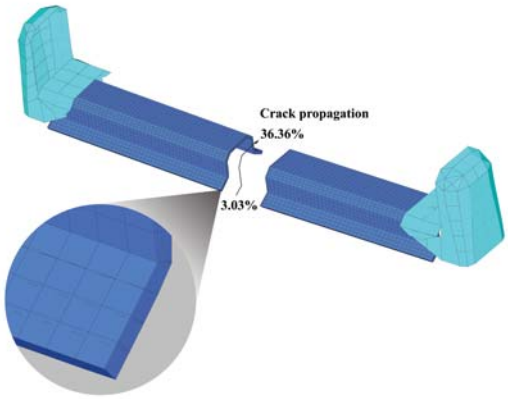

Figure 5.8: Substructure for the modified cracked cross-member modeled with solid-type elements

the modified model of the cross-member frame. The thickness variations in the reinforcement frame of the HMMWV model are the same as in the previous example. The crack length also varies (across the cross-member component) from 3.03% to 36.36%. PROMs were constructed and BMA was employed to approximate the response of the cracked HMMWV frame. The in-plane motions of the solid elements are not small, so the mode shapes of the open crack and the closed crack states are used to construct bilinear (BL) modes. A similar procedure as in the previous section was employed to calculate the generalized $\mathbf{MAC}$ matrix and to identify sensitive mode shapes for each crack length. Figures 5.9 shows the $\mathbf{MAC}$ matrices calculated between the healthy and the cracked structures with 30.30% and 36.36% crack length. The most sensitive and the second most sensitive modes are the 30^{th} and the 22^{nd} modes. These modes of the healthy and the cracked structures are used to identify the crack length separately. Using each of the two modes, the BL mode variation matrix $\delta\hat{\mathbf{\Phi}}_{BL,30}$ and $\delta\hat{\mathbf{\Phi}}_{BL,22}$ were computed for structures with three distinct crack lengths (same as in the previous section). However, when the

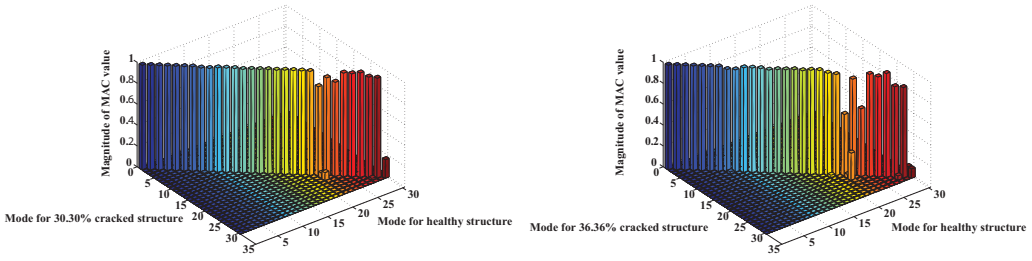

Figure 5.9: $\mathbf{MAC}$ between modes obtained using solid-type elements for the healthy high mobility multipurpose wheeled vehicle (HMMWV) and the structure with a 30.30% crack and 36.36% crack

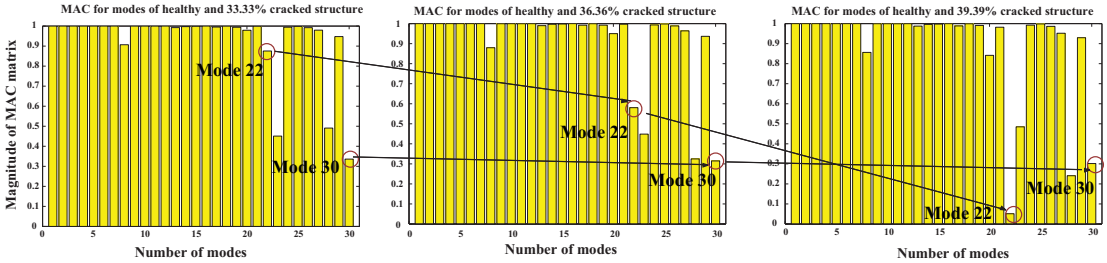

Figure 5.10: $\mathbf{MAC}$ between mode shapes with 4 measurement locations for the healthy and 33.33%, 36.36%, and 39.39% cracked structure

30^{th} mode is used to identify the crack length, the estimated crack length d calculated from Eq. (5.15) and described in Tab. 5.3 is not accurate. The reason is that the 30^{th} mode is very sensitive to a small crack but not sensitive to the crack growth. That is, this mode seems to be the most sensitive to the presence of the crack, but it does not vary much **once the crack grows**. In contrast, the 22^{nd} mode is less sensitive to small cracks, but varies as the crack growth. Figure 5.10 shows the diagonal entries of MAC matrices computed by using only the selected measurement DOFs. The $\mathbf{MAC}$ is between the healthy structure and structures with 33.33%, 36.36%, and 39.39% crack lengths. Figure 5.10 indicates that the $\mathbf{MAC}$ values for the 22^{nd} mode change sensitively of the crack length increases, but

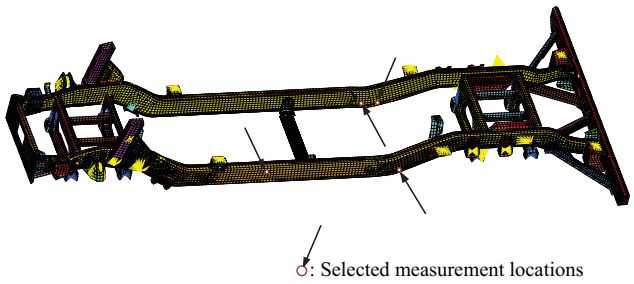

Figure 5.11: Optimal sensor locations based on the 22^{th} mode

Table 5.3: Estimated crack length d for HMMWV modeled with solid-type elements

Actual crack length	d (22^{th} mode)	d (30^{th} mode)
18.18%	18.91%	17.26%
27.27%	27.57%	27.57%
33.33%	33.75%	30.60%

the **MAC** values for the 30^{th} mode do not change significantly. In addition, for the case of 39.39% crack length, the 22^{nd} mode is more sensitive than the 30^{th} mode. Thus, for the sensor placement and damage identification algorithm, the 22^{nd} mode is employed. Figure 5.11 shows the optimal sensor locations used to identify the crack length employed the 22^{nd} mode. Tab. 5.3 shows results for the estimated crack length. The estimated values of the crack size variable d obtained for several crack cases agree very well with the actual crack length for the 22^{nd} mode.

5.8.3 Robust sensor locations based on Monte-Carlo technique

For identifying the crack length, mode shape information has been used. When the thickness of some components of the structure vary, the structural characteristics, especially mode shapes, are affected. Then, the optimal sensor locations may also be affected

Table 5.4: Several cases of thickness variations in substructures to identify crack length with statistically optimal sensor locations

Case	Substructure	Thickness variation	Case	Substructure	Thickness variation
1	L_{rear}	3.0 mm $\rightarrow$ 3.4 mm	2	L_{rear}	3.0 mm $\rightarrow$ 5.2 mm
	L_{front}	3.0 mm $\rightarrow$ 5.7 mm		L_{front}	3.0 mm $\rightarrow$ 5.8 mm
3	L_{rear}	3.0 mm $\rightarrow$ 3.7 mm	4	L_{rear}	3.0 mm $\rightarrow$ 5.5 mm
	L_{front}	3.0 mm $\rightarrow$ 4.2 mm		L_{front}	3.0 mm $\rightarrow$ 3.2 mm

by the change in the mode shapes. That means that robust sensor locations are required to capture the damage level in the presence of thickness variations. Herein, a Monte-Carlo technique is applied to determine statistically optimal and robust sensor locations. To apply the Monte-Carlo technique, several possible thickness variations are considered, and optimal sensor locations for the resulting mode shapes are obtained. To compute the mode shapes for each thickness variation, PROM techniques are applied. The main advantage of PROMs is that reanalysis is almost 100 times faster because any parameter value in the parameter range can be easily applied [35].

The reinforcement frames in the rear and the front (which are attached to the leftrails)

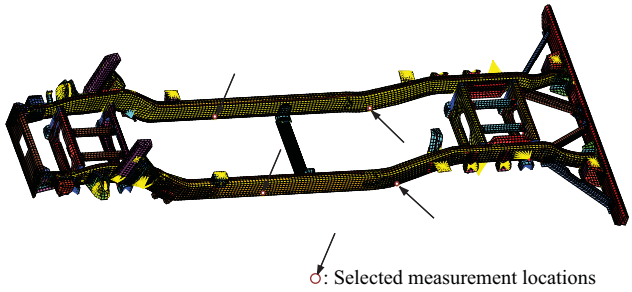

Figure 5.12: Statistically optimal sensor locations for 400 cases of thickness variations

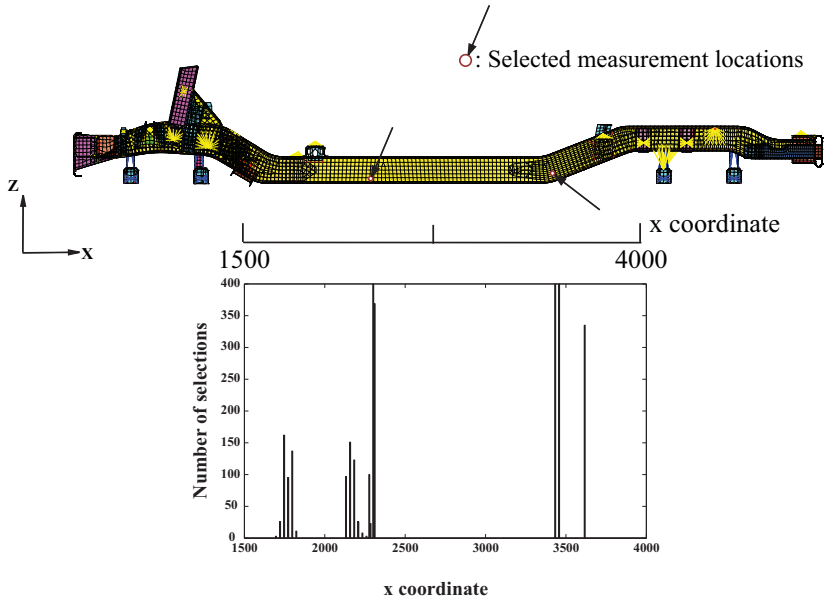

Figure 5.13: Optimal sensor locations distribution of leftrail frame structure for all cases of thickness variation

have thickness variations. For the Monte-Carlo technique, 400 separate cases of possible thickness variations are applied to these reinforcement frames. Sensitive modes to be used for sensor placement and the crack detection algorithm are selected from 20^{th} to 24^{th} mode based on $\mathbf{MAC}$ matrices. The total number of modes for the augmented bilinear modal matrix in Eq. (5.18) is 20. Then, the optimal number of measurement locations are decided based on the selected number of singular value of $\mathbf{\Phi}_{aug}^{EIDV}$ for each case of thickness variation. For instance, if all columns of $\mathbf{\Phi}_{aug}^{EIDV}$ in Eq. (5.18) are linearly independent, the selected number of singular values is 20. In contrast, if the columns of $\mathbf{\Phi}_{aug}^{EIDV}$ are not linearly independent, then the selected number of singular values is smaller than 20. By using the sensor placement algorithm for damage identification, 15 or 16 optimal measurement locations are selected for each case of thickness variation. Then, only four measurement points are selected for all cases of thickness variation. These four selected measurement locations are chosen to be the statistically optimal locations. Thus,

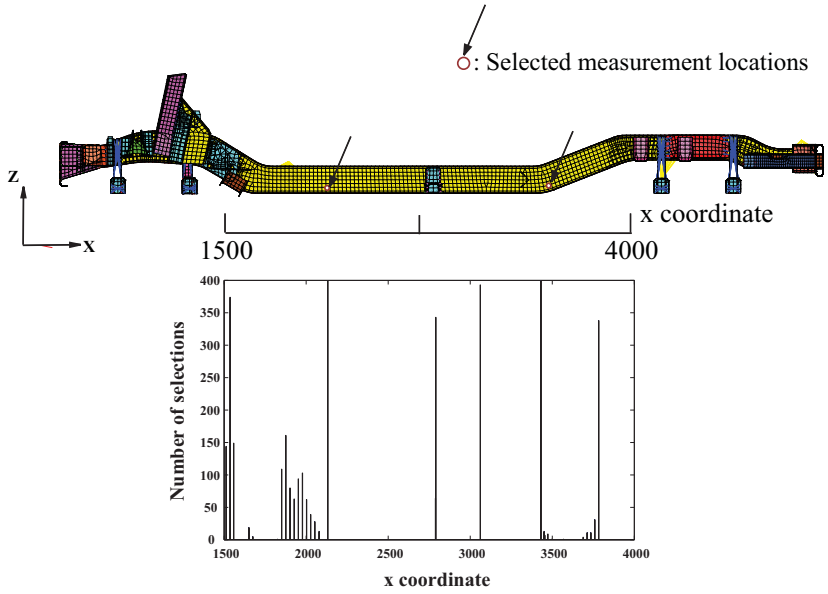

Figure 5.14: Optimal sensor locations distribution of rightrail frame structure for all cases of thickness variation

they are the most robust when used to identify the crack length. Figure 5.12 shows the four statistically optimal measurement locations obtained. Figures 5.13 and 5.14 represent the distribution of optimal sensor locations for the leftrail and the rightrail structure along the x coordinate for all cases of thickness variation. Using these four statistically optimal measurement locations, the crack length is identified for several cases of thickness variation described in Tab. 5.4. The damage identification algorithm is applied using the mode shapes corresponding to those variations, and the variable d (the estimated crack length) is estimated by solving Eq. (5.15). Tab. 5.5 provides a summary of the results obtained using statistical optimal sensor locations. The estimated crack length d agrees very well with the actual crack length for all cases of thickness variation. That indicating the statistically optimal sensor locations are robust to identify the crack length for any possible thickness variations.

Table 5.5: Estimated crack length d obtained using statistically optimal sensor locations

Case	Actual crack length	d	Case	Actual crack length	d
1	18.18%	18.52%	2	18.18%	18.49%
	27.27%	27.62%		27.27%	27.55%
	33.33%	33.41%		33.33%	33.79%
3	18.18%	18.61%	4	18.18%	18.37%
	27.27%	27.63%		27.27%	27.66%
	33.33%	33.39%		33.33%	33.36%

5.9 Conclusions

Identifying structural inspection points or desired sensor locations for the purpose of damage detection is a complex issue for cracked structures because of the nonlinear dynamics created by the crack opening and closing. A new concept of bilinear (BL) modes has been introduced. The BL modes are obtained using linear analysis techniques. To alleviate high computational costs and to allow for use in design applications, a reduced order modeling method based on Craig-Bampton component mode synthesis and multi-component parametric reduced order models was used. A generalized modal assurance criterion has been developed and used to find the BL modes that are most sensitive to the presence of a crack. Using the selected BL modes, an augmented BL modal matrix has been formed and used in an algorithm based on a modified effective independence distribution vector (EIDV) method to select optimal inspection points or measurement locations. Finally, the optimal set of measurement locations (for the cracked structure) was selected (by the modified EIDV algorithm) and the crack detection algorithm was applied to estimate the crack length (based on the selected optimal sensor locations). The esti-

mated crack length obtained was shown to agree well with the actual crack length. The techniques proposed herein are based on linear analyses and thus are highly efficient computationally. To select robust sensor locations for any thickness variation, a Monte-Carlo technique was implemented based on PROMs to select statistically optimal measurement locations. 400 cases of possible thickness variations were considered for the HMMWV frame, and four statistically optimal measurement locations were selected and observed to be robust to capture the crack length for in the presence of thickness variations.

CHAPTER VI

Joining of Components of Complex Structures for Improved Dynamic Response

6.1 Introduction

Mechanical structures such as those found in automobiles and airplanes consist of multiple components which are assembled using joints such as bolts, welds, rivets, etc. The locations (assembly points) of these joints affect structural performance characteristics such as the static compliance, the frequency response, and the durability. To achieve high performance, the joining locations should be selected by a systematic approach rather than an experience-based approach. However, this issue can be quite challenging because there are many joints and even more possible joining locations for large scale complex structures. The number of such joints can be as many as several thousand. The choice for joining locations can be improved/optimized by topology optimization approaches such as homogenization techniques [46] and density methods [47–49]. Homogenization techniques compute an optimal distribution of micro-structures in a given design domain. Density methods compute an optimal distribution of isotropic materials, where the material densities are design variables. Although the single-component topology design has been extensively studied during the past two decades [50], the amount of research done for multiple-component topology optimization is relatively small. In that area of research, Johanson *et*

al. [69] implemented the topology optimization techniques for multibody structural systems which possess joints between components. Chirehdast and Jiang [51] extended the concept of topology optimization to the design of spot-weld and adhesive bond patterns. A year later, Jiang and Chirehdast [52] proposed a theoretical framework to determine which optimal connection points minimize the static compliance of the given substructures. To solve the coupled problem of component topology and joining location optimization, Chickermane and Gea [53] considered a methodology for a multiple-component structure as a whole, in which the optimal topology and the joint locations were computed simultaneously. More recently, Zhu and Zhang [54] did layout optimization of structural supports using a topology optimization method for free vibration analyses. All these previous efforts employed spring elements for modeling joints. In contrast, Li *et al.* [55] proposed a fastener layout/topology that achieves an almost uniform stress level in each joint, and adopted evolutionary structural optimization [56–61] to provide an alternative optimization strategy to traditional gradient-based topology optimization approaches. In the context of these past efforts, the focus of this work is on the development of an efficient framework for determining improved/optimal joining locations as to minimize the total energy input into the structure and the strain energy in the joints of a complex structure with variability using a density-based method.

For general optimization processes, finite element models (FEMs) are typically used to evaluate the cost function. However, the number of degrees of freedom (DOFs) of FEMs of complex structures are prohibitively large. So, conventional FEMs are hard to employ due to the expensive time needed for each iteration. To reduce the computational cost, Craig-Bampton component mode synthesis (CB-CMS) was employed by Ma *et al.* [70] in a multi-domain topology optimization. The CB-CMS method is one of the most well-established methods for constructing reduced-order models (ROMs) [6–10]. However, if

one attempts to use CB-CMS techniques when parametric changes (such as thickness and geometrical variations) are applied during the design or exist through damage, the ROMs have to be reconstructed. This reconstruction requires other analyses in addition to the repetitive calculation of the cost function. This is computationally expensive and requires significant effort to prepare a FEM and a ROM for each reanalysis.

These challenges are addressed in this work as follows. First, the mean compliance for the dynamic case with damping is derived, and the strain energy in the joints is added to the cost function. Second, a novel approach to calculate the sensitivity of the strain energy in the joints efficiently is proposed. Third, the cost function and its sensitivity are computed in optimization process by using novel models which are able to manage structural variabilities. Recently, design oriented parametric reduced-order models (PROMs) have been developed to avoid such prohibitively expensive reanalyses of complex structures [28–30, 32, 35]. Here, the next-generation PROMs (NX-PROMs) developed by the authors in Chapter III are employed to allow complex structures to be divided into several components when determining improved/optimal joining locations.

This paper is organized as follows. In Sec. 6.2, a design methodology for determining improved/optimal joining locations is defined, which includes models for the joints, the definition of the associated cost function, and a computationally efficient method to determine design sensitivities for the cost function. In Sec. 6.3, NX-PROMs used in the calculations are reviewed. In Sec. 6.4, numerical simulations are used to demonstrate the proposed approach for the problem of attaching an armor plate to a structure with a V-shaped bottom. Finally, conclusions are summarized in Sec. 6.5

6.2 Design Methodology for Optimal Joining Locations

In single-component topology optimization, the primary objective is to obtain the optimal layout of the structure. When multi-component structures are considered, the problem is extended to select the optimal joining locations between components. This is done not only to optimize the layout of each of the subcomponents, but also because the joining locations affect the structural performance. Herein, a density-based topology optimization technique [47–49] is applied. Rozvany *et al.* [71] have defined this method as a modeling technique based on solid isotropic material with penalization (SIMP), where the distribution of the joining stiffness is optimized to improve the static or dynamic structural performance of the entire connected structure. The SIMP method has been developed to replace the size and orientation variables (of the holes used in the homogenization method [46]) with a density variable (of the finite elements) in the design domain. Herein, the idea of SIMP is employed to select optimal joining locations for the entire connected structure. To improve/optimize the joining locations, the stiffnesses of the joints are designed using density functions. Thus, the design variables are the densities (or stiffnesses) of the joints. These densities are continuous variables varying between 0 and 1. A location where the joint has a low density (close to 0) is not effective/adequate for joining, while a location where the joint has a density close to 1 is best for joining.

6.2.1 Design region - models for joints

Being one of the controversial tasks in structural FE analysis, modeling methods for joints have been extensively studied. Depending on the required accuracy and complexity of the problem at hand, an appropriate modeling strategy can be adopted for the joints. Several techniques for modeling joints were proposed in the literature [72–76]. For fatigue analyses based on local stresses and the local strength of the material, a fine mesh of

the structure and accurate joint models are required. For noise and vibration analysis of complex structures, a moderate level of accuracy and complexity is required, which leads to simple models for the joints. For a design optimization problem, and especially for a preliminary design, the simple flexible bar models are preferred [51, 53, 74, 77] because those joint models can be easily catered toward the iterative updating employed in design optimization.

In this work, the joints are modeled as three rectilinear springs. Let the stiffness associated with the motion of one of the two ends of a joint (of index i) be $\mathbf{k}_{s,i} = \mathbf{Diag}\left(\begin{bmatrix} k_{x,i} & k_{y,i} & k_{z,i} \end{bmatrix}\right)$, where $k_{x,i}$, $k_{y,i}$, and $k_{z,i}$ denote the stiffnesses of the spring along the three directions of a local Cartesian reference system associated with joint i. Here, $\mathbf{Diag}(\mathbf{v})$ represents a diagonal matrix with entries given by the vector $\mathbf{v}$. The directional stiffnesses of a joint are often related to each other. In this work, it is assumed that $k_{x,i} = k_{z,i} = \alpha_i k_i$ and $k_{y,i} = k_i$. This is the case for joints such as bolts, rivets, spot welds, etc, where y is the axis of the joint (e.g., the axis of a bolt). Thus, a joint is modeled as having 6 DOFs linked by three springs. The stiffness matrix for the i^{th} joint can thus be written as

$$\mathbf{K}_{s,i} = \begin{bmatrix} \mathbf{k}_{s,i} & -\mathbf{k}_{s,i} \\ -\mathbf{k}_{s,i} & \mathbf{k}_{s,i} \end{bmatrix},$$

where $\mathbf{k}_{s,i} = k_i \mathbf{Diag}\left(\begin{bmatrix} \alpha_i & 1 & \alpha_i \end{bmatrix}\right)$.

The joints (modeled as three rectilinear springs) are designed using density functions in the SIMP method. According to the SIMP method, the design elements are written using the densities ρ_i as

$$\mathbf{K}_{b,i} = \rho_i^p \begin{bmatrix} \mathbf{k}_{s,i} & -\mathbf{k}_{s,i} \\ -\mathbf{k}_{s,i} & \mathbf{k}_{s,i} \end{bmatrix} = \rho_i^p \mathbf{K}_{s,i}, \tag{6.1}$$

where $\mathbf{K}_{b,i}$ represents the joining stiffness matrix for the i^{th} candidate joining location.

Thus, $\mathbf{K}_{b,i}$ is a density-based function. Intermediate values of ρ_i $(0 < \rho_i < 1)$ are penalized compared to values of 0 or 1 by the use of the penalty exponent p. This exponent is typically $p = 3$ for a structural optimization problem [78, 79]. Also, for simplicity, we assume that α_i has the same value for all joints. Thus, only one density variable is assigned to a joint.

The system-level joining stiffness matrix $\mathbf{K}_b$ is given by

$$\mathbf{K}_b = \mathbf{Bdiag}\left[\begin{array}{cccc} \mathbf{K}_{b,1} & \mathbf{K}_{b,2} & \cdots & \mathbf{K}_{b,g} \end{array}\right], \tag{6.2}$$

where $\mathbf{Bdiag}$ denotes a block-diagonal matrix, and g is the number of candidate joining locations. Then, the system-level governing equation for the structural dynamic problem with (structural) damping γ is

$$\mathbf{M}_0 \left[\begin{array}{c} \ddot{\mathbf{u}}_b \\ \\ \ddot{\mathbf{u}}_r \end{array}\right] + (1 + j\gamma)\left(\mathbf{K}_0 + \left[\begin{array}{cc} \mathbf{K}_b & \mathbf{0} \\ \\ \mathbf{0} & \mathbf{0} \end{array}\right]\right)\left[\begin{array}{c} \mathbf{u}_b \\ \\ \mathbf{u}_r \end{array}\right] = \left[\begin{array}{c} \mathbf{f}_b \\ \\ \mathbf{f}_r \end{array}\right], \tag{6.3}$$

where $j = \sqrt{-1}$, $\mathbf{M}_0$ and $\mathbf{K}_0$ are the system-level mass and stiffness matrices which do not include the joining stiffness matrix $\mathbf{K}_b$. Subscript b indicates the candidate joining DOFs, and subscript r denotes the remaining DOFs. Note that a joining mass matrix $\mathbf{M}_b$ does not exist because massless spring elements are used. Based on Eq. (6.3), the dynamic response of all DOFs, $\mathbf{u}_r$ (remainder) and $\mathbf{u}_b$ (joint), are obtained.

6.2.2 Formulation of the optimization problem

The approach employed here is based on an energy criterion which is commonly used in structural optimization problems. Two energies are used. The first is the total energy input into the structure under dynamic loading. This total energy input is equal to the external work done on the structure, which can be defined in function of the mean compliance of the structure. For the dynamic case, the total work done on the structure by

external forces is

$$Re\left(\int \mathbf{F}^{\mathrm{T}}\mathrm{d}\mathbf{u}\right) = Re\left(\int_0^T \mathbf{F}^{\mathrm{T}}\frac{\mathrm{d}\mathbf{u}}{\mathrm{d}t}\mathrm{d}t\right) = Re\left(\int_0^T \mathbf{F}^{\mathrm{T}}\dot{\mathbf{u}}\mathrm{d}t\right), \tag{6.4}$$

where $\mathbf{F} = \mathbf{f}e^{j\omega t}$ is the external harmonic forcing, and $\mathbf{u}$ is the displacement due to the harmonic forcing. The phase reference for the calculation is chosen such that $\mathbf{f}$ is real. For structures with damping, the response $\mathbf{u}$ is complex and can be expressed as

$$\mathbf{u} = (\mathbf{u}_R + j\mathbf{u}_I)\mathrm{e}^{j\omega t} \quad \text{so that} \quad \dot{\mathbf{u}} = (j\omega\mathbf{u}_R - \omega\mathbf{u}_I)\mathrm{e}^{j\omega t}, \tag{6.5}$$

where subscripts R and I indicate real and imaginary parts. From Eq. (6.5), the real valued portion of the velocity is

$$Re(\dot{\mathbf{u}}) = -\omega\mathbf{u}_I\cos\omega t - \omega\mathbf{u}_R\sin\omega t. \tag{6.6}$$

Substituting Eq. (6.6) into Eq. (6.4) and (for convenience) using the fact that $\mathbf{f}$ is real, one obtains

$$\begin{aligned} Re\left(\int_0^T \mathbf{F}^{\mathrm{T}}\dot{\mathbf{u}}\mathrm{d}t\right) &= -\int_0^T \mathbf{f}^{\mathrm{T}}\cos\omega t(\omega\mathbf{u}_I\cos\omega t + \omega\mathbf{u}_R\sin\omega t)\mathrm{d}t \\ &= -\omega\mathbf{f}^{\mathrm{T}}\mathbf{u}_I\int_0^T \cos^2\omega t\mathrm{d}t = -\frac{\omega T}{2}\mathbf{f}^{\mathrm{T}}\mathbf{u}_I \\ &= -\pi\mathbf{f}^{\mathrm{T}}\mathbf{u}_I = -\pi(\mathbf{f}^{\mathrm{T}}\mathbf{u})_I. \end{aligned}$$

The resulting first component of the cost function c_1 is thus

$$c_1 = -\left(\mathbf{f}^{\mathrm{T}}\mathbf{u}\right)_I, \tag{6.7}$$

and contains the strain energy in the entire structure, including the joints. Note that Eq. (6.7) holds also when $\mathbf{ff}$ is not real. However, focusing on the durability of the joints, the strain energy in the joints should be taken into account. Thus, the second component of the cost function is based on the strain energy in the joints. This energy can be expressed as

$$c_2 = \frac{1}{2}\mathbf{u}_b^{\mathrm{H}}\mathbf{K}_b\mathbf{u}_b, \tag{6.8}$$

where the superscript H indicates the Hermitian operator. Then, by assembling the two components c_1 and c_2 of the cost function from Eq. (6.7) and Eq. (6.8), the final cost function for this optimization problem is

$$c = w_1 c_1 + w_2 c_2 = -w_1 \left(\mathbf{f}^{\mathrm{T}}\mathbf{u}\right)_I + w_2 \frac{1}{2}\mathbf{u}_b \mathbf{K}_b^{\mathrm{H}} \mathbf{u}_b,$$

where w_1 and w_2 are weighting factors to control the relative importance of overall structural vibration and joint durability.

Naturally, the number of joints to be distributed in the design domain is limited. Thus, the topology optimization problem associated with the joining location design can be stated as

$$\begin{aligned} \text{Minimize}: \qquad & c(\boldsymbol{\rho}) \;\; = -w_1 \left(\mathbf{f}^{\mathrm{T}}\mathbf{u}\right)_I + w_2 \frac{1}{2}\mathbf{u}_b \mathbf{K}_b^{\mathrm{T}} \mathbf{u}_b, \\ \text{Subject to}: \qquad & g(\boldsymbol{\rho}) \;\; = \sum_{i=1}^{g} \rho_i - N \leq 0; \;\; 0 < \rho_{min} \leq \rho_i \leq 1, \end{aligned} \tag{6.9}$$

where N denotes the total number of joints allowed in the design, g is the total number of candidate joint locations, and ρ_{min} is a sufficiently small lower bound imposed to avoid numerical instabilities (herein $\rho_{min} = 0.001$).

To solve such optimization problems, specific methods have been developed to handle a large number of design variables with a few constraints. Among these techniques, the method of moving asymptotes (MMA) [80, 81] and the optimality criterion (OC) [46, 82] methods are broadly utilized for their efficacy and generality. The MMA method is based on the convex approximation method with the advanced feature of setting asymptotic moving limits to approximation variables. The OC makes use of the well-known Karush-Khun-Tucker condition to satisfy a set of criteria related to the behavior of the structure. Even though the OC method is well-convergent for static cases, it is not effective for the dynamic case. Thus, herein we use the modified optimality criterion (MOC) method [82],

which is also a gradient-based optimizer.

6.2.3 Sensitivities of the cost function

The design domain for joining is modeled with the density-based three rectilinear springs, each having a design variable ρ_i (density), as in Eq. (6.1). The variable ρ_i is varied between 0 and 1 using the MOC method to select improved/optimal joining locations. For any gradient-based optimizer, the design sensitivities of the cost function and of the constraints with respect to the design variables are required. For an efficient calculation of the design sensitivities for the dynamic case discussed here, an adjoint variable method [83] is applied. First, we consider the design sensitivities of c_1 given by in Eq. (6.7). The derivative of c_1 with respect to the m^{th} design variable ρ_m is

$$\frac{\partial c_1\left(\boldsymbol{\rho}\right)}{\partial \rho_m} = -\left(\begin{bmatrix} \mathbf{f}_b \\ \mathbf{f}_r \end{bmatrix}^{\mathrm{T}} \begin{bmatrix} \frac{\partial \mathbf{u}_b}{\partial \rho_m} \\ \frac{\partial \mathbf{u}_r}{\partial \rho_m} \end{bmatrix} \right)_I = -\left(\begin{bmatrix} \mathbf{f}_b \\ \mathbf{f}_r \end{bmatrix}^{\mathrm{T}} \boldsymbol{\lambda} \right)_I .$$

The direct calculation of $\begin{bmatrix} \frac{\partial \mathbf{u}_b}{\partial \rho_m} \\ \frac{\partial \mathbf{u}_r}{\partial \rho_m} \end{bmatrix}$ is cumbersome, so an adjoint variable $\boldsymbol{\lambda}$ is used. To obtain $\boldsymbol{\lambda}$, the equilibrium Eq. (6.3) is differentiated with respect to the design variable ρ_m to obtain

$$\frac{\partial \mathbf{G}}{\partial \rho_m} \begin{bmatrix} \mathbf{u}_b \\ \mathbf{u}_r \end{bmatrix} + \mathbf{G} \begin{bmatrix} \frac{\partial \mathbf{u}_b}{\rho_m} \\ \frac{\partial \mathbf{u}_r}{\partial \rho_m} \end{bmatrix} = \mathbf{0}, \tag{6.10}$$

where

$$\mathbf{G} = -\omega^2 \mathbf{M}_0 + (1 + j\gamma) \left(\mathbf{K}_0 + \begin{bmatrix} \mathbf{K}_b & \mathbf{0} \\ \mathbf{0} & \mathbf{0} \end{bmatrix} \right).$$

Multiplying Eq. (6.10) by $\begin{bmatrix} \mathbf{u}_b \\ \mathbf{u}_r \end{bmatrix}^{\mathrm{T}}$, one obtains

$$\begin{bmatrix} \mathbf{u}_b \\ \mathbf{u}_r \end{bmatrix}^{\mathrm{T}} \mathbf{G} \begin{bmatrix} \frac{\partial \mathbf{u}_b}{\rho_m} \\ \frac{\partial \mathbf{u}_r}{\partial \rho_m} \end{bmatrix} = \begin{bmatrix} \mathbf{f}_b \\ \mathbf{f}_r \end{bmatrix}^{\mathrm{T}} \boldsymbol{\lambda} = - \begin{bmatrix} \mathbf{u}_b \\ \mathbf{u}_r \end{bmatrix}^{\mathrm{T}} \begin{bmatrix} \frac{\partial \mathbf{K}_b}{\rho_m} & \mathbf{0} \\ \mathbf{0} & \mathbf{0} \end{bmatrix} \begin{bmatrix} \mathbf{u}_b \\ \mathbf{u}_r \end{bmatrix}.$$

Thus, the design sensitivity of c_1 to ρ_m is given by

$$\begin{aligned} \frac{\partial c_1(\boldsymbol{\rho})}{\partial \rho_m} &= - \left(\begin{bmatrix} \mathbf{f}_b \\ \mathbf{f}_r \end{bmatrix}^{\mathrm{T}} \boldsymbol{\lambda} \right)_I = - \left(\mathbf{u}_b^{\mathrm{T}} \frac{\partial \mathbf{K}_b}{\partial \rho_m} \mathbf{u}_b \right)_I \\ &= - \left(\mathbf{u}_{b,m}^{\mathrm{T}} \frac{\partial \left(\rho_m^p \mathbf{K}_{s,m} \right)}{\partial \rho_m} \mathbf{u}_{b,m} \right)_I = - \left(p \rho_m^{p-1} \mathbf{u}_{b,m}^{\mathrm{T}} \mathbf{K}_{s,m} \mathbf{u}_{b,m} \right)_I . \end{aligned} \tag{6.11}$$

Second, the sensitivity of c_2 with respect to ρ_m is considered. One obtains

$$\frac{\partial c_2(\boldsymbol{\rho})}{\partial \rho_m} = \frac{1}{2} \left[2 \mathbf{u}_b^{\mathrm{H}} \mathbf{K}_b \frac{\partial \mathbf{u}_b}{\partial \rho_m} + \mathbf{u}_b^{\mathrm{H}} \frac{\partial \mathbf{K}_b}{\partial \rho_m} \mathbf{u}_b \right], \tag{6.12}$$

where the fact that $\mathbf{K}_b$ is a real, symmetric matrix was used. This sensitivity requires the calculation of $\frac{\partial \mathbf{K}_b}{\partial \rho_m}$ and $\frac{\partial \mathbf{u}_b}{\partial \rho_m}$. The first term $\frac{\partial \mathbf{K}_b}{\partial \rho_m}$ can be easily calculated because it has a simple analytical form. Next, from Eq. (6.10), one obtains

$$\begin{bmatrix} \frac{\partial \mathbf{u}_b}{\partial \rho_m} \\ \frac{\partial \mathbf{u}_r}{\partial \rho_m} \end{bmatrix} = - (1 + j\gamma) \mathbf{G}^{-1} \begin{bmatrix} \frac{\partial \mathbf{K}_b}{\partial \rho_m} \mathbf{u}_b \\ \mathbf{0} \end{bmatrix}. \tag{6.13}$$

This equation could, in principle, be used to compute $\frac{\partial \mathbf{u}_b}{\partial \rho_m}$ once $\frac{\partial \mathbf{K}_b}{\partial \rho_m}$ is calculated. However, using Eq. (6.13) requires the inverse of $\mathbf{G}$ at each iteration. This matrix is very large because it is a full-order, system-level matrix. Also, $\mathbf{G}$ depends on excitation frequency ω, so this inversion has to be done at each frequency in the range of interest. To avoid such a high computational effort, we propose a novel approach. To calculate $\frac{\partial \mathbf{u}_b}{\partial \rho_m}$, first, Eq. (6.3)

is used to obtain

$$\begin{aligned}\left(-\omega^2\mathbf{M}_0+(1+j\gamma)\,\mathbf{K}_0\right)\begin{bmatrix}\frac{\partial\mathbf{u}_b}{\partial\rho_m}\\ \\ \frac{\partial\mathbf{u}_r}{\partial\rho_m}\end{bmatrix} &+ (1+j\gamma)\begin{bmatrix}\frac{\partial\mathbf{K}_b}{\partial\rho_m} & \mathbf{0}\\ \\ \mathbf{0} & \mathbf{0}\end{bmatrix}\begin{bmatrix}\mathbf{u}_b\\ \\ \mathbf{u}_r\end{bmatrix}\\ &+ (1+j\gamma)\begin{bmatrix}\mathbf{K}_b & \mathbf{0}\\ \\ \mathbf{0} & \mathbf{0}\end{bmatrix}\begin{bmatrix}\frac{\partial\mathbf{u}_b}{\partial\rho_m}\\ \\ \frac{\partial\mathbf{u}_r}{\partial\rho_m}\end{bmatrix}=0.\end{aligned} \tag{6.14}$$

Then, substituting Eq. (6.13) into Eq. (6.14), one obtains

$$\begin{aligned}\begin{bmatrix}\mathbf{K}_b\frac{\partial\mathbf{u}_b}{\partial\rho_m}\\ \\ \mathbf{0}\end{bmatrix} &= \mathbf{G}_0\mathbf{G}^{-1}\begin{bmatrix}\frac{\partial\mathbf{K}_b}{\partial\rho_m}\mathbf{u}_b\\ \\ \mathbf{0}\end{bmatrix}-\begin{bmatrix}\frac{\partial\mathbf{K}_b}{\partial\rho_m}\mathbf{u}_b\\ \\ \mathbf{0}\end{bmatrix}\\ &= \left(\mathbf{G}_0\mathbf{G}^{-1}-\mathbf{I}\right)\begin{bmatrix}\frac{\partial\mathbf{K}_b}{\partial\rho_m}\mathbf{u}_b\\ \\ \mathbf{0}\end{bmatrix},\end{aligned} \tag{6.15}$$

where $\mathbf{G}_0=(-\omega^2\mathbf{M}_0+(1+j\gamma)\,\mathbf{K}_0)$. The quantity $\mathbf{G}_0\mathbf{G}^{-1}$ in Eq. (6.15) can be written as

$$\mathbf{G}_0\mathbf{G}^{-1}=\left(\mathbf{I}+(1+j\gamma)\begin{bmatrix}\mathbf{K}_b & \mathbf{0}\\ \\ \mathbf{0} & \mathbf{0}\end{bmatrix}\mathbf{G}_0^{-1}\right)^{-1}. \tag{6.16}$$

Then, substituting Eq. (6.16) into Eq. (6.15), one obtains

$$\begin{bmatrix}\mathbf{K}_b\frac{\partial\mathbf{u}_b}{\partial\rho_m}\\ \\ \mathbf{0}\end{bmatrix}=\left[\left(\mathbf{I}+(1+j\gamma)\begin{bmatrix}\mathbf{K}_0 & \mathbf{0}\\ \\ \mathbf{0} & \mathbf{0}\end{bmatrix}\mathbf{G}_0^{-1}\right)^{-1}-\mathbf{I}\right]\begin{bmatrix}\frac{\partial\mathbf{K}_b}{\partial\rho_m}\mathbf{u}_b\\ \\ \mathbf{0}\end{bmatrix}. \tag{6.17}$$

The novel approach uses the assumption that the values of the (spring) stiffnesses of the joints are much smaller than the values of the stiffnesses in the nominal structure. Thus, we assume that, for all DOFs of indices i_1 and i_2,

$$\left(\begin{bmatrix}\mathbf{K}_0 & \mathbf{0}\\ \\ \mathbf{0} & \mathbf{0}\end{bmatrix}\mathbf{G}_0^{-1}\right)_{i_1 i_2}\ll 1.$$

Then, the inverse term in Eq. (6.17) can be written as

$$\left(\mathbf{I} + (1+j\gamma) \begin{bmatrix} \mathbf{K}_0 & \mathbf{0} \\ \mathbf{0} & \mathbf{0} \end{bmatrix} \mathbf{G}_0^{-1} \right)^{-1} \approx \mathbf{I} - (1+j\gamma) \begin{bmatrix} \mathbf{K}_0 & \mathbf{0} \\ \mathbf{0} & \mathbf{0} \end{bmatrix} \mathbf{G}_0^{-1}. \tag{6.18}$$

Substituting Eq. (6.18) into Eq. (6.17), one obtains

$$\begin{bmatrix} \mathbf{K}_b \frac{\partial \mathbf{u}_b}{\partial \rho_m} \\ \mathbf{0} \end{bmatrix} = \left(-(1+j\gamma) \begin{bmatrix} \mathbf{K}_0 & \mathbf{0} \\ \mathbf{0} & \mathbf{0} \end{bmatrix} \mathbf{G}_0^{-1} \right) \begin{bmatrix} \frac{\partial \mathbf{K}_b}{\partial \rho_m} \mathbf{u}_b \\ \mathbf{0} \end{bmatrix}. \tag{6.19}$$

Of course, Eq. (6.19) can be used to obtain $\frac{\partial \mathbf{u}_b}{\partial \rho_m}$. However, Eq. (6.19) requires the calculation of the inverse of $\mathbf{G}_0$. Inverting $\mathbf{G}_0$ has to be done only once during the iterations because $\mathbf{G}_0$ does not depend on $\mathbf{K}_b$. However, $\mathbf{G}_0$ does depend on the excitation frequency ω, which means that $\mathbf{G}_0$ has to be inverted at all frequencies in the range of interest. Also, $\mathbf{G}_0$ is a large matrix because it is a full-order, system-level matrix. Thus, this calculation is very time consuming. A new approach to address this issue is presented next. The key term to be calculated in Eq. (6.19) is $\mathbf{G}_0^{-1} \begin{bmatrix} \frac{\partial \mathbf{K}_b}{\partial \rho_m} \mathbf{u}_b \\ \mathbf{0} \end{bmatrix}$. To compute this term, we consider first that a unit force is applied at the m^{th} joining location and to the a^{th} DOFs (at that location). The index a varies from 1 to the number L of DOFs used in the finite elements which contain the joining node m. For example, $L = 6$ for shell-type elements, while $L = 3$ for brick-type elements. Then, the resulting deformation $\mathbf{\Psi}_{m,a}$ can be expressed as

$$\mathbf{\Psi}_{m,a} = \mathbf{G}_0^{-1} \cdot \begin{bmatrix} 0 & 0 & \cdots & 1_{m,a} & 0 & 0 \end{bmatrix}^{\mathrm{T}},$$

where $\mathbf{\Psi}_{m,a}$ indicates the deformation everywhere in the system due to the unit force applied at the a^{th} DOFs of the m^{th} joint location.

Next, we express the difficult term as

$$\begin{aligned}
\mathbf{G}_0^{-1}\begin{bmatrix} \frac{\partial \mathbf{K}_b}{\partial \rho_m}\mathbf{u}_b \\ \mathbf{0} \end{bmatrix} &= \sum_{a=1}^{L} \mathbf{G}_0^{-1}\begin{bmatrix} 0 \\ \vdots \\ 1_{m,a} \\ \vdots \\ 0 \end{bmatrix}\left(\frac{\partial \mathbf{K}_{b,m}}{\partial \rho_m}\mathbf{u}_{b,m}\right) \\
&= \sum_{a=1}^{L} \mathbf{\Psi}_{m,a}\frac{\partial\left(\rho_m^p \mathbf{K}_{s,m}\right)}{\partial \rho_m}\mathbf{u}_{b,m} \\
&= \sum_{a=1}^{L} p\rho_m^{p-1}\mathbf{\Psi}_{m,a}\left(\mathbf{K}_{s,m}\mathbf{u}_{b,m}\right)_a .
\end{aligned}$$

Thus, the sensitivity of c_2 in Eq. (6.12) can be expressed as

$$\frac{\partial c_2(\boldsymbol{\rho})}{\partial \rho_m} = \frac{1}{2}\left(-2\sum_{i=1}^{n}\mathbf{A}_i + p\rho_m^{p-1}\mathbf{u}_{b,m}^{\mathrm{H}}\mathbf{K}_{s,m}\mathbf{u}_{b,m}\right), \tag{6.20}$$

where

$$\mathbf{A}_i = \rho_i^p \mathbf{u}_{b,i}^{\mathrm{H}}\mathbf{K}_{b,i}(1+j\gamma)\left[\sum_{a=1}^{L} p\rho_m^{p-1}\left(\mathbf{\Psi}_{m,a}\right)_i\left(\mathbf{K}_{s,m}\mathbf{u}_{b,m}\right)_a\right].$$

Finally, the design sensitivity of the entire cost function for the m^{th} design variable is obtained using Eqs. (6.11) and (6.20) as

$$\begin{aligned}
\frac{\partial c(\boldsymbol{\rho})}{\partial \rho_m} = &- w_1\left(p\rho_m^{p-1}\mathbf{u}_{b,m}^{\mathrm{T}}\mathbf{K}_s\mathbf{u}_{b,m}\right)_I \\
&+ w_2\frac{1}{2}\left(-2\sum_{i=1}^{n}\mathbf{A}_i + p\rho_m^{p-1}\mathbf{u}_{b,m}^{\mathrm{H}}\mathbf{K}_s\mathbf{u}_{b,m}\right).
\end{aligned}$$

Computing the sensitivities of the entire cost function based on this formulation is fast especially because vectors $\mathbf{\Psi}_{m,a}$ have to be calculated only once. They remain unchanged during the optimization iterations.

6.3 Next-Generation Parametric Reduced-Order Models (PROMs)

The cost function and design sensitivities are presented in Sec. 6.2 as if they are calculated based on full-order finite element models. However, if the structure has a huge number of DOFs, the turn-around time of the optimization iteration process is very long. This issue is particularly important when the design involves not only choosing joining locations, but also modifications of various components of the structure. In that case, the full-order model of the modified components changes, which requires additional computational effort. To address this issue, a new modeling approach is presented next. This approach is based on next-generation parametric reduced-order models (NX-PROMs) used together with the well-known fixed-interface Craig-Bampton component mode synthesis (CB-CMS) [7]. A review of this approach is provided next.

6.3.1 Modeling approach

CB-CMS [7] is used to model only the substructures which do not have any structural variability. This modeling approach is used because it is very simple and computationally stable. To apply CB-CMS, the complex structure of interest is divided into several substructures, and their DOFs are partitioned into internal and interface DOFs. The interface DOFs for a substructure (of index q) are projected onto the generalized coordinates by using static constraint modes $\mathbf{\Psi}_q^C$. The internal DOFs are projected onto fixed-interface normal modes $\mathbf{\Phi}_q^N$. Then, the size of the mass and stiffness matrices and the force vector for substructure q is significantly reduced as follows

$$\mathbf{M}_q^{CB} = \begin{bmatrix} \mathbf{m}_q^C & \mathbf{m}_q^{CN} \\ \mathbf{m}_q^{NC} & \mathbf{m}_q^N \end{bmatrix}, \mathbf{K}_q^{CB} = \begin{bmatrix} \mathbf{k}_q^C & \mathbf{k}_q^{CN} \\ \mathbf{k}_q^{NC} & \mathbf{k}_q^N \end{bmatrix}, \mathbf{F}_q^{CB} = \begin{bmatrix} \mathbf{f}_q^C \\ \mathbf{f}_q^N \end{bmatrix},$$

where the superscript C indicates generalized interface DOFs (i.e., constraint partitions). These DOFs are used to assemble substructural matrices and obtain system-level reduced

matrices. The superscript N indicates generalized internal DOFs. These DOFs are used to reduce the number of internal DOFs.

The substructures which can have variability are modeled using NX-PROMs. One important advantage of NX-PROMs is that the finite element mesh of the nominal structure does not need to be modified although several substructures may have variability. That is because the mass and stiffness matrices of these substructures are parameterized. The NX-PROM approach resembles the CB-CMS approach. However, the transformation matrix for NX-PROMs is constructed for all values of the variable parameters in the parameter space of each component with variability. In contrast, components with no parameter variability do not need a parameterization, so they are modeled by CB-CMS. By applying the NX-PROM approach to the l^{th} substructure with variation Δp in one of its parameters, the mass and stiffness matrices and force vector are obtained as

$$\begin{aligned}
\mathbf{M}_l^{NX} &= \begin{bmatrix} \mathbf{m}_{\Delta p,l}^{C} & \mathbf{m}_{\Delta p,l}^{CN} \\ \mathbf{m}_{\Delta p,l}^{NC} & \mathbf{m}_{\Delta p,l}^{N} \end{bmatrix}, \mathbf{K}_l^{NX} = \begin{bmatrix} \mathbf{k}_{\Delta p,l}^{C} & \mathbf{k}_{\Delta p,l}^{CN} \\ \mathbf{k}_{\Delta p,l}^{NC} & \mathbf{k}_{\Delta p,l}^{N} \end{bmatrix}, \\
\mathbf{F}_l^{NX} &= \begin{bmatrix} \mathbf{f}_{\Delta p,l}^{C} \\ \mathbf{f}_{\Delta p,l}^{N} \end{bmatrix},
\end{aligned}$$

6.3.2 Geometric compatibility conditions

The complete, reduced-order component-level equations of motion for each component l of the entire set of n components can be expressed as

$$\mathbf{M}_l^{ROM}\ddot{\mathbf{q}}_l^{ROM} + \mathbf{K}_l^{ROM}\mathbf{q}_l^{ROM} = \mathbf{F}_l^{ROM}, \tag{6.21}$$

where the superscript ROM indicates that either CB-CMS or NX-PROM was used, with q_l being the generalized coordinates ($l = 1, \cdots, n$).

The constraint partitions (indicated by superscript C) of component-level matrices retain the physical meaning of the interface DOFs. This means that the geometric com-

patibility conditions at the interfaces with no joints can be applied directly to construct the system-level matrices. Consider, for example that an interface with no joints exists between components l and d ($d = 1, \cdots, n$, $d \neq l$). Then,

$$\mathbf{q}_l^C = \mathbf{q}_d^C, \tag{6.22}$$

where $\mathbf{q}_l^C$ and $\mathbf{q}_d^C$ are the generalized coordinates for the constraint partitions that correspond to the interface between substructures l and d. Of course, there is no compatibility condition to be enforced for two components which do not have a common interface. Equation (6.22) is used to transform the matrices in Eq. (6.21) in a manner similar to the assembly process in all finite element modeling methods. Then, the system-level equation of motion which does not include the joints is given by

$$\mathbf{M}_{sys}^{ROM}\ddot{\mathbf{q}}_{sys}^{ROM} + \mathbf{K}_{sys}^{ROM}\mathbf{q}_{sys}^{ROM} = \mathbf{F}_{sys}^{ROM}. \tag{6.23}$$

Equation (6.23) is obtained after all geometric compatibility condition have been enforced, except for the conditions present at the interfaces with joints. To tackle the joints, the (remaining) constraint partitions corresponding to the joints are repartitioned in two pieces. These pieces are indicated by superscript C_1 and C_2. The C_1 portion corresponds the DOFs of one end of all joints and the C_2 portion corresponds to the DOFs of the other end of all joints. Thus, the matrices in Eq. (6.23) can be expressed as

Table 6.1: Thickness variation for substructure 5 and for the armor plate

Substructure	Nominal	Case 1	Case 2
6 (parameter h_1)	6 mm	7.5 mm	8.5 mm
$\mathrm{Armor\ plate}$ (parameter h_2)	10 mm	10.5 mm	11.1 mm

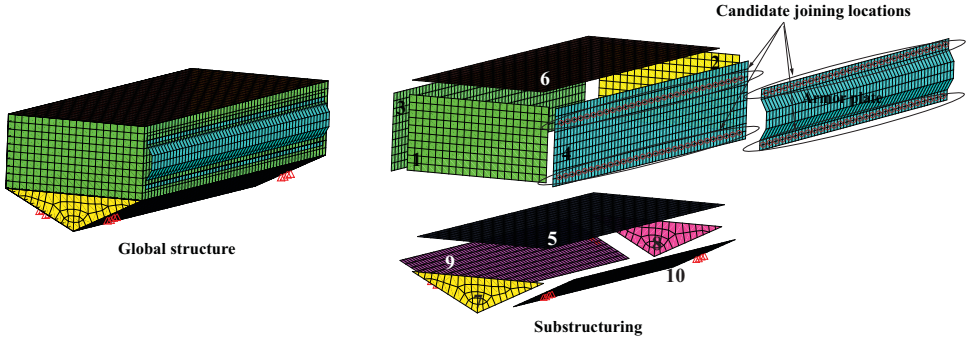

Figure 6.1: Structure with a V-shaped bottom; indices of the substructures are shown

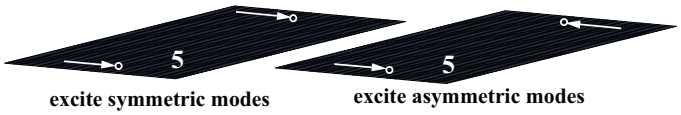

Figure 6.2: Dynamic loads applied to substructure 5 to excite symmetric and asymmetric modes of the entire structure

$$
\begin{aligned}
\mathbf{M}_{sys}^{ROM} &= \begin{bmatrix} \mathbf{M}^{\bar{C}} & \mathbf{M}^{\bar{C}N} \\ \mathbf{M}^{N\bar{C}} & \mathbf{M}^{N} \end{bmatrix} = \begin{bmatrix} \mathbf{M}^{C_1} & \mathbf{0} & \mathbf{M}^{C_1N} \\ \mathbf{0} & \mathbf{M}^{C_2} & \mathbf{M}^{C_2N} \\ \mathbf{M}^{NC_1} & \mathbf{M}^{NC_2} & \mathbf{M}^{N} \end{bmatrix}, \\
\mathbf{K}_{sys}^{ROM} &= \begin{bmatrix} \mathbf{K}^{\bar{C}} & \mathbf{K}^{\bar{C}N} \\ \mathbf{K}^{N\bar{C}} & \mathbf{K}^{N} \end{bmatrix} = \begin{bmatrix} \mathbf{K}^{C_1} & \mathbf{0} & \mathbf{K}^{C_1N} \\ \mathbf{0} & \mathbf{K}^{C_2} & \mathbf{K}^{C_2N} \\ \mathbf{K}^{NC_1} & \mathbf{K}^{NC_2} & \mathbf{K}^{N} \end{bmatrix}, \qquad (6.24) \\
\mathbf{q}_{sys}^{ROM} &= \begin{bmatrix} \mathbf{q}^{\bar{C}} \\ \mathbf{q}^{N} \end{bmatrix} = \begin{bmatrix} \mathbf{q}^{C_1} \\ \mathbf{q}^{C_2} \\ \mathbf{q}^{N} \end{bmatrix}, \quad \mathbf{F}_{sys}^{ROM} = \begin{bmatrix} \mathbf{F}^{\bar{C}} \\ \mathbf{F}^{N} \end{bmatrix} = \begin{bmatrix} \mathbf{F}^{C_1} \\ \mathbf{F}^{C_2} \\ \mathbf{F}^{N} \end{bmatrix},
\end{aligned}
$$

where superscript $\bar{C}$ represents the constraint partition (for all components) that corresponds to the joints.

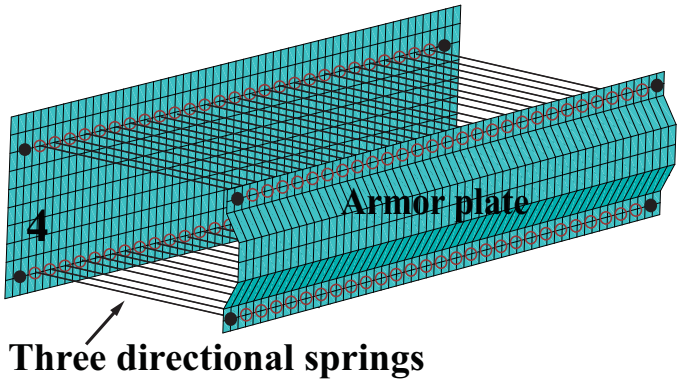

Figure 6.3: Springs modeling joints between substructure 4 and the armor plate

Next, the joints (three rectilinear springs) are applied to connect the DOFs of C_1 to those of C_2. First, the joining stiffness matrix in Eq. (6.2) and the physical coordinates of all DOFs of all joints are partitioned similar to C_1 and C_2 to obtain

$$\mathbf{K}_b = \begin{bmatrix} \mathbf{K}_b^{C_1} & \mathbf{K}_b^{C_1C_2} \\ \mathbf{K}_b^{C_2C_1} & \mathbf{K}_b^{C_2} \end{bmatrix} \text{ and } \mathbf{q}_b = \begin{bmatrix} \mathbf{q}_b^{C_1} \\ \mathbf{q}_b^{C_2} \end{bmatrix}. \tag{6.25}$$

The C_1 and C_2 partitions are the same in Eqs. (6.24) and (6.25). Thus,

$$\mathbf{q}^{C_1} = \mathbf{q}_b^{C_1} \text{ and } \mathbf{q}^{C_2} = \mathbf{q}_b^{C_2}. \tag{6.26}$$

Ultimately, Eq. (6.26) is used to obtain the final system-level equation of motion *with joints* expressed as

$$\hat{\mathbf{M}}_{sys}^{ROM}\ddot{\mathbf{q}}_{sys}^{ROM} + \hat{\mathbf{K}}_{sys}^{ROM}\mathbf{q}_{sys}^{ROM} = \hat{\mathbf{F}}_{sys}^{ROM}, \tag{6.27}$$

where

$$\begin{aligned} \hat{\mathbf{M}}_{sys} &= \mathbf{M}_{sys},\ \hat{\mathbf{K}}_{sys} = \begin{bmatrix} \mathbf{K}^{C_1} + \mathbf{K}_b^{C_1} & \mathbf{K}_b^{C_1C_2} & \mathbf{K}^{C_1N} \\ \mathbf{K}_b^{C_2C_1} & \mathbf{K}^{C_2} + \mathbf{K}_b^{C_2} & \mathbf{K}^{C_2N} \\ \mathbf{K}^{NC_1} & \mathbf{K}^{NC_2} & \mathbf{K}^{N} \end{bmatrix} \text{ and} \\ \hat{\mathbf{F}}_{sys} &= \mathbf{F}_{sys}. \end{aligned}$$

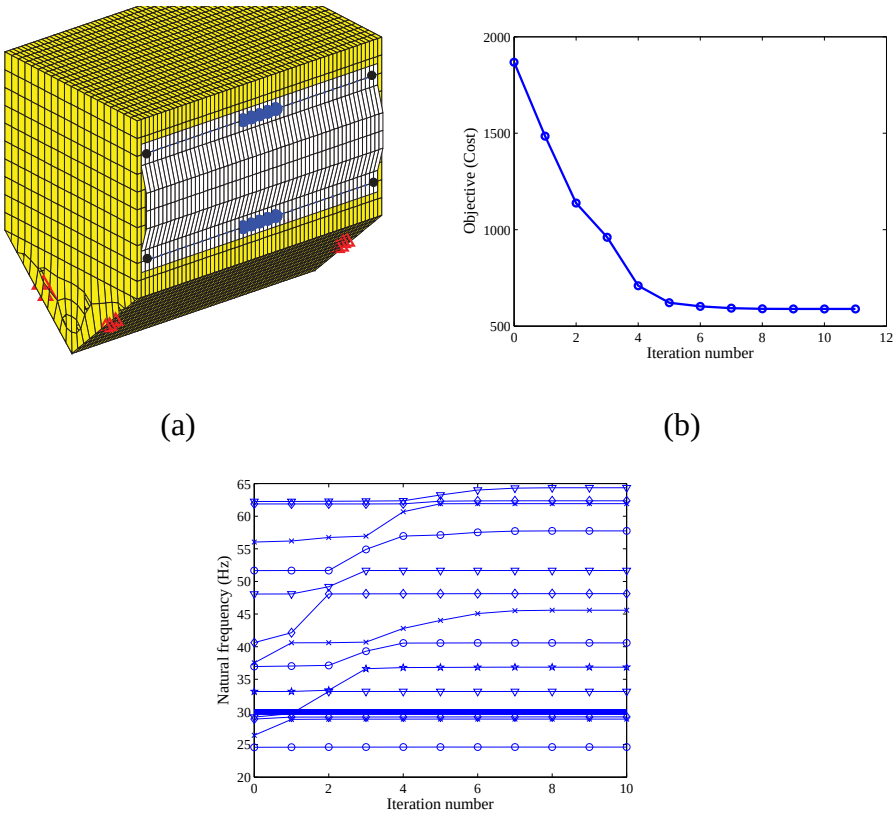

Figure 6.4: (a) 10 optimal joining locations, (b) convergence history, and (c) natural frequency variations for a 30 *Hz* excitation of the nominal structure

Note that all the design parameters are contained in the joints. Thus, the joining optimization has to reevaluate only the joints, and does not require a reevaluation of all components. Moreover, all components (except for the joints) are reduced only once, at the initial construction of NX-PROMs, before iteration. Thus, the joining design can be very efficient by using NX-PROMs with the proper matrix partitioning. By using the system matrices in Eq. (6.27) (based on NX-PROMs), the turn-around time of the iteration process is much shorter than by using FEMs. Additionally, variations in any substructure (where NX-PROM is used) can be handled efficiently in the new optimization processes.

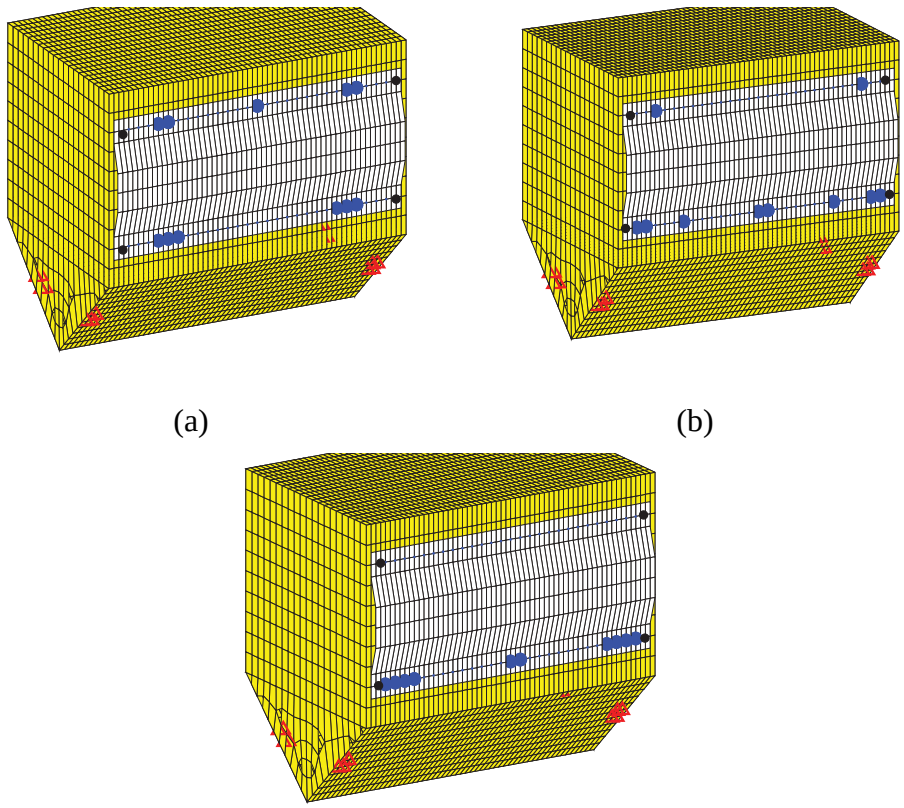

(a) (b)

(c)

Figure 6.5: Optimal joining locations for a 100 *Hz* excitation for (a) nominal structure, (b) case 1 (c) case 2 of thickness variation

6.4 Numerical Example: V-Shaped Box Structure with Thickness Variation

To demonstrate the improved/optimal joining, a structure with a V-shaped bottom is considered, as shown in Fig. 6.1. The focus of this example is to find joining locations where to attach armor to the structure. Military vehicles are typically designed to resist blasts caused by mines or improvised explosive devices and to increase survivability. For that purpose, these vehicles have a V-shaped hull under the body. Of course, any type of structure can be used to demonstrate the joining optimization. Hence, we chose to focus on finding joining locations to attach armor to military vehicles with a V-shaped hull. Fig. 6.1 shows all substructures and their number. The marked regions are candidate

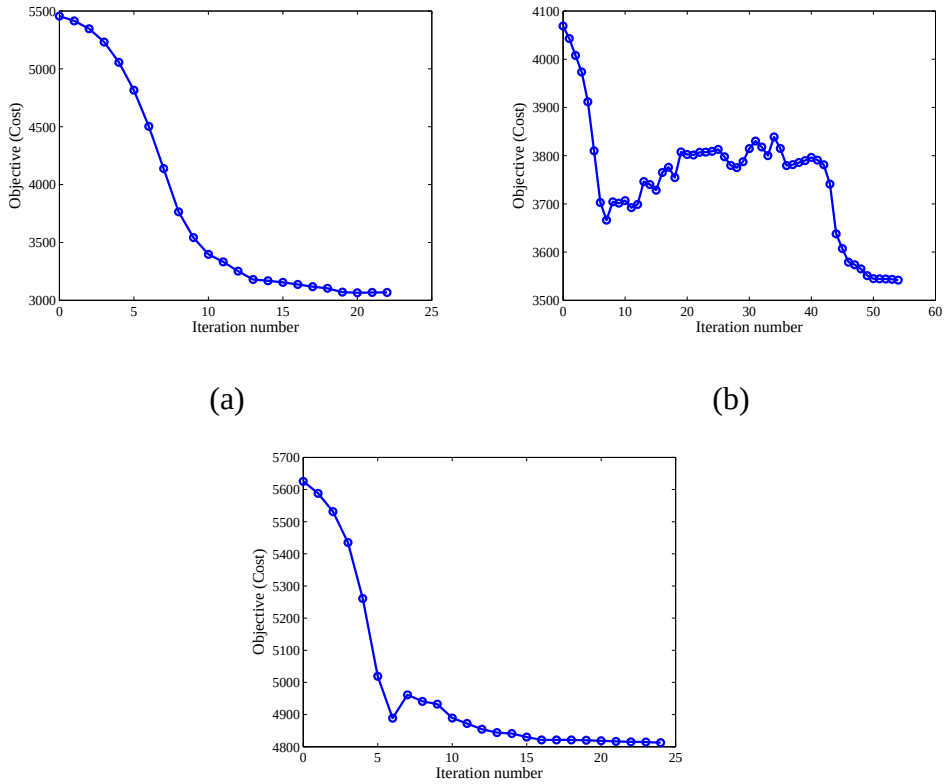

Figure 6.6: Convergence history for a 100 *Hz* excitation for (a) nominal structure, (b) case 1 (c) case 2 of thickness variation

joining locations. Harmonic loads are assumed to act on substructure 5 shown in Fig. 6.2. Substructure 6 and the armor plate have thickness variation. Tab. 6.1 shows two cases of thickness variation of each substructure. In Tab. 6.1, h_1 and h_2 indicate the parameter number. NX-PROMs are constructed by parameterizing the thickness of substructure 6 and of the armor plate. CB-CMS is applied to all remaining substructures because they do not have structural variations.

As an initial guess, all the candidate joining nodes on substructure 4 and on the armor plate are connected by three rectilinear springs as shown in Fig. 6.3. For all joints, the maximum allowable stiffness of the spring in the (main) y direction is $k_y = k_0 = 500\ \mathrm{kN/m}$, and the other directional stiffnesses are $k_x = k_z = 0.5\ k_0$. The total number of candidate

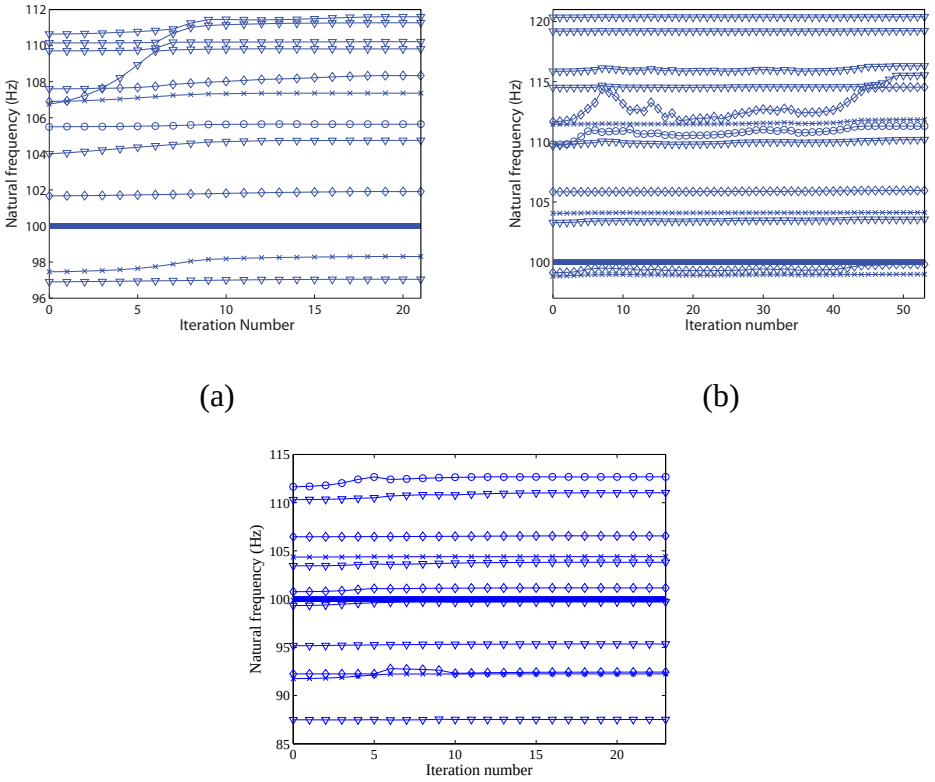

Figure 6.7: Natural frequency variation for a 100 *Hz* excitation for (a) nominal structure, (b) case 1 (c) case 2 of thickness variation

joints is 54, and the final desired number of joints N is 10 or 11. Note that the four edge nodes highlighted in Fig. 6.3 are not considered candidate joining locations. The fact that joints are present at those four locations is considered to be known.

The optimization starts with an initial guess, i.e. a given set of feasible design values ($\rho_i = 0.185$ when $N = 10$, and $\rho_i = 0.204$ when $N = 11$). The structural damping is $\gamma = 0.03$, and the weighting factors in Eq. (6.9) are $w_1 = 0.5$ and $w_2 = 0.5$. In general, the choice of weights balances the importance of vibration throughout the vehicle with the stresses in the joints. That balance is an application-dependent issue. For example, in a durability analysis, one may consider that the strain energy of the joints is more important than the total energy input into the structure. Thus, the weights can be distinct for each

application. The values of 0.5 and 0.5 were chosen arbitrarily. Note that the overall energy in the structure already includes the energy in the joints. Hence a weighting of 0.5 and 0.5 puts a little more emphasis on the joints than on the rest of the structure.

With the given initial guess, the excitation frequency was fixed at $30\ Hz$ for the nominal structure. Fig. 6.4 shows the results of the optimization for the $30\ Hz$ excitation and $N = 10$. Figures 6.5, 6.6 and 6.7 show the results of the optimization for a $100\ Hz$ excitation for the nominal structure and for cases 1 and 2 of thickness variation. For the nominal structure under the $100\ Hz$ excitation, $N = 11$. For cases 1 and 2 of thickness variation, $N = 10$.

The optimal joining locations described in Fig. 6.5 are selected differently for each case, even though the thickness variations are not very large. However, the cost function is minimized for all 3 cases, as shown in Fig. 6.6. Fig. 6.7 shows the changes in natural frequencies at each iteration. Note that the various choices made during the iterations affect significantly the dynamic response because some of the natural frequencies of the overall structure change significantly.

The optimal joint locations are significantly different for the three structures considered: the nominal structure and the two structures with thickness variation. The optimal joint locations for these three cases are quite different although the structural variations are not large. That is because the different thicknesses affect the frequencies of the structure, which in turn affect the forced response. For the nominal case at 100 Hz excitation frequency, the natural frequencies of the structure with the armor attached do not cross the value of 100 Hz at any iteration. That translates in a smaller change in the value of the cost function from iteration to iteration. That is because resonances are not close to 100 Hz at any of the iterations. For the other two cases, however, certain natural frequencies cross the excitation frequency, and resonant (or near-resonant) responses occur. Conse-

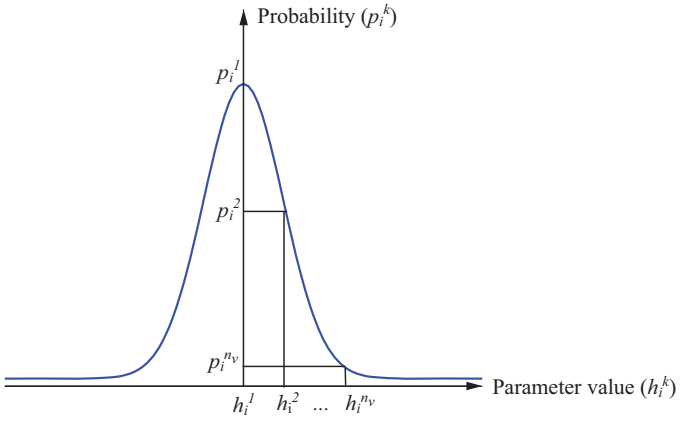

Figure 6.8: Probability distribution for the i^{th} parameter of the (nominal) vehicle in a fleet. In the numerical example, there are two such parameters (thicknesses shown in Tab. 6.1)

quently, the values of the cost function vary much more than in the nominal case. This ultimately leads to different optimal joining locations for each case. This phenomenon can prove to be a challenge when multiple structures/vehicles (nominally identical, but practically different) have to be up-armored. For that case, the proposed method provides a very good solution to the challenge of finding statistically (quasi-)optimal joint locations. To obtain such locations, one could evaluate the increase in the cost function when the joints are chose based on the nominal structure but they are applied to a structure with slightly different properties. As a first alternative, joint locations can be found by a Monte Carlo simulation (or other sample-based statistical methods). To do that, one would first use the proposed method to construct a PROM. Next, one would choose samples the parameter space (Monte-Carlo). The joint optimization can then be quickly applied using the PROM for each of the samples. After all solutions (for the joint locations) are obtained, a probability distribution can be calculated for the chosen joint locations. The joint locations with the highest probability to be chosen can then be used as candidate joint locations for

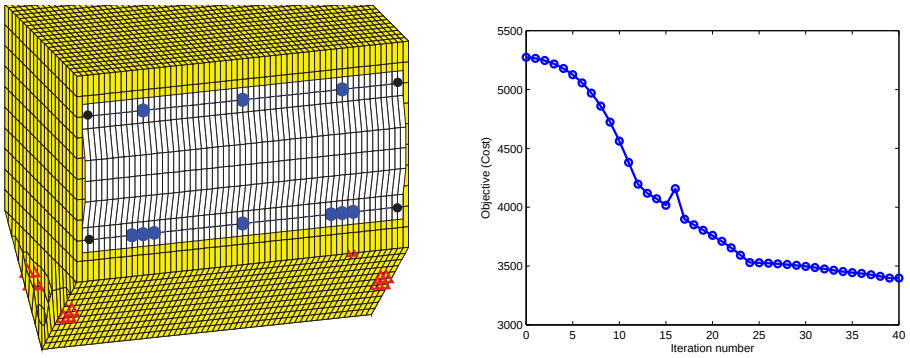

(a) (b)

Figure 6.9: (a) Optimal joining locations and (b) convergence history for 100 Hz excitation for the fleet of 3 vehicles

one final optimization which would pick the final choice of joint locations. Finally, a second (and perhaps best) alternative to find stable joint locations is to define an overall cost function specifically for series of nominally identical structures. For example, consider a case where a fleet of n_v vehicles are to be armored. They are nominally identical, but in reality they have distinct parameters (such as different material properties or thicknesses in certain components). Thus, for one set of joint locations the value of the cost function is different for each vehicle. A cost function that is a sum of the cost functions for each vehicle can easily be used in the optimization algorithm. That is because the use of the proposed PROMs allows a very fast calculation of the cost and the sensitivity at each iteration in the optimization algorithm.

Following the example of the fleet, consider that each vehicle can have variability in n_p parameters denoted by $h_1, h_2, \cdots, h_{n_p}$ (e.g., the thickness of several components). The variability in each parameter follows a given probability distribution, as schematically shown in Fig. 6.8. Denote the actual value of h_i for vehicle k as h_i^k. The two weights used in the cost function for parameter h_i for vehicle k can be chosen to be proportional to the probability p_i^k of h_i to have the value h_i^k. This probability represents the likelihood

of a vehicle in the fleet to have its parameter h_i equal to h_i^k. Hence, the weights in the definition of the overall cost function can be chosen such that

$$w_1^k = \alpha(\prod_{i=1}^{n_p} p_i^k)w_1 \quad \text{and} \quad w_2^{c_k} = \alpha(\prod_{i=1}^{n_p} p_i^k)w_2 \quad \text{for} \quad (k = 1, 2, \cdots, n_v), \tag{6.28}$$

where superscript k indicates vehicle k, and subscripts 1 and 2 indicate weights for the energy input in the structure or energy in the joints. The values w_1 and w_2 reflect the relative importance of vibration throughout the nominal vehicle and the stress in the joints of the nominal vehicle (as done for the case of a single vehicle calculations). For the sum of the weights to be one, the constant α is chosen as

$$\alpha = \frac{1}{\left[\sum_{k=1}^{n_v} (\prod_{i=1}^{n_p} p_i^k)\right](w_1 + w_2)}.$$

We implemented this calculation for the numerical example of a structure with a V-shaped bottom. The three cases that we first considered individually, we now considered as a set of nominally identical structures, $n_v = 3$. We chose the relative importance of the energy input in the structure and the energy in the joints the same way as in the individual calculations (i.e., $w_1 = 0.5$ and $w_2 = 0.5$). We chose $n_p = 2$. The two parameters h_1 and h_2 are same as the ones considered in cases 1 and 2 of parameter variation. The probabilities used had values h_1 are: $p_1^1 = 0.75$, $p_1^2 = 0.714p_1^1$, and $p_1^3 = 0.7p_1^1$. The probabilities used had values h_2 are: $p_2^1 = 0.75$, $p_2^2 = 0.2p_2^1$, and $p_2^3 = 0.5p_2^1$. All weights are obtained by using Eq. (6.28). They have different values for each vehicle. Figure 6.9 shows the results of the optimization for a 100 Hz excitation for a fleet of $n_v = 3$ vehicles (i.e., the nominal structure and the structures with case 1 and 2 of thickness variation). The overall cost function is

$$c = w_1^1 c_1^1 + w_2^1 {c_2}^1 + w_1^2 {c_1}^2 + w_2^2 {c_2}^2 + w_1^3 {c_1}^3 + w_2^3 {c_2}^3.$$

The number of desired joints N is 10. In Fig. 6.9, the minimum value of the cost function is larger than its value for the nominal case shown in Fig. 6.6 (a), but smaller than its values for two cases 1 and 2 of of thickness variation as shown in Figures 6.6 (b) and (c). That is because weights w_1^1 and w_2^1 are considerably larger than w_1^2, w_2^2, w_1^3, and w_2^3. Thus, the optimal design for the nominal structure is dominant for the entire fleet of 3 vehicles.

6.5 Conclusions

Several challenges of current methods for determining improved/optimal joining locations have been addressed. First, the mean compliance for the dynamic case with damping was derived, and the strain energy in the joints was added to the cost function. Second, a novel approach to calculate efficiently the sensitivity of the strain energy in the joints was proposed. Third, the cost function and its sensitivities were computed in the optimization process by using novel next-generation parametric reduced-order models to improve computational efficiency and to manage structural variabilities in several substructures.

The approach to select improved/optimal joining locations uses a density-based topology optimization method which employs solid isotropic material with penalization (SIMP) modeling. Based on SIMP modeling, a three rectilinear springs (with density) is used to model each joint. Also, a reliable cost function has been developed. It includes the energy input into the structure and the strain energy in all joints. By penalizing the density of the springs between 0 and 1, the cost function is minimized while satisfying a constraint which enforces an upper limit for the number of joints in the design domain. To solve this optimization problem, the modified optimality criterion method has been applied. To demonstrate the methodology, the problem of attaching armor to a structure with a V-shaped bottom has been considered. By applying the proposed methodology, improved/optimal joining locations have been selected.

The improved/optimal joining locations (obtained for each structure individually) are significantly different for the nominal structure and the two structures with thickness variation. In general, it can be challenging to find a unique set of joining locations which are good for a series of (distinct in reality, but nominally identical by design) structures. To overcome this challenge we devised an alternate approach to define overall cost function for the series of nominally identical structures. Each parameter variability occurs in the vehicles in the fleet with a given probability. Thus, the weights used in the overall cost function were chosen by taking into account these probabilities as well as the relative importance of the vibration throughout the vehicle and the stress in the joints. To demonstrate this approach, improved/optimal joining locations for a fleet of 3 vehicles have been shown.

CHAPTER VII

Conclusions

7.1 Dissertation Contributions

The main contributions of this dissertation can be summarized as follows:

- In chapter II, a multiple-component parametric reduced order models (MC-PROMs) was successfully developed. MC-PROMs enable a more direct and efficient capture of the influence of component-level design changes, damages (geometrical or structural variabilities and a crack) on the system-level structural dynamic response. The proposed MC-PROMs were developed for cases where parameter variations occur simultaneously in multiple components by developing a novel transformation matrix for model reduction. For efficient modeling of a crack, bilinear frequency approximation was employed to approximate the resonant frequency of cracked complex structures. The static mode compensation approach was adapted for use with Craig-Bampton component mode synthesis to create a novel component-level analysis.

- In chapter III, next-generation parametric reduced-order models (NX-PROMs) were developed to have enhanced numerical stability and to be used for complex structures modeled with brick-type finite elements. NX-PROMs have three main advancements compared to MC-PROMs: (1) a new parameterization technique for-

mulated to capture the element-level nonlinearity due to volume variations of finite elements of brick or other types, (2) a new transformation matrix developed using a novel interpolation of static constraint modes, (3) a local-interface reduction (LIR) technique proposed for further enhancing the computational efficiency

- In chapter IV, robust signal processing techniques were proposed for structural health monitoring. The techniques were used to capture the mode shapes of a cracked structure with structural variability by selecting the optimal sensor locations. The bilinear mode approximation (BMA) was developed in the PROMs domain to approximate mode shapes of cracked structures to be used in novel sensor placement techniques. The modal assurance criterion (MAC) was generalized to select sensitive modes of cracked structures by using the bilinear mode shapes of the healthy structure and structures with different crack lengths. Sensor placement technique based on effective independence distribution vector was employed and enhanced to select optimal sensor locations. An over-sampled algorithm was developed to be used in conjunction with enhanced sensor placement technique to reduce the effects of measurement noise. A Monte-Carlo technique was implemented to select statistically optimal and robust sensor locations to capture the mode shapes of a cracked complex structure with structural variabilities.

- In chapter V, the robust signal processing techniques were applied and modified to identify the size of a crack in a complex structure. PROM-based robust signal processing techniques were extended and used in a new crack detection algorithm. The resonant shapes were shown to vary nonlinearly with the crack length. To capture the nonlinear variations, a crack length identification algorithm was developed, and the new sensor placement techniques were employed to capture these variations.

Then, the signals obtained from the selected minimal/optimal sensors were used to identify the size of a crack. A Monte-Carlo technique was also employed to select statistically optimal sensor locations to identify the size of a crack.

- In chapter VI, structural optimization techniques were developed for joining of components of complex structures for improved dynamic response. The mean compliance for the dynamic case with damping was derived, and the strain energy in the joints was added to the cost function. A novel approach to calculate efficiently the sensitivity of the strain energy in the joints was proposed. The cost function and its sensitivities were computed in the optimization process by using NX-PROMs to improve computational efficiency and to manage structural variabilities in several substructures.

7.2 Future Research

Next, based on the work reported in this dissertation, some suggestions for future research are proposed. The novel reduced-order modeling technique and the sensor placement algorithms used to identify damage, as well as the structural optimization techniques have been developed and validated computationally. However, these techniques have not been validated experimentally. Thus, experimental efforts should be concentrated on enhancing and experimentally testing the modeling, damage detection, and signal processing methodologies developed in this research.

The key experimental validations to be performed can be summarized as follows:

- Validate the MC-PROMs and NX-PROMs themselves.

- Validate the signal processing methodology used for damage detection as well as the algorithms used for detection. Specifically, the validation should focus on

(a) the PROM-based approach for selecting sensors for damage detection,

(b) the algorithms and technology for damage detection in structures with variability.

- Validate the nonlinear techniques and codes used to predict the nonlinear response of cracked structures. Specifically, the validation should focus on

  (a) the bi-linear frequency approximation,

  (b) the novel bi-linear modal approximation.

- Validate the structural optimization methodology.

BIBLIOGRAPHY

BIBLIOGRAPHY

[1] H. B. Yun and S. Masri. Stochastic change detection in uncertain nonlinear systems using reduced-order models: System identification. *Smart Materials and Structures*, 17:015040–1–015040–13, 2008.

[2] H. B. Yun and S. Masri. Stochastic change detection in uncertain nonlinear systems using reduced-order models: Classification. *Smart Materials and Structures*, 18:015004–1–015004–12, 2009.

[3] S. Chung and E. Fung. A nonlinear finite element model of a piezoelectric tube actuator with hysteresis and creep. *Smart Materials and Structures*, 19:045025–1–045028–19, 2010.

[4] U. Ashwin, S. Raja, and D. Dwarakanathan. A finite element based substructuring procedure for design analysis of large smart structural systems. *Smart Meterials and Structures*, 18:045006–1–045006–11, 2009.

[5] D. J. Hartl, D. C. Lagoudas, and F. T. Calkins. Advanced methods for the analysis, design, and optimization of sma-based aerostructures. *Smart Materials and Structures*, 20:094006–1–094006–20, 2011.

[6] W. C. Hurty. Dynamic analysis of structural systems using component modes. *AIAA Journal*, 3(4):678–685, 1965.

[7] R. R. Craig, Jr. and M. C. C. Bampton. Coupling of substructures for dynamic analyses. *AIAA Journal*, 6(7):1313–1319, 1968.

[8] S. Rubin. Improved component-mode representation for structural dynamic analysis. *AIAA Journal*, 13(8):995–1006, 1975.

[9] R. M. Hintz. Analytical methods in component mode synthesis. *AIAA Journal*, 13(8):1007–1016, 1975.

[10] R. R. Craig, Jr. and C.-J. Chang. Free-interface methods of substructure coupling for dynamic analysis. *AIAA Journal*, 14(11):1633–1635, 1976.

[11] M. P. Castanier, Y.-C. Tan, and C. Pierre. Characteristic constraint modes for component mode synthesis. *AIAA Journal*, 39(6):1182–1187, 2001.

[12] Wen-Hwa Shyu, Jianmin Gu, Gregory M. Hulbert, and Zheng-Dong Ma. On the use of multiple quasi-static mode compensation sets for component mode synthesis of complex structures. *Finite Elements in Analysis and Design*, 35(2):119–140, 2000.

[13] W. Wang and J. Kirkhope. Complex component mode synthesis for multi-shaft rotors with flexible inter-shaft bearings. *Journal of Sound and Vibration*, 173(4):537–555, 1994.

[14] W. Wang and J. Kirkhope. Complex component mode synthesis for damped systems. *Journal of Sound and Vibration*, 181(5):781–800, 1995.

[15] M. H. Liu and G. T. Zheng. Improved component-mode synthesis for nonclassically damped systems. *AIAA Journal*, 46(5):1160–1168, 2008.

[16] I. Takewaki. Inverse component-mode synthesis method for redesign of large structural systems. *Computer Methods in Appiled Mechanics and Engineering*, 166:201–209, 1998.

[17] F. Matichard and L. Gaudiller. Hybrid modal nodal method for multibody smart structure model reduction: Application to modal feedback control. *Smart Materials and Structures*, 15:1887–1898, 2006.

[18] D. Kim, M. Lee, and J. Jan. Substructure synthesis method for a nonlinear structure with a sliding mode condition. *Journal of Sound and Vibration*, 321:704–720, 2009.

[19] D. Tran. Component mode synthesis methods using partial interface modes: Application to tuned and mistuned structures with cyclic symmetry. *Computers and Structures*, 87:1141–1153, 2009.

[20] I. Takewaki and K. Uetani. Inverse component-mode synthesis method for damped large structural systems. *Computers and Structures*, 78:415–423, 2000.

[21] A. Elhami, G. Lallement, P. Minotti, and S. Cogan. Methods that combine finite group theory with component mode synthesis in the analysis of repetitive structures. *Computers and Structures*, 48(6):975–982, 1993.

[22] C. Farhat and M. Geradin. On a component mode synthesis method and its application to incompatible substructures. *Computers and Structures*, 51(5):459–473, 1994.

[23] L. Jezequel and S. T. Tchere. A procedure for improving component-mode representation in structural dynamic analysis. *Journal of Sound and Vibration*, 144(3):409–419, 1991.

[24] J. Moon and D. Cho. A component mode synthesis applied to mechanisms for an investigation of vibration. *Journal of Sound and Vibration*, 157(1):67–79, 1992.

[25] G. Masson, B.A. Brik, S. Cogan, and N. Bouhaddi. Component mode synthesis (CMS) based on an enriched ritz approach for efficient structural optimization. *Journal of Sound and Vibration*, 296:845–860, 2006.

[26] A. Shanmugam and C. Padmanabhan. A fixed-free interface component mode synthesis method for rotordynamic analysis. *Journal of Sound and Vibration*, 297:664–679, 2006.

[27] L. Hinke, F. Dohnal, B. R. Mace, T. P. Waters, and N.S. Ferguson. Component mode synthesis as a frame work for uncertainty analysis. *Journal of Sound and Vibration*, 324:161–178, 2009.

[28] E. Balmès. Parametric families of reduced finite element modes: Theory and application. *Mechanical Systems and Signal Processing*, 10(4):381–394, 1996.

[29] D. Langlais E. Balmès, F. Ravary. Uncertainty propagation in modal analysis. In *Proceedings of IMAC-XXII: A Conference and Exposition on Structural Dynamics*, pages IMAC–XXII–57., Dearborn, MI, 2004.

[30] G. Zhang, M. P. Castanier, and C. Pierre. Integration of component-based and parametric reduced-order modeling methods for probabilistic vibration analysis and design. In *Proceedings of the Sixth European Conference on Structural Dynamics, Paris, France,*, pages 993–998, Paris, France, 2005.

[31] K. Park, G. Zhang, M. P. Castanier, and C. Pierre. A component-based parametric reduced-order modeling technique and its application to probabilistic. In *Proceedings of ASME International Mechanical Engineering Congress and Exposition*, pages IMECE2006–15069, Chicago, IL, USA, 2006.

[32] K. Park. *Component-Based Vibration Modeling Methods for Fast Reanalyses and Design of Complex Structures*. PhD thesis, University of Michigan, 2008.

[33] S. Lim, R. Bladh, M. P. Castanier, and C. Pierre. Compact, generalized component mode mistuning representation for modeling bladed disk vibration. *AIAA Journal*, 45(9):2285–2298, 2007.

[34] S.-H. Lim, M. P. Castanier, and C. Pierre. Vibration modeling of bladed disks subject to geometric mistuning and design changes. In *Proceedings of the 45th AIAA/ASME/ASCE/AHS/ASC Structures, Structural Dynamics and Material Conference, Palm Springs, CA, 2004, AIAA 2004-1686.*, 2003.

[35] S. K. Hong, B. I Epureanu, M. P. Castanier, and D. J. Gorsich. Parametric reduced-order models for predicting the vibration response of complex structures with component damage and uncertainties. *Journal of Sound and Vibration*, 330:1091–1110, 2011.

[36] O. Poudou and C. Pierre. Hybrid frequency-time domain methods for the analysis of complex structural systems with dry friction damping. In *Proceedings of the 44th AIAA/ASME/ASCE/AHS/ASC Structures, Structural Dynamics and Materials Conference, Norfolk, Virginia, 2003, AIAA 2003-1411.*, volume 1, pages 111–124, Reston, VA, 2003. AIAA.

[37] O. Poudou and C. Pierre. A new hybrid frequency-time domain method for the forced vibration of elastic structures with friction and intermittent contact. In *Proceedings of the 10th International Symposium on Transport Phenomena and Dynamics of Rotating Machinery, Honolulu, Hawaii, 2004, paper ISROMAC10-2004-068*, Honolulu, Hawaii, March 2004.

[38] S. W. Shaw and P. J. Holmes. A periodically forced piecewise linear oscillator. *Journal of Sound and Vibration*, 90(1):129–155, 1983.

[39] M. Chati, R. Rand, and S. Mukherjee. Modal analysis of a cracked beam. *Journal of Sound and Vibration*, 207(2):249–270, 1997.

[40] A. Saito, M. P. Castanier, and C. Pierre. Estimation and veering analysis of nonlinear resonant frequencies of cracked plates. *Journal of Sound and Vibration*, 326:725–739, 2009.

[41] F Ansari. Practical implementation of optical fiber sensors in civil structural health monitoring. *Journal of Intelligent Material Systems and Structures*, 18:879–889, 2007.

[42] E. B. Flynn and M. D. Todd. Optimal placement of piezoelectric actuators and sensors for detecting damage in plate structures. *Journal of Intelligent Material Systems and Structures*, 21:265–274, 2009.

[43] M. Krommer, M. Zellhofer, and K. H. Heilbrunner. Strain-type sensor networks for structural monitoring of beam-type structures. *Journal of Intelligent Material Systems and Structures*, 20:1875–1888, 2009.

[44] D. C. Kammer. Sensor placement for on-orbit modal identification and correlation of large space structures. *Journal of Guidance*, 14(2):251–259, 1991.

[45] J. E. T. Penny, M. I. Friswell, and S. D. Garvey. Automatic choice of measurement locations for dynamic testing. *AIAA Journal*, 32(2):407–414, 1994.

[46] M. P. Bendsøe and N. Kikuchi. Generating optimal topologies in structural design using a homogenization method. *Computer Methods in Applied Mechanics and Engineering*, 71:197–224, 1988.

[47] M. P. Bendsøe. Optimal shape design as a material distribution problem. *Structural Optimization*, 1:193–202, 1989.

[48] M. Zhou and G. I. N. Rozvany. The COC algorithm, part II: Topological, geometrical and generalized shape optimization. *Computer Methods in Applied Mechanics and Engineering*, 89:309–336, 1991.

[49] R. J. Yang and A. I. Chahande. Automotive applications of topology optimization. *Structural Optimization*, 9:246–249, 1995.

[50] M. P. Bendsøe and O. Sigmund. *Topology Optimization: Theory, Methods and Applications*. Springer, 2002.

[51] M. Chirehdast and T. Jiang. Optimal design of spot-weld and adhesive bond patterns. In *International Congress and Exposition 1996, SAE, Paper No. 960812*, 1996.

[52] T. Jiang and M. Chirehdast. A system approach to structural topology optimization: Designing optimal connections. *ASME Transations: Journal of Mechanical Design*, 119:40–47, 1997.

[53] H. Chickermane and H. C. Gea. Design of multi-component structural systems for optimal layout topology and joint locations. *Engineering with Computers*, 13:235–243, 1997.

[54] J. H. Zhu and W. H. Zhang. Maximization of structural natural frequency with optimal support layout. *Structural and Multidisciplinary Optimization*, 31(6):462–469, 2006.

[55] Q. Li, G. P. Steven, and Y.M. Xie. Evolutionary structural optimization for connection topology design of multi-component systems. *Engineering Computations*, 18(3-4):460–479, 2001.

[56] Y. M. Xie and G. P. Steven. A simple evolutionary procedure for structural optimization. *Computer and Structures*, 49:885–896, 1993.

[57] Y. M. Xie and G. P. Steven. Optimal design of multiple load case structures using an evolutionary procedure. *Engineering Computations*, 11:295–302, 1994.

[58] Y. M. Xie and G. P. Steven. *Evolutionary Structural Optimization*. Springer-Verlag, 1997.

[59] E. Hinton and J. Sienz. Fully stressed topological design of structure using an evolutionary procedure. *Engineering Computations*, 12:229–244, 1995.

[60] E. Hinton, J. Sienz, S. Bulman, and S. J. Lee. Fully integrated design optimization of engineering structures using adaptive finite element models. In *Proceedings of the First Australasian Conference no Structural Optimization, Keynote paper*, pages 73–78, 2011.

[61] P. Roski. Three-dimensional topology design of structures using crystal models. *Computer and Structures*, 55:1077–1083, 1995.

[62] O. C. Zienkiewicz and R. L. Taylor. *The Finite Element Method*. Butterworth Heinemann, 1967.

[63] Thomas J. R. Hughes. *The Finite Element Method Linear Static and Dynamic Finite Element Analysis*. Dover, 2000.

[64] S. K. Hong, B. I Epureanu, and M. P. Castanier. Novel sensor placement for damage identification in a cracked complex structure with structural variability. *Journal of Intelligent Material Systems and Structures*, 22:1189–1202, 2011.

[65] A. Saito, M. P. Castanier, C. Pierre, and O. Poudou. Efficient nonlinear vibration analysis of the forced response of rotating cracked blades. *Journal of Computational and Nonlinear Dynamics*, 4:011005–1–011005–10, 2009.

[66] A. Saito and B. I. Epureanu. Bilinear modal representations for reduced-order modeling of localized piecewise-linear oscillators. *Journal of Sound and Vibration*, 330:3442–3457, 2011.

[67] R. J. Allemang and D. L. Brown. A correlation coefficient for modal vector analysis. In *Proceedings of the International Modal Analysis Conference*, pages 110–116, 1982.

[68] R. J. Allemang. The modal assurance criterion - twenty years of use and abuse. *Sound and Vibration*, 37(8):14–23, 2010.

[69] R. Johanson, P. Papalambros, and N. Kikuchi. Topology optimization of multibody structural systems. *Manufacturing Science and Engineering*, 68(2):505–509, 1994.

[70] Z. D. Ma, N. Kikuchi, C. Pierre, and B Raju. Multi-domain topology optimization for vehicle substructure design. In *2002 ASME IMECE Proceedings*, pages IMECE 2002–32908, 2002.

[71] G. I. N. Rozvany, M. Zhou, and T. Birker. Generalized shape optimization without homogenization. *Structural Optimization*, 4:250–252, 1992.

[72] D. Heiserer, M. Chargin, and J. Sielaff. High performance, process oriented, weld spot approach. In *MSC Wouldwide Automotive*, 1999.

[73] J. Fang, C. Hoff, B. Holman, F. Mueller, and D. Wallerstein. Welding modeling in MSC NASTRAN. In *Second MSC Worldwide*, 2000.

[74] Y. Zhang and D. Taylor. Optimization of spot-welded structures. *Finite Elements in Analysis and Design*, 37(9):1013–1022, 2001.

[75] M. Palmonella, M. I. Friswell, J. E. Mottershead, and Lees. A. W. Guidelines for the implementation of the CWELD and ACM2 spot weld models in structural dynamics. *Finite elements in Analysis and Design*, 41:193–210, 2004.

[76] S. Donders and M. Brughmans. The effect of spot weld failure on dynamic vehicle performance. *Sound and Vibration*, 39(4):16–25, 2005.

[77] S. W. Chae, K. Y. Kwon, and Lee. T. S. An optimal design system for spot welding locations. *Finite Elements in Analysis and Design*, 38:276–294, 2002.

[78] M. P. Bendsøe and O. Sigmund. Material interpolation schemes in topology optimization. *Archive of Applied Mechanics*, 69:635–654, 1999.

[79] O. Sigmund. A 99 line topology optimization code written in matlab. *Structural dna Multidisciplinary Optimization*, 21(2):120–127, 2001.

[80] K. Svanberg. The method of moving asymptotes - a new method for structural optimization. *International Journal for Numerical Methods in Engineering*, 24:359–373, 1987.

[81] K. Svanberg. A class of globally convergent optimization methods based on conservative convec separable approximations. *SIAM Journal on Optimization*, 12(2):555–573, 2002.

[82] Z. D. Ma, N. Kikuchi, and I. Hagiwara. Structural topology and shape optimization for a frequency response problem. *Computational Mechanics*, 13:157–174, 1993.

[83] K. K. Choi and N. H. Kim. *Structural Sensitivity Analysis and Optimization I: Linear Systems*. Springer, 2005.